Advanced material platforms for holographic applications of photonic metasurfaces

Mohammad Biabanifard Hossein Abadi

A thesis submitted for the degree of PhD
at the
University of St Andrews

2024

DOI: https://doi.org/10.17630/sta/826

Abstract

Metasurface holographic applications such as imaging, sensing, data encryption and biophotonics are promising for more advanced photonic devices. However, most prevailing material platforms are constrained to rigid substrates with transparency windows at $\lambda > 500$ nm, where absorption losses become significant at shorter wavelengths. This thesis demonstrates rigid and flexible material platforms to realise holographic metasurfaces functioning at shorter wavelengths across the visible spectrum. In particular, it presents zirconium dioxide metasurfaces as a novel material platform, all-polymeric metasurfaces, and incoherent light metasurfaces. Pillar with top and air-hole meta-atoms configurations, operating in transmission across the visible spectrum, are introduced.

Zirconium dioxide metasurfaces, characterised by a high refractive index, hardness, and biocompatibility, are systematically designed, fabricated, and experimentally measured. These metasurfaces are utilised for holographic image projection and lab-on-chip optical trapping, employing a retrieval algorithm for hologram design. The integration of these lab-on-chip devices has the potential to replace conventional bulky objective lenses, thereby advancing optics integration.

All-polymeric holographic metasurfaces are designed, fabricated, and experimentally characterised using a novel single-material meta-atom design adaptable to various materials. Specifically implemented with SU-8, these metasurfaces are applied to achieve conformable holographic image projection. Their potential for mass-scale production is highlighted by the low fabrication cost and design simplicity, exploiting nanolithography methods.

Metasurfaces designed to operate with incoherent light sources are developed, fabricated, and partially characterised. The design methodology is described. The initial experimental results are rewarding, but further investigations are required to enhance their performance. These findings are promising to extend the applicability of these incoherent metasurfaces for out-of-lab applications.

The advancement of holographic devices, including their materials, operational wavelengths, and excitation methods, will pave the way for advances in the field.

Candidate’s declaration

I, Mohammad Biabanifard Hossein Abadi, do hereby certify that this thesis, submitted for the degree of PhD, which is approximately 38,000 words in length, has been written by me, and that it is the record of work carried out by me, or principally by myself in collaboration with others as acknowledged, and that it has not been submitted in any previous application for any degree. I confirm that any appendices included in my thesis contain only material permitted by the 'Assessment of Postgraduate Research Students' policy.

I was admitted as a research student at the University of St Andrews in February 2020.

I received funding from an organisation or institution and have acknowledged the funder(s) in the full text of my thesis.

Date Signature of candidate

9/03/2024

Supervisor's declaration

I hereby certify that the candidate has fulfilled the conditions of the Resolution and Regulations appropriate for the degree of PhD in the University of St Andrews and that the candidate is qualified to submit this thesis in application for that degree. I confirm that any appendices included in the thesis contain only material permitted by the 'Assessment of Postgraduate Research Students' policy.

Date Signature of supervisor

9/03/2024

Permission for publication

In submitting this thesis to the University of St Andrews we understand that we are giving permission for it to be made available for use in accordance with the regulations of the University Library for the time being in force, subject to any copyright vested in the work not being affected thereby. We also understand, unless exempt by an award of an embargo as requested below, that the title and the abstract will be published, and that a copy of the work may be made and supplied to any bona fide library or research worker, that this thesis will be electronically accessible for personal or research use and that the library has the right to migrate this thesis into new electronic forms as required to ensure continued access to the thesis.

I, Mohammad Biabanifard Hossein Abadi, confirm that my thesis does not contain any third-party material that requires copyright clearance.

The following is an agreed request by candidate and supervisor regarding the publication of this thesis:

Printed copy

No embargo on print copy.

Electronic copy

No embargo on electronic copy.

Date Signature of candidate

9/03/2024

Date Signature of supervisor

9/03/2024

Underpinning Research Data or Digital Outputs

Candidate's declaration

I, Mohammad Biabanifard Hossein Abadi, hereby certify that no requirements to deposit original research data or digital outputs apply to this thesis and that, where appropriate, secondary data used have been referenced in the full text of my thesis.

Date Signature of candidate

9/03/2024

Acknowledgements

General acknowledgements

First of all, this journey would not have been possible without the insightful and prudent guide and influence of my supervisor, Prof. Andrea Di Falco, who honed my skills with his expertise which have been invaluable in shaping the direction and success of this research.

Secondly, I would like to express my deepest gratitude to Dr Sebastian Schulz who supported me through this journey. I cannot forget the unreserved help of Dr Jonathon Harwell who helped me at the start of my journey through this PhD.

My thanks also go to the past and present members of the Synthetic Optics group, in particular, to Saydulla Persheyev, Meisam Askari, Jianling Xiao, Tomasz Plaskocinski, who created an active and fruitful team working environment. Next, my thanks go to the clean room technicians.

Finally, I would like to thank my beloved parents and brothers, who have always supported me in my life.

Thank you all for being part of this intellectual and personal milestone.

Funding

This work was supported by the European Research Council (ERC) under the European Union Horizon 2020 Research and Innovation Program (Grant Agreement No. 819346).

Research Data/Digital Outputs access statement

Research data underpinning this thesis are available at:

[To be added]

Science is the only way forward.

Publications

Publications Resulting from this Work

- **Mohammad Biabanifard**, Tomasz Plaskocinski, Jianling Xiao, and Andrea Di Falco. "ZrO_2 holographic metasurfaces for efficient optical trapping in the visible range." *Advanced Optical Materials* (2024): 2400248.
- **Mohammad Biabanifard**, Jianling Xiao, and Andrea Di Falco. "Thin-film polymeric metasurfaces for visible wavelengths." *Applied Physics Letters* 123, no. 23 (2023).
- Xiao, Jianling, Tomasz Plaskocinski, **Mohammad Biabanifard**, Saydulla Persheyev, and Andrea Di Falco. "On-Chip Optical Trapping with High NA Metasurfaces." *ACS photonics* 10, no. 5 (2023): 1341-1348.
- Xiao, Jianling, Tomasz Plaskocinski, **Mohammad Biabanifard**, and Andrea Di Falco. "Self-Calibrated Flexible Holographic Curvature Sensor." *Advanced Materials Technologies* (2024): 2301851.
- Yan, Libin, Jianling Xiao, Tomasz Plaskocinski, **Mohammad Biabanifard**, Saydulla Persheyev, Meisam Askari, and Andrea Di Falco. "Two-tier manipulation of holographic information." *Optics Express* 30, no. 11 (2022): 19145-19151.

Conferences

- **Mohammad Biabanifard**, Tomasz Plaskocinski, Jianling Xiao, and Andrea Di Falco. "High Numerical Aperture ZrO_2 Holographic Metasurfaces for Biophotonics Applications." Photonic technology for biomedical applications, CLEO Europe 2023, Munich, Germany. Presentation, Contribution: presented by **Mohammad Biabanifard**.
- **Mohammad Biabanifard**, Tomasz Plaskocinski, Jianling Xiao, Andrea Di Falco 'ZrO_2 Holographic Metasurfaces for Biophotonics Applications' Metasurfaces and their Applications, META 2023, Paris, France. Presentation, Contribution: presented by **Mohammad Biabanifard**.
- Jianling Xiao, Libin Yan, Tomasz Plaskocinski, **Mohammad Biabanifard**, Saydulla Persheyev, Meisam Askari, and Andrea Di Falco 'Environment-Dependent Holographic Metasurfaces In The Visible Range' Tunable and holographic metasurfaces, CLEO Europe 2023, Munich, Germany, Presentation.
- Tomasz Plaskocinski, Jianling Xiao, **Mohammad Biabanifard**, Saydulla Persheyev, Andrea Di Falco 'Holographic Optical Metasurfaces with High Trap Stiffness' Poster session, CLEO Europe 2023, Munich, Germany, presentation.
- Tomasz Plaskocinski, Jianling Xiao, **Mohammad Biabanifard**, Saydulla Persheyev, Andrea Di Falco 'Photonic metasurfaces for biophotonics' Optical Trapping and Optical Micromanipulation XX, 2023, San Diego, California, United States, presentation.

Contents

6 Holographic metasurfaces for imaging and optical trapping applications in the visible range 112

Chapter 1

Introduction

This chapter introduces the main topics of this thesis and its context. It discusses the physics behind the four main types of metasurfaces and categorises them by their constituent material. Finally, the chapter gives a brief overview of the applications of metasurfaces.

1.1 Introduction to metasurfaces

Metamaterials are well-known three-dimensional (3D) structures in the photonics community. They are artificial materials that may be engineered to have properties that cannot be found in natural materials. Interestingly, they gain their properties from their structure rather than their composition. These artificially man-made 3D structures are also known as Meta-films [1-2]. The prefix Meta indicates that its characteristics are beyond normal structures, which can be found in nature. The reason behind these names is that the thickness of these devices compared to their area is negligible.

Metasurfaces (MSs) are two-dimensional versions of metamaterials. Hence, they take up much less space in the third dimension. Subsequently, and compared to metamaterials, MSs represent the possibility of easier fabrication with a less challenging scheme. These structures have sub-wavelength features that can manipulate the complex wavefront of light waves. For instance, MSs bring us complete control of the wavefront in terms of amplitude, phase, polarisation, and the direction of propagation [3-4].

It is essential to emphasise that these types of control over the complex wavefront of light waves are usually achieved by using bulky optics that take a considerable amount of volume; thus, integrating these bulky optics is an obstacle. However, introducing MSs with small thin areas that can replicate these controls over the complex wavefront with improved properties over the scattered light facilitates the manipulation of light waves and holds promise for their integration into numerous applications.

Moreover, MSs leverage their electromagnetic scattering characteristics to not only facilitate the precise manipulation of phase, amplitude, and polarisation of incident light at subwavelength scales but also to effectively suppress the undesirable effects associated with high-order diffraction [4-6].

Consequently, MSs have facilitated the manipulation of optical properties capabilities that pose challenges to conventional optics. A noteworthy aspect that has garnered significant interest among researchers is the compatibility of these two-dimensional structures with contemporary semiconductor technology [7]. Furthermore, they can be fabricated using techniques such as photolithography and nanoimprinting [8].

Here, I illustrate the phase discretisation concept using an example. Fig. 1.1(a) depicts a simple refractive lens focusing light on its focal length. Figure 1.1(b) depicts the division of the lens into 2π optical phase segmentations, signifying that these segmented portions have no impact on the lens's performance.

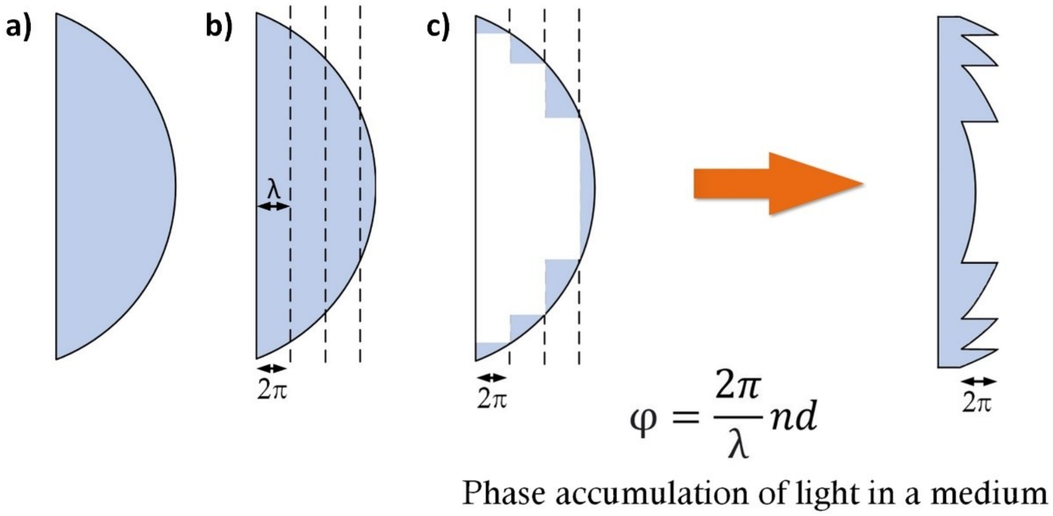

Fig. 1.1. (a) A simple refractive lens, (b-c) idea of Fresnel lens.

This becomes evident when comparing it to Fig. 1.1(c), where the segments mentioned above are removed, leaving only the representation of the underlying concept akin to that of a Fresnel lens. The principal challenge associated with lenses of this nature lies in the intricacy of their fabrication, demanding a precise manufacturing process.

The discretisation of phase at various discrete levels allows for the creation of diffractive lenses. As an illustration, Fig. 1.2 demonstrates a two-level phase discretisation scheme, namely 0 and π. While the fabrication of such lenses is relatively straightforward, their efficiency is poor and suffers from substantial phase information losses. Increasing the number of phase discretisation levels is imperative to enhance efficiency. However, achieving this poses a formidable challenge due to the demanding fabrication process involved.

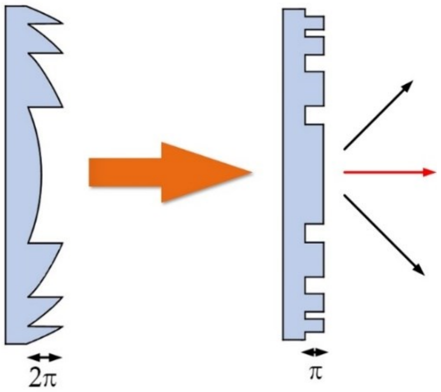

Fig. 1.2. Schematically showing the transformation of the complex cross-sectional profile of a Fresnel lens to a binary phase mask, representing 0 or π optical phase shift. The black and red arrows schematically illustrate the change in the direction of light propagation.

Discussing the characteristics of light when it encounters an obstacle in its path is interesting. This matter can be considered from two points of view: (i) ray optics, where the object dimensions are much larger than the light wavelength, and (ii) wave optics, where the object dimensions are comparable to the light wavelength. The light behaviour is understandable through Snell's law of refraction when it impinges homogeneous large interfaces like water or glass. However, a more complex situation should be considered when light impinges inhomogeneous small interfaces when the light wavelength is comparable to the interface's feature sizes.

1.1.1 Generalised Snell's law

The determination of the positions of objects submerged in water has historically captivated human thought as it diverged from external observations. This phenomenon is depicted in Fig. 1.3, highlighting the distinction between the actual location of a fish and its apparent position as perceived by a fisherman. In earlier times, the underlying cause of this disparity remained elusive; today, we attribute it to 'refraction', a phenomenon arising from changing the direction of light as it traverses through two substances with different densities.

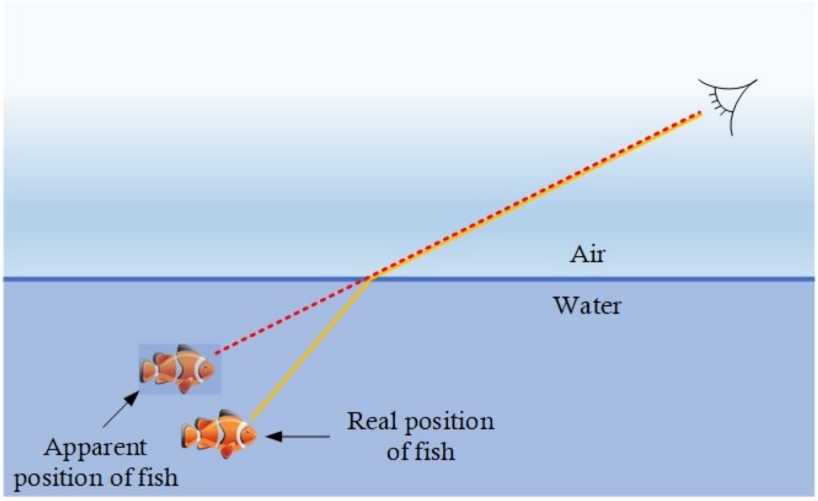

Fig. 1.3. Refraction phenomenon in the water.

Refraction occurs when the velocity of light changes while transitioning between different media. This alteration in light velocity arises due to density variations in different media. This velocity change during light propagation results in a change in the direction of propagation. Exploiting ray optics, Snell's law of refraction elucidates the relationship between the refractive index (n) of a medium and the angle of refraction, given by $n_i\,sin(\theta_i) = n_r\,sin(\theta_r)$, where n_i and n_r are the refractive indices of the incident and refraction media, θ_i and θ_r represent the angles of incidence and refraction, respectively [9]. Although Snell's law is a valuable tool for isotropic and planar interfaces, it does not provide an accurate response for anisotropic and complex non-planar interfaces with different materials and geometries. However, wave optics provide more accurate results in this situation. In 1962, it was demonstrated that Snell's law must have a more general form in a nonlinear medium [10]. More recently, since 2008 and 2011, with the advent of two-dimensional artificial structures, MSs, it has been shown that the direction of refraction and reflection can be carefully engineered [11-13]. The point is that Snell's law works very well for homogeneous media. To analyse a medium that is inhomogeneous and usually consists of different materials/media, wave optics rather than ray optics can give a better understanding by exploiting generalised laws of reflection and refraction [13]. The continuity of the electromagnetic fields' factors at the boundary between two different media supports Fresnel [14] and Snell's law equations. Therefore, conventional optical components are designed based on this continuity. However, with the progress in the field of nanotechnology, allowing the making of engineered inhomogeneous interfaces with different materials, another approach was introduced to control light behaviour in such interfaces. Structured interfaces containing different materials with different refractive indices can create the required optical response in terms of phase and amplitude modulation. This extraordinary response comes from the reflection and refraction laws introduced by generalised Snell's law.

MSs introduce an abrupt phase shift when light traverses through a thin engineered interface between two media. Snell's law was generalised by Federico Capasso and his team in 2012 when they explored the properties of thin MSs [13]. Introducing phase discontinuity brings new degrees of freedom and great flexibility in designing devices for countless applications [15-16]. The choice of unit cells for MSs is wide, including electromagnetic cavities [17-18], nanoparticle clusters [19-20], and plasmonic antennas [21-22], which offer broad tailorable optical features [23-27] and are relatively easy to fabricate.

Starting with Fermat's principle [28], the path taken by a ray between two given points is the path that can be traversed in the least time, considering a plane wave is illuminated from medium one toward medium two with the angle of θ_i. Looking at Fig. 1.4, assume that the two depicted paths are infinitesimally close to the actual light path. To this end, the phase difference between them must be zero, resulting in the following equation [13]:

$$[k_0 n_i \sin(\theta_i)dx + (\Phi + d\Phi)] - [k_0 n_t \sin(\theta_t)dx + (\Phi)] = 0, \qquad (1.1)$$

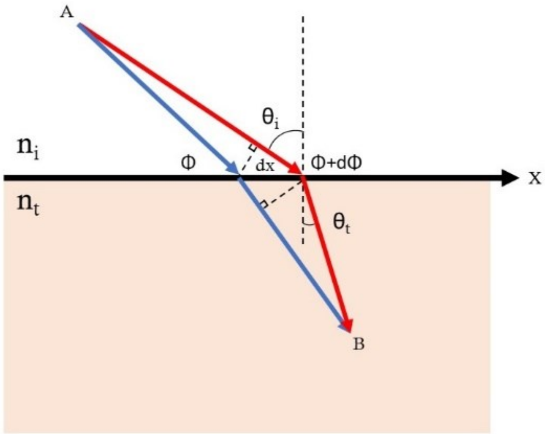

Fig. 1.4. Using the concept of Fermat's principle to derive the general law of reflection and refraction.

where $k_0 = 2\pi/\lambda_0$ and λ_0 is the vacuum wavelength, n_i and n_t are respectively, the refractive indices of the first and second media, θ_t is the angle of refraction, dx is the distance between two crossing points, Φ and Φ+dΦ are the local phase discontinuities at the interface crossings. By designing the phase gradient along the interface to be constant, relation (1) would be [13]:

$$\sin(\theta_t)n_t - \sin(\theta_i)n_i = \frac{\lambda_0}{2\pi}\frac{d\Phi}{dx} \tag{1.2}$$

This equation indicates that the refracted light could have an arbitrary direction. The direction is related to introducing a constant gradient of phase discontinuity, $d\Phi/dx$, along with the interface [13]. This means the angle of transmitted and reflected light depends also on the local phase gradient created by the meta-atoms. Hence, Snell's law is a specific situation of this equation where the phase gradient is constant.

In addition, it is worth pointing out that (i) the separation between resonators controls the amount of extraordinary reflection and refraction, and (ii) it is assumed that the amplitude of scattered waves by each unit-cell is the same, so the refracted and reflected beams are plane wave [13].

Figure 1.5 shows the potential of MSs in creating a desirable wavefront. The phase shift between the incident and emitted radiation of an optical resonator gradually changes across a resonance. The phase discontinuity along the interface can be engineered by designing the meta-atoms with appropriate spatial separation in an array [13]. The meta-atoms must cover the whole 0-2π range for complete wavefront control.

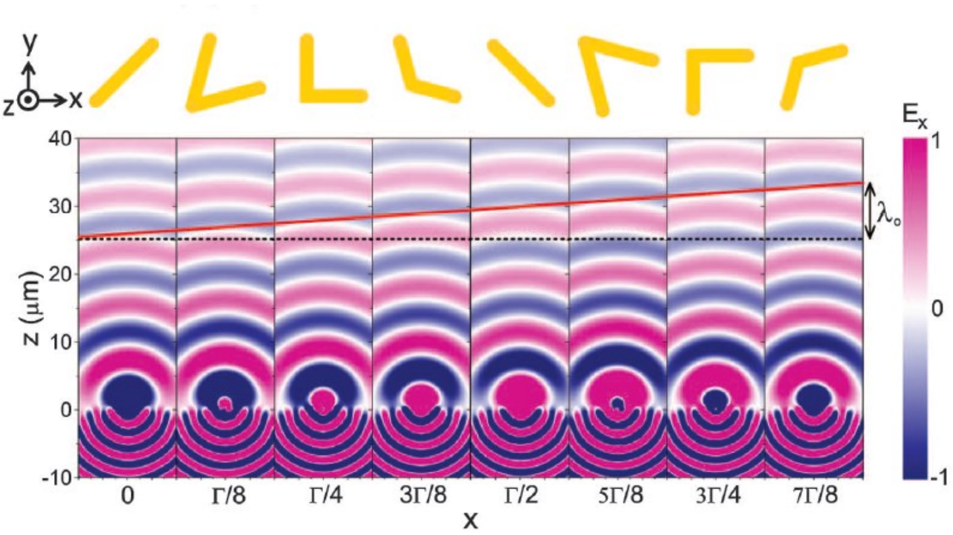

Fig. 1.5. FDTD simulation of meta-atoms consisting of an array of metallic resonators (Γ is the unit cell array lengths), each segmented part illustrates the electric field scattering of the meta-atoms shown [13].

In the first demonstration of phase discontinuity, as illustrated in Fig. 1.5, eight elements of the metallic antenna are used to cover the 0-2π range. Each of them shifts the phase with the amount of π/4 with respect to that of the incident wave. The array of antennas is in the x-y plane, while Fig. 1.5 shows the electric Field in the x-z plane. Γ is the period of the unit cell, the meta-atoms are located in air at z>0, and the space z≤0 is a silicon substrate. The scattered electric field is x-polarized, while the excitation is a y-polarized plane wave at normal incidence with respect to the silicon substrate. The drawn red line is the envelope of the projections of the spherical waves scattered by the antennas onto the x-z plane. Considering Huygens's principle, the anomalously refracted beam is made of the superposition of these spherical waves with the phase gradient along with the interface [13]. This indicates the direction of the scattered waves can be further controlled. The control over the wavefront plus the direction of the propagation opens up an enormous opportunity for lots of applications, through which the metalens can be mentioned as a prominent example.

1.2 Types of metasurfaces

The materials used in the structure of the MSs determine some of their main properties, including their working spectrum. Metal-based MSs are relatively easy to make, but they absorb light in the visible range. However, dielectric materials hold promise for designing MSs operating in the visible light spectrum. This section presents different techniques for designing MSs with regard to their constituent material (metallic or dielectric). Following this, the physics underlying different MSs is explained through examples.

1.2.1 Resonant metallic metasurfaces

According to Huygens' principle, the wavefront can be manipulated by controlling the phase and amplitude of the individual point sources that constitute the wavefront. In resonant metallic MSs, each meta-atom, as the basic building block of the MS, works as a spherical point source. Consequently, complete control over the wavefront is achieved by manipulating the phase and amplitude of these fundamental building blocks. The key point in the working principle of these structures is surface plasmon polaritons (SPPs). SPPs are electromagnetic excitations at the interface between a metal and a dielectric material [29]. Generally, resonant metallic or plasmonic MSs are made of metal nanoparticles over a substrate. In these structures, free electrons are excited on the surface and oscillate collectively when the incident light impinges the metal. The collective oscillations of free electrons with the frequency of the incident electromagnetic wave introduce a resonance. These resonances are forcefully dependent on the natural frequency of their vibration, geometrical shape, size, and the dielectric surrounding the metals [30-31]. SPPs are surface waves propagating along the metal-dielectric interface and strongly become evanescent in the direction perpendicular to the interface. Fig. 1.6 intuitively depicts how the SPPs are generated.

A long and highlighted list of proposed structures could excite SPPs in different spectra of EM waves from microwave to visible range, among which nanorod antennas as popular practical structures can be mentioned [4, 13, 32-36].

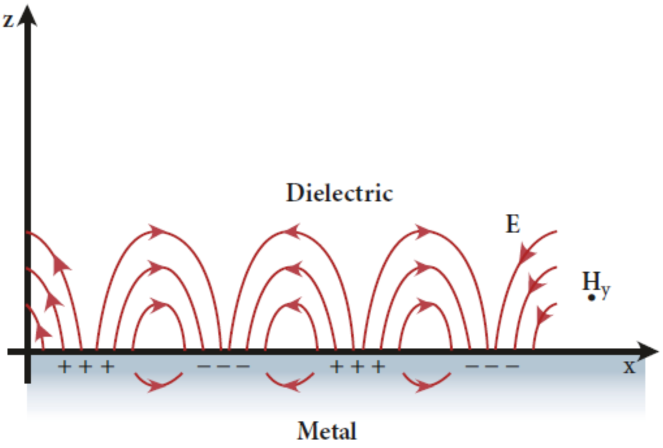

Fig. 1.6. Distribution of charges in the presence of an electric field when SPPs are propagating on the metal-dielectric interface [37].

Here, to explain the concept, I used the nanorod antenna structure. Consider an incident light with the wavelength λ, the resonance approximately occurs at $L_{res} = \lambda/2,$ where λ is the surface plasmon wavelength, which is related to the dispersion in the metal. In this situation, the exciting antenna current is in phase with the incident light. If the antenna length is smaller than L_{res}, the excited antenna current phase leads compared to that of the incident. Similarly, if the antenna length is larger than L_{res} the current phase lags. The coverage of the phase is between 0-π by involving a single antenna resonance, but some techniques are demonstrated for covering the whole 0-2π range, which is vital for controlling the wavefront. Among these, multiple independent and coupled antenna resonances can be listed [38].

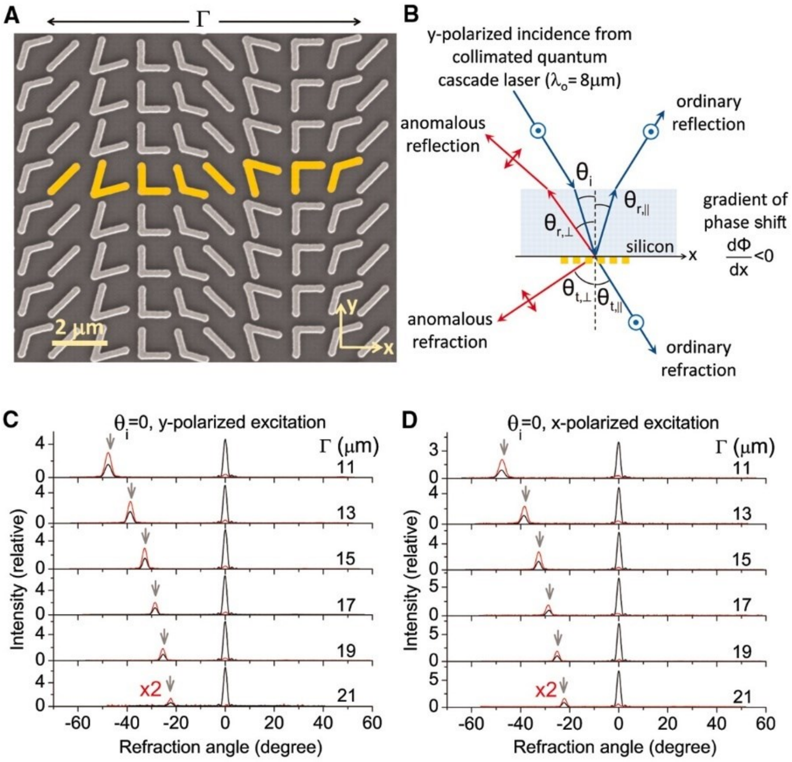

Fig. 1.7. (A) Scanning electron microscope (SEM) image of an antenna array fabricated on a silicon substrate. The unit cell of the plasmonic interface highlighted in yellow colour consists of eight gold V-antennas of width ~220 nm and thickness ~50 nm. It repeats with a periodicity of Γ = 11 μm in the x direction and 1.5 μm in the y direction. (B) Schematic show the experimental setup for y-polarised excitation (electric field normal to the plane of incidence). (C, D) Measured far-field intensity profiles of the refracted beams for y- and x-polarised excitations, respectively. The refraction angle is considered from the normal to the surface. The red and black curves represent the measured values with and without a polariser, for six samples with different periodicity, respectively. The polariser is used to select the anomalously refracted beams that are cross-polarised with respect to the excitation. It should be noted that the amplitude of the red curves is magnified by a factor of two for clarity [13].

For instance, Fig. 1.7 shows an array of resonant metallic MS unit cells made of eight elements. The unit cell is a V-shaped nanorod with two arms having different angles. Each element applies an additional phase shift of π/4 to the incident wave compared to its left sub-unit-cell starting from 0 to 7π/4 [13]. Fig. 1.8 shows this MS. Panel (a) shows the applied phase shift in different areas of the MS imposed by the meta-atoms. Panel (b) intuitively illustrates how the meta-atoms are placed to satisfy the required phase profile to create the vortex beam as a complex control of the beam profile. To explain how the amplitude and polarisation can be controlled, I would like to explain the physics behind them through an example. Back in the proposed structure with a phase coverage of 0-2π, the structure consists of V-shaped resonant metallic antennas that support two symmetric and asymmetric modes [13].

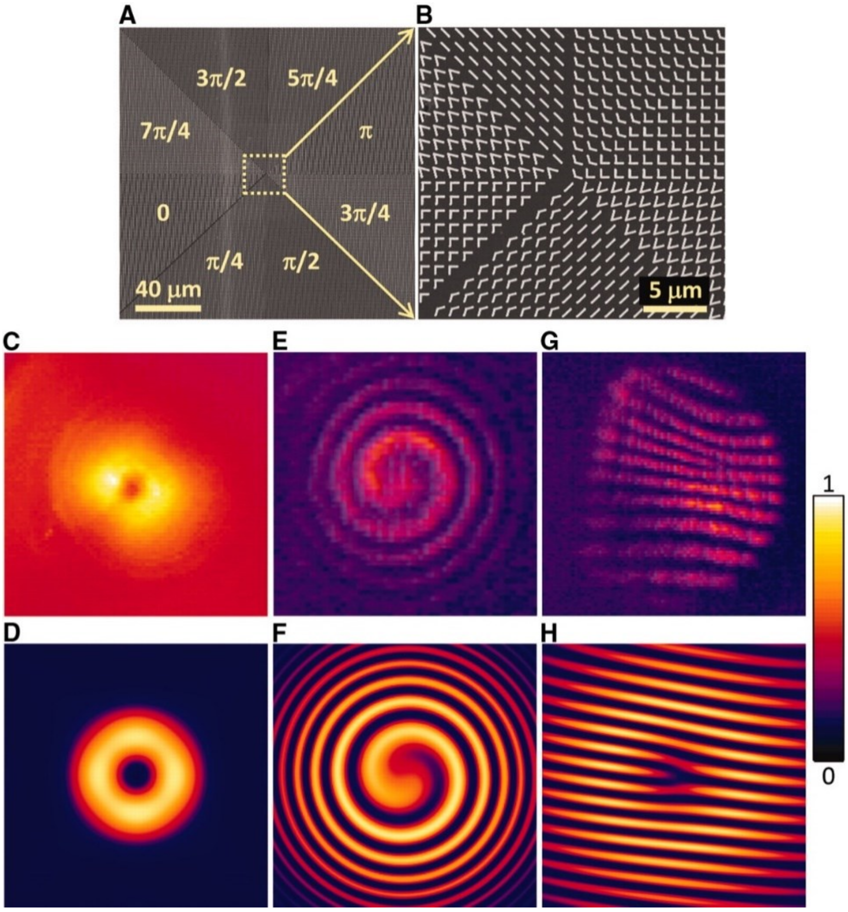

Fig. 1.8. SEM image of a plasmonic interface (Au nanorods on silicon substarte) that generates an optical vortex. The plasmonic pattern consists of eight regions, as shown in the figure, and each region is occupied by one constituent antenna of the eight-element. The antennas are arranged to create a phase shift that varies azimuthally from 0 to 2π, thus generating a helicoidal scattered wavefront. (B) SEM image of the centre area specified with a square in (A). (C, D) Respectively, measured and calculated far-field intensity distributions of an optical vortex with topological charge one. The constant background in (C) is because of the thermal radiation. (E, F) Respectively, measured and calculated spiral patterns generated by the interference of the vortex beam and a co-propagating Gaussian beam. (G, H) Respectively, measured and calculated interference patterns with a dislocated fringe generated by the interference of the vortex beam and a Gaussian beam when the two are tilted with respect to each other. The circular border of the interference pattern in (G) arises from the finite aperture of the beam splitter used to combine the vortex and the Gaussian beams. The size of (C) and (D) is 60 × 60 mm^2 , and that of (E) to (H) is 30 × 30 mm^2 [13].

The antennas are made of two identical arms with a length of h and an angle Δ between the two arms [13]. For simplicity in description, two unit vectors are defined: $\hat{s}$ along the symmetry axis of the V-shaped antenna and $\widehat{a}$ perpendicular to $\hat{s}$ as shown in Fig. 1.9. The current distribution in each arm of the symmetric mode is approximately the same in that we have only one straight antenna with a length of h. So, the first-order antenna resonance happens at $h \approx \lambda_{eff} / 2$ where λ_{eff} is the effective wavelength [22, 39].

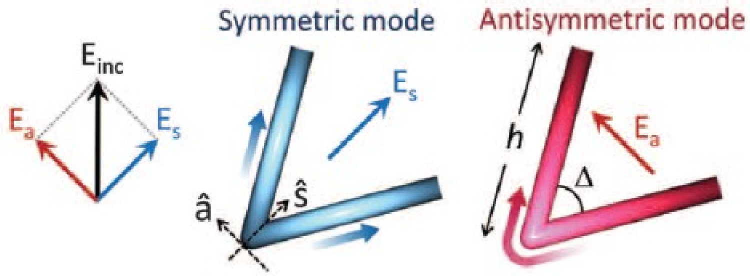

Fig. 1.9. Schematic showing V-antenna supporting two symmetric and asymmetric modes excited by components of the incident field along $\hat{s}$ and $\hat{a}$ respectively. The V-shaped antenna is illuminated by an incident light polarised 45° respect to $\hat{s}$. Current distribution is plotted while brighter colour indicates larger currents. Also, the direction of current flow is illustrated by arrows with colour gradient [13].

The asymmetric current distribution in each arm is like a half current distribution of a straight antenna with a length of $2h$. Similarly, the first-order antenna resonance in this mode occurs at $2h \approx \lambda_{eff}/2$.

The polarisation state of the scattered field is the same as the incident when the incident wave is polarised along $\hat{s}$ and $\hat{a}$. In the case of arbitrary incident polarisation, both the symmetric and antisymmetric modes will be exited but with completely different amplitude and phase due to the distinguished resonance conditions [13]. This means that the polarisation of the scattered light could be different from the incident light. This means by using the modal properties of these modes, one can control the scattered wave's phase, amplitude, and polarisation.

As another example, the amplitude and phase control of the SPPs exploiting an MS is proposed in [4]. Figure 1.10 illustrates how the meta-atoms orientation is different when applying the required phase shift. The authors introduced a novel approach for independent control of the phase and amplitude using an array of subwavelength dipole gold Nanoantennas. The proposed array is in close proximity to a gold surface that enables light to be coupled efficiently to SPPs [4].

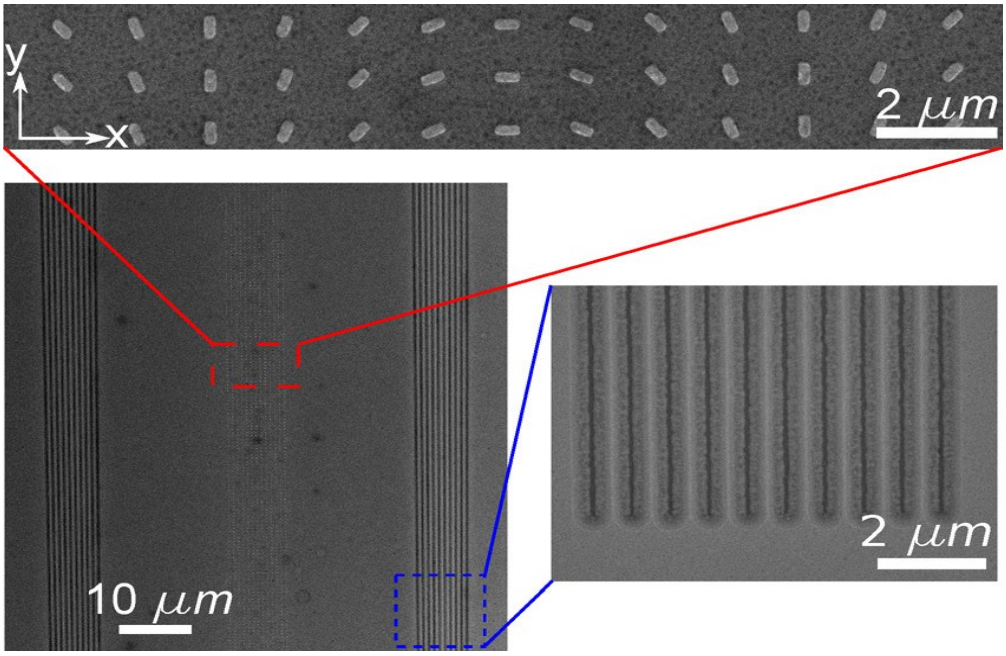

Fig. 1.10. SEM images of the sample with the gold nanoantenna array and the etched gratings on both sides. The image at the top shows a magnified view of three complete rows of the nanoantennas. The image to the right shows parts of the right gratings, which couple the SPP to the far field [4].

1.2.2 Pancharatnam-Berry metasurfaces

Pancharatnam-Berry technique is a popular and practical technique that can be used to design both metallic and dielectric MSs [40-45]. This technique uses local resonators, usually plasmonic structures interacting with circularly polarised light, and a 2π phase shift is achievable through the change of the resonator's geometrical orientation. Hence, this method uses meta-atoms with the same geometry to obtain complete control over the phase [46]. Figure 1.11 shows one of the most practical realisations of this approach using nanorod meta-atoms. To explain this method, assume that a normal incident light illuminates an anisotropic nanostructure in which the incident light's polarisation state is along the nanostructure's two-principle axis. Also, t_o and t_e represent the complex transmission coefficients.

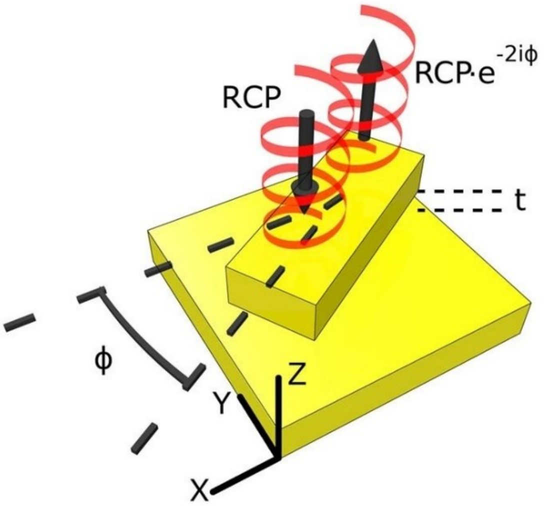

Fig. 1.11. Perspective of the nanorod unit cell structure with incident right-hand circularly polarised light. The spacing between the nanorod and backplane is denoted as *t*. The angle *ϕ* belongs to the XY plane and is defined between the long axis of the nanorod and the X axis [47].

Rotating this nanostructure by the amount of θ from the x-axis, as depicted in Fig. 1.12, results in a change in the transmission coefficients. This can be mathematically derived using the operation of Jones matrix [48-49]:

$$\begin{aligned}\hat{t}(\theta) &= R(-\theta)\begin{pmatrix} t_o & 0 \\ 0 & t_e \end{pmatrix}R(\theta) \\ &= \begin{bmatrix} \cos\theta & -\sin\theta \\ \sin\theta & \cos\theta \end{bmatrix}\begin{bmatrix} t_o & 0 \\ 0 & t_e \end{bmatrix}\begin{bmatrix} \cos\theta & \sin\theta \\ -\sin\theta & \cos\theta \end{bmatrix}. \\ &= \begin{bmatrix} t_o\cos^2\theta + t_e\sin^2\theta & (t_o - t_e)\cos\theta\sin\theta \\ (t_o - t_e)\cos\theta\sin\theta & t_o\sin^2\theta + t_e\cos^2\theta \end{bmatrix}\end{aligned} \tag{1.3}$$

In the above calculations, R(θ) is the rotation matrix. By assuming that the incident light is circularly polarised (CP), the transmitted electric field of the light for the left-handed CP or right-handed CP can be achieved by equation (1.3). As known, each CP can be considered as two linearly polarised waves: $\hat{e}_{L/R} = (\hat{e}_x \pm i\hat{e}_y)/\sqrt{2}$, so it can be derived as [51-52]:

$$E^t_{L/R} = \hat{t}(\theta).\hat{e}_{L/R} = \frac{t_o + t_e}{2}\hat{e}_{L/R} + \frac{t_o - t_e}{2}e^{\pm i2\theta}\hat{e}_{L/R}\,. \tag{1.4}$$

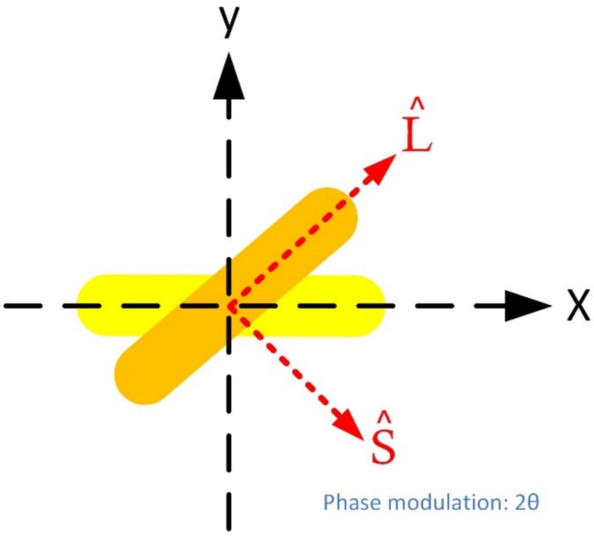

Fig. 1.12. Schematically showing the Pancharatnam-Berry-phase metasurfaces exploiting nanorods as unit cells of the metasurface and that the phase response is only related to the angle of nanorod with respect to the x-axis (θ) [50].

From equation (1.4), one can see that the first term represents CP scattered light. At the same time, its helicity is identical to that of the incident wave, and the second term has the opposite helicity while carrying an additional Pancharatnam-Berry phase (±i2θ). As a result, the phase shift of 0-2π can be achieved for opposite-handed CP by rotating the nanoresonator from 0 to π [41].

Metallic MSs are appropriate for numerous applications and are still among the best platforms to work in reflection [38, 53-55]. However, they are suffering from increasing dissipative losses in optical frequencies, which is the main focus of the spectrum in this thesis. There are plenty of undesirable loss channels during the phase-modulation process, among which diffraction, ordinary refraction/reflection, and polarisation conversion losses can be listed. Although using reflective type MSs, there are reported works with efficiency of more than 80% in microwave and optical frequencies [40, 56], they cannot efficiently perform in transmission and visible range, particularly the shorter wavelengths.

In many applications and this thesis, MSs working in transmission mode are required. To this end, researchers paved the way and found metallic MSs counterparts using dielectric materials that do not inherit the loss of metals.

1.2.3 Huygens metasurfaces

To overcome the limitation of metallic MSs, all-dielectric MSs are introduced. Their ability to interact with light in optical frequencies, especially at the visible range, is one of the most significant reasons that dielectric MSs have drawn the attention of numerous researchers during recent years [57-58].

In general, Huygens' MSs consist of a thin layer of electric and magnetic dipoles that are orthogonal to each other, creating an array of Huygens' sources [59-63]. Huygens' principle states that the complex wavefront of an EM wave can be constructed from spherical source points [64]. This becomes interesting when the EM wave faces a small slit, where the wavelength is comparable to the size of the slit.

Maxwell's equations state that electric and magnetic fields induce each other. Thus, in Huygens' MSs, the idea is to use the superposition of electric dipole (ED) and magnetic dipole (MD) resonances to achieve 2π phase coverage. To satisfy this term, each meta-atom, which can be considered as a Mie resonance, can achieve an approximate π phase shift. Thus, the 2π phase shift is achievable when ED and MD resonances of the same order overlap. Therefore, designing a structure that satisfies the overlapping of ED and MD resonances is the key to the design. Usually, Huygens' MSs, owing to their working principle, are subwavelength thick [65].

Following the physics underlying Huygens MSs, the Helmholtz equation can be separated for spherical or cylindrical dielectric particles, and it is in excellent agreement with Mie scattering theory [66]. Hence, the calculation of Mie theory is enormously appreciated and is a powerful tool for dielectric nanoparticles. Besides, by extending the solution to the spherical vector wave function, the radiation and internal field of spherical shapes are calculated [37]. Usually, the experimental data and the analytical calculations for the radiation field are compared to extract each mode's contribution. Also, the analytical expressions for the internal field correspond to the distribution of the field inside the medium, and it discloses the physical mechanism of transmission or reflection for the MS [37].

It has been proved that high-refractive-index nanoparticles/nanodisks can generate electric and magnetic responses with considerable strength in approximately the same spectra. For instance, this feature is the key requirement to achieve optimal transmission efficiency for Huygens' MSs [59-63, 67]. The inherent losses at the visible spectrum for metallic MSs result in poor efficiency. In contrast, dielectric MSs take advantage of low loss and can couple the incident light, producing circular current displacement and, consequently, having a strong magnetic dipole resonance, as depicted in Fig. 1.13 [68-72].

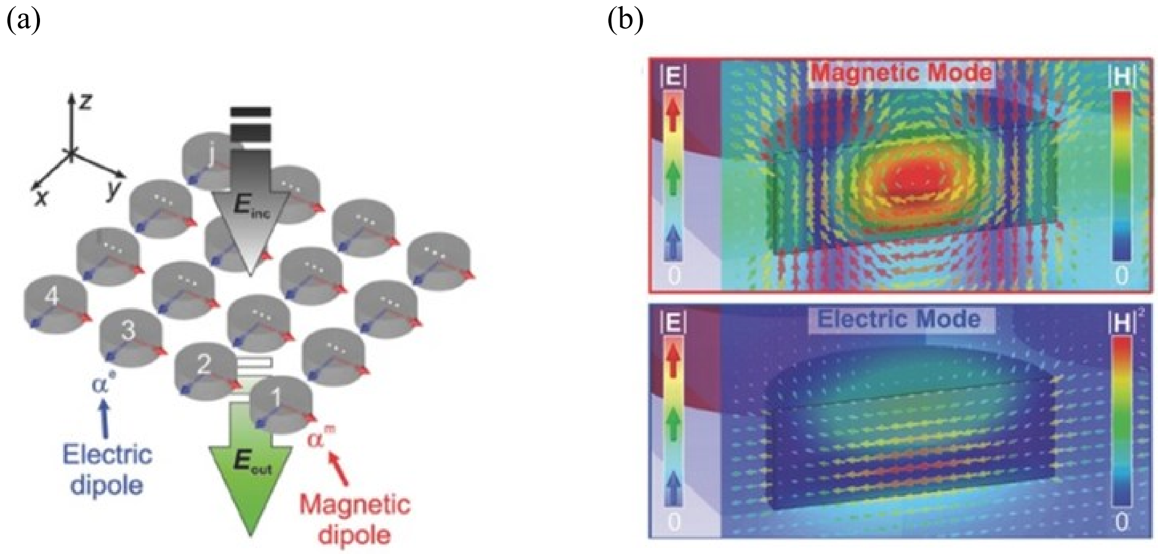

Fig. 1.13. a) Schematic of dielectric Huygens' MS using arrays of nanodisks represented as electric and magnetic dipoles with polarisabilities α^e and α^m under x-polarised illumination. b) the dominant Electric (coloured arrows) and magnetic (plain colour) field distributions for the magnetic (top) and electric (bottom) modes of periodic Si nanodisks [3, 68].

Besides, in aspherical geometries, the magnetic dipole modes occur [37]. As an instance, the electric and magnetic dipole resonances for a single-layer cylindrical silicon resonator on a silicon-insulating substrate are shown in Fig. 1.14(a).

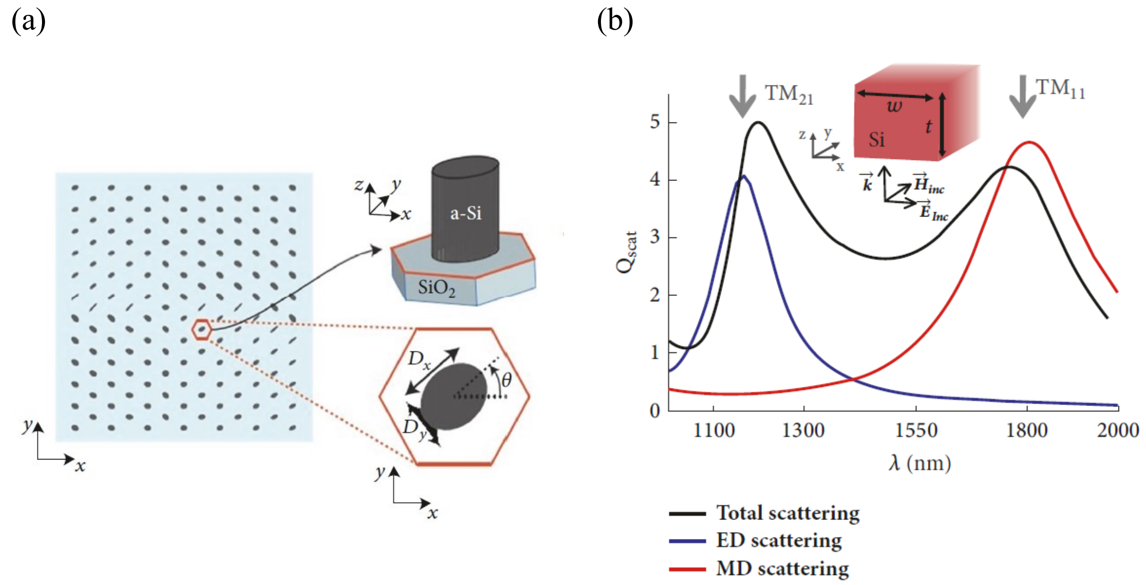

Fig. 1.14. (a) The metasurface consists of an elliptic amorphous silicon column with the same height, different diameters (D_x and D_y), and different azimuthal angles (θ). The columns are located in the centre of the hexagonal unit cell. (b) Rectangular dielectric nanoparticles also exhibit electromagnetic field polarisability. The figure shows the dominant ED and MD [37, 65, 73].

Also, for rectangular resonators, the variation of the size provides easy tuning over the resonant wavelength, which is depicted in Fig. 1.14(b) [73]. Thus, Huygens' MSs can be realised by carefully managing these ED and MD resonances.

1.2.4 High-contrast metasurfaces

These types of MSs can be realised using dielectrics with high refractive index and offer transmission phase MSs, which can be considered as truncated waveguides [74-76]. In contrast with Huygens MSs, where the meta-atoms support two resonant modes, one with a strong electric dipole and another with a strong magnetic dipole, the meta-atoms in high-contrast MSs contain diploe, quadrupole and higher electric and magnetic multipoles [75].

Owing to the truncation on both ends, they support multiple low-quality Fabry-Perot resonances, where the light bounces back and forth between the two ends of the meta-atom [75]. The constructive interference of these resonances contributes to the high transmission. Meta-atoms with high refractive index materials induce a dephasing dependent on their geometry [75-81]. In the most popular form, the meta-atom unit cell consists of a high-refractive index material on a low-refractive index substrate [75-82]. As a result, the illuminated light strongly interacts with the higher refractive index material and excites different modes. These excitations provide the required optical amplitude and phase response, which depends on the geometry of the meta-atom.

Figure 1.15 depicts the excitation of eight dominant modes inside a meta-atom to show their contribution to transmission. This meta-atom consists of a high refractive index material (amorphous silicon) embedded inside a low refractive index material (Polydimethylsiloxane (PDMS)). Fig. 1.15(d) shows the superposition effect of these eight dominant modes that create a strong transmission through the meta-atom.

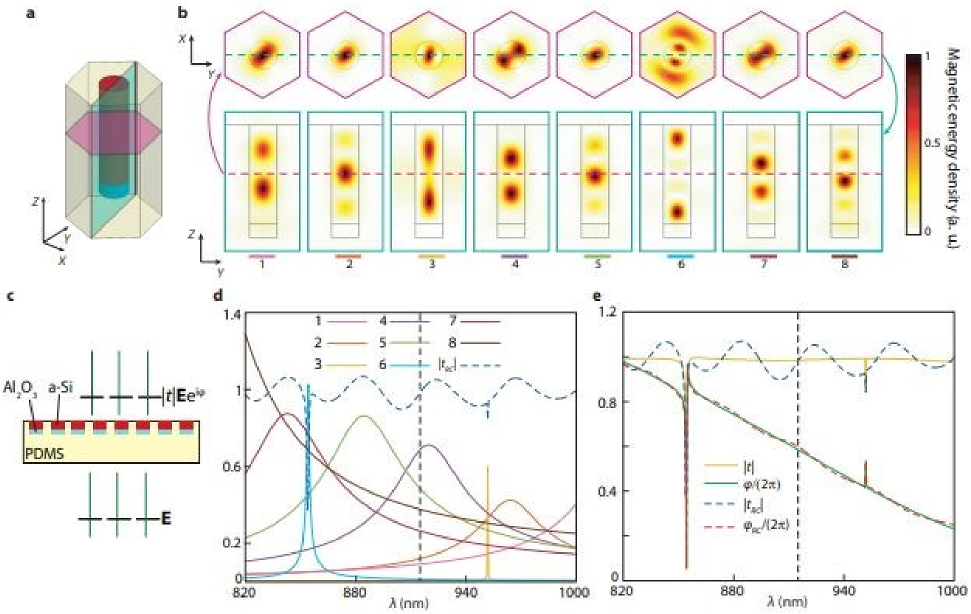

Fig. 1.15. Highlighting the contribution of different resonant modes of the nano-posts to transmission. (a) Schematic illustration of the metasurface unit cell with cross-sectional planes. (b) Magnetic energy density distribution of 8 dominant resonant modes in the bandwidth from 820 nm to 1000 nm, at horizontal (top) and vertical (bottom) cross sections specified in (a). (c) Schematic illustration of a uniform array of nano-posts illuminated with a plane wave at normal incident. The amplitude of the transmission coefficient ($|t|$) and its phase (ϕ) are indicated in the illustration. (d) Contribution of 8 dominant resonant modes to the transmission of a periodic array of nano-posts with a diameter of 200 nm. The reconstructed transmission amplitude from these 8 modes is shown. (e) Transmission amplitude and phase of the periodic array of nano-posts, and reconstructed transmission amplitude and phase using the 8 dominant resonant modes. $|t_{RC}|$: reconstructed transmission amplitude, $|\varphi_{RC}|$: reconstructed transmission phase [75].

It is essential to emphasise that due to the presence of a high dielectric index material compared to a low refractive index substrate material, the coupling effect between unit cells is typically negligible [75, 78-82]. Though the meta-atoms are made of subwavelength nanostructures, their thickness can be comparable to the wavelength [75, 82].

Achieving high transmission requires minimal absorption within the designated spectral range in such a structure. It relies on the high refractive index with low absorption coefficients of dielectrics to ensure robust light confinement within the MSs' meta-atom. That is why each meta-atom can be considered as an individual truncated waveguide [75-77]. As a result, the transmittance coefficient is primarily determined by the nano scatterers' geometry, considering the negligible coupling effect between meta-atoms.

In this thesis, mainly a high-contrast MS is explored. Thus, I will elaborate more on this technique in the following chapters, explicitly depicting the phase modulation mechanism.

1.3 Applications

There is quite a long and highlighted list of functionalities enabled by MSs. The reason for such a variety is the ability of MSs to perform in a very small footprint, particularly in the optical regime, as of a few tens or hundreds of microns. MSs also show precise and unprecedented control over electromagnetic waves, e.g., employing phase discontinuity at the interface [13]. To this end, achieving such functionalities with traditional optics is challenging. In this section, I categorised some of the most popular applications in the following sub-sections [83-131].

1.3.1 Flat lenses

Flat lenses are among the most significant areas that hugely benefit from MSs. To begin with, traditional optics use the accumulated phase of bulky optics to create the desired functionality. While this approach is greatly appreciated in the optics society, bulky optics impose a practical limitation on many possible application scenarios simply because of the size and volume they take. Particularly, this matter is of great importance in the integration of optics, which is highly in demand simply due to the interest in having smaller devices. As MSs can mimic the operation of traditional optics, they offer the manipulation of the electromagnetic wave properties, including phase, amplitude, polarisation, and the direction of propagation. To this end, MSs can take the role of traditional optics with having a much smaller footprint and, in several cases, offering functionalities that are not possible by traditional optics, such as but not limited to miniaturised optical planar cameras, planar reflectors, and conformable structures for lensing and cloaking [38, 65, 73, 75, 77, 83-87]. Metalenses are another functionality of flat lenses enabled by MSs [88-92]. A lens made of MSs where meta-atoms can individually and precisely control the characteristics of the scattered light can offer functionalities through which aberration correction, extending the depth of focus, varifocal characteristics, and high numerical aperture (NA) lenses can be listed. Compared to conventional refractive or diffractive lenses, metalenses enabled by MSs can offer numerous advantages of bespoke functionalities. For instance, replacing the array of lenses with traditional optics has immensely reduced the volume of achromatic metalenses [92]. In addition to high NA, metalenses offer a high resolution for applications in direct laser lithography [93], microscopic imaging [94], and optical trapping [95-97]. The applications enabled by metalenses cover a wide variety of fields [98]. Here, I present an example to show their capabilities.

Imaging with subwavelength resolution demands lenses with a high NA, which can be satisfied by bulky and expensive objective lenses. However, MSs can offer a solution which is small in footprint and is planar. A shining example of a flat lens that enabled diffraction-limited focusing and subwavelength resolution imaging in the visible range is reported in ref [88]. Figure 1. 16 shows the unit cell design with meta-atoms made of titanium dioxide (TiO_2) and efficiency measurements for three different structures operating across the visible range. Figure 1.16(h) illustrates an image of the fabricated sample for this work.

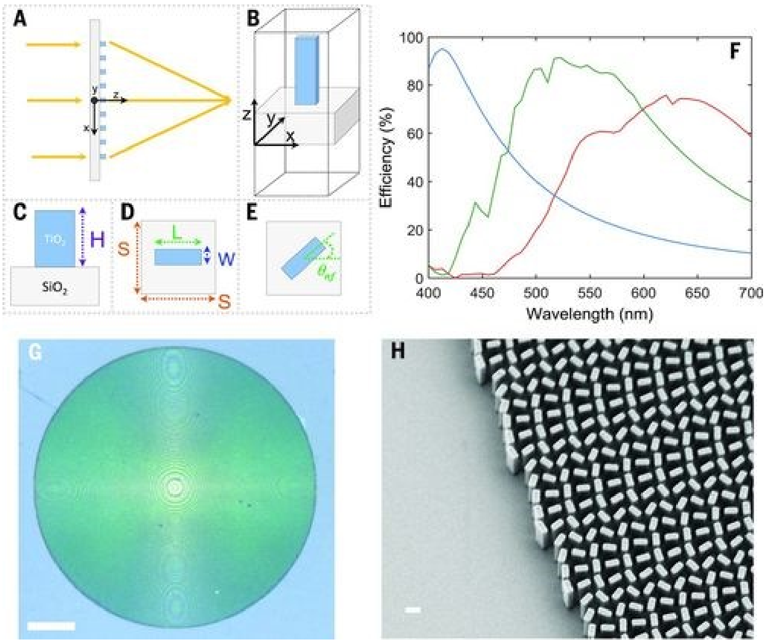

Fig. 1.16. (A) Schematic illustration of the metalens with its meta-atoms consists of TiO_2 nanofin. (B) schematic view of a TiO_2 nanofin on a glass substrate as a unit cell. (C, D) Side and top views of the unit cell showing height H, width W, and length L of the nanofin, with unit cell dimensions S × S. (E) The required phase is imparted by rotation of the nanofin by an angle θ_{nf}, based on the geometric Pancharatnam-Berry phase. (F) Simulated polarisation conversion efficiency as a function of wavelength. This efficiency is defined as the fraction of the incident circularly polarised optical power that is converted to transmitted optical power with opposite helicity. Periodic boundary conditions are applied at the x and y boundaries and perfectly matched layers at the z boundaries. Details of the three designs are as follows: for the metalens designed at λ_d = 660 nm (red curve), nanofins have W = 85, L = 410, and H = 600 nm, with centre-to-centre spacing S = 430 nm. For the metalens designed at λ_d = 532 nm (green curve), nanofins have W = 95, L = 250, and H = 600 nm, with centre-to-centre spacing S = 325 nm. For the metalens designed at λ_d = 405 nm (blue curve), nanofins have W = 40, L = 150, and H = 600 nm, with centre-to-centre spacing S = 200 nm. (G) Optical image of the metalens designed at the wavelength of 660 nm. Scale bar, 40 μm. (H) SEM image of the fabricated metalens with the shown scale bar, 300 nm [88].

This lens has reported a magnification of 170× with the ability to resolve structures with subwavelength spacing [88]. Hence, the compact design of these metalenses has the potential to facilitate the development of portable/handheld instruments for a variety of applications. Figure 1.17 presents an example of imaging with these metalenses and its comparison to commercial objectives.

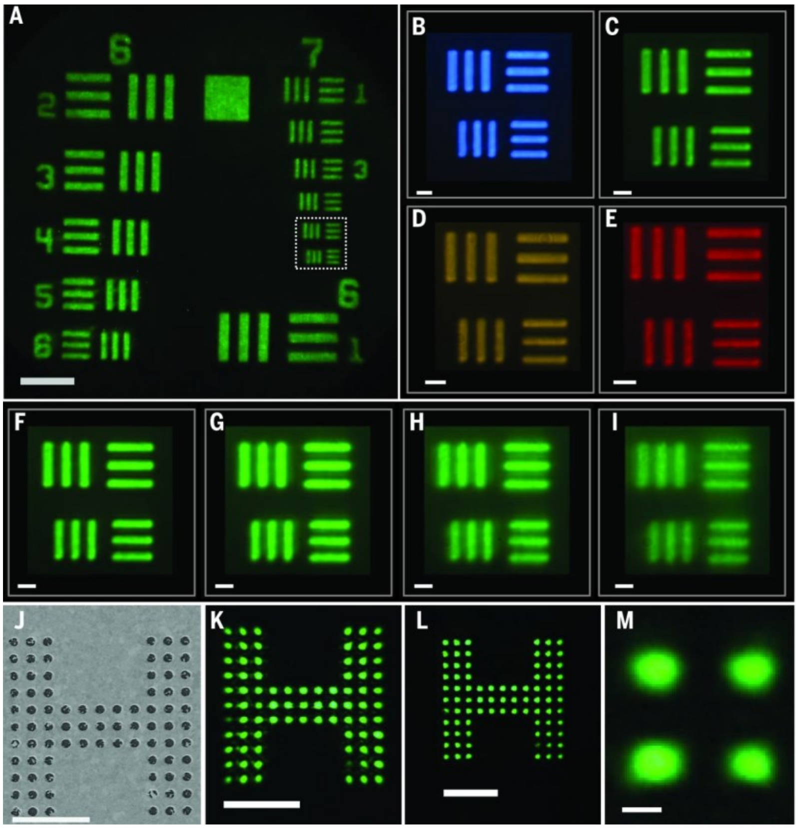

Fig. 1.17. Metalens imaging designed at λ_d = 532 nm with diameter D = 2 mm and focal length f = 0.725 mm.
(A) Image of 1951 USAF resolution test chart formed by the metalens taken with a DSLR camera. Laser wavelength is 530 nm. Scale bar is 40 µm. (B to E) Images of the highlighted region in Fig. 1.18(a) at wavelengths of (B) 480, (C) 530, (D) 590, and (E) 620 nm. Scale bar, 5 µm. (F to I) Images of the highlighted region in Fig. 1.18(a) at a centre wavelength of 530 nm and with different bandwidths: (F) 10, (G) 30, (H) 50, and (I) 100 nm. Scale bar is 5 µm. (J) Nanoscale target prepared by FIB. The smallest gap between neighbouring holes is approximately 800 nm. (K) Image of the target object (Fig. 1.18(j)) formed by the metalens. (L) Image of target object formed by the commercial state-of-the-art objective. Scale bar is 10 µm in Fig. 1.18, J to L. (M) Image formed by the metalens illustrates that holes with subwavelength gaps of ~450 nm can be resolved. The scale bar is 500 nm [88].

1.3.2 Holography

Reconstruction of the complex wavefront of the electromagnetic waves with both amplitude and phase information is called holography, first introduced by Gabor in 1947 [99]. Originally, it was an imaging technique that used the scattering of an incident coherent source when the incident light passed through an interface pattern to reconstruct the 3D optical features of a target object. I should emphasize that in this thesis, holographic imaging refers to the holographic image projection using a phase mask.

Holography has garnered significant interest since its utilisation in achieving cutting-edge 3D displays [100-101]. Recently, the emergence of MSs as the designated interface pattern has made the realisation of holographic applications feasible with the aid of MSs. The precise engineering of the phase of an optical beam, with high accuracy and spatial resolution, is ideally suited for applications in holography [102]. In the most popular form of holography with MSs, phase modulation of the incident light is required while the amplitude is almost unchanged [103-105]. To this end, there is a long list of holographic applications enabled by MSs [103-109]. In particular, the wavefront engineering capability is exploited to realise numerous applications in security [55], storage and manipulation of data [110-111], conformable platforms [47, 75], and several different areas [112-113]. Here, and through examples, the capability of holographic MSs, rather than summarising all the reported works, is discussed.

As an example to show the capability of MSs for holographic applications, a design procedure of a reflective type MS to make Einstein's portrait is shown in Fig. 1.18. In panel (a) of this figure, the incident light impinges the MS (patterned interface/hologram), and Einstein portrait as the target holographic image will be created in the designed distance and angle with respect to the normal MS plane. In panels (b-c), the phase profile of this hologram is shown. Realising this phase profile is achievable with the specific orientation

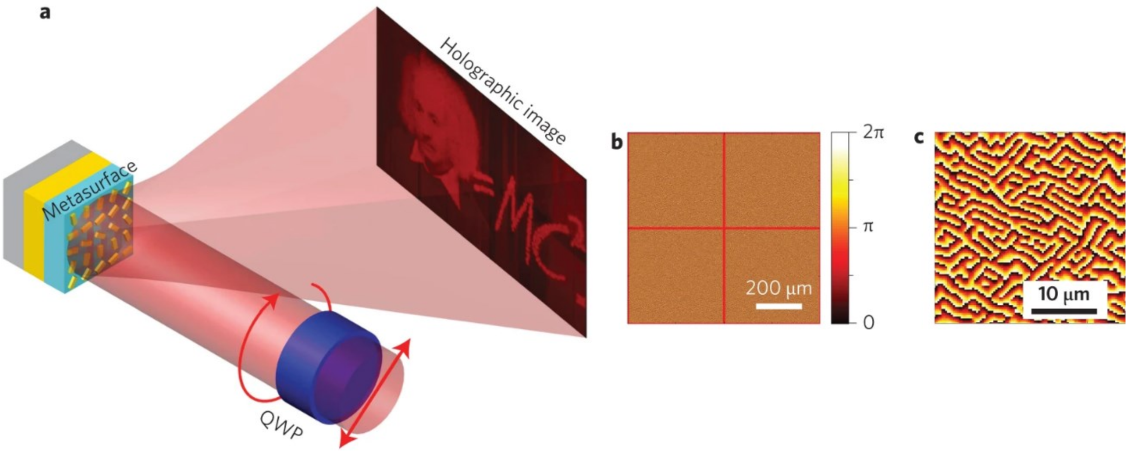

Fig. 1.18. (a) Illustration of the reflective nanorod-based computer-generated hologram under a circularly polarised incident beam. The circularly polarised incident beam is generated from a linearly polarised source that is passed through a quarter wave plate (QWP) and illuminates the metasurface. The reflected beam creates the holographic imaging in the far field. (b) The 16-level phase distribution with 2 × 2 periods designed to generate the target holographic image in the far field. (c) Enlarged phase distribution (100 × 100 pixels) of the upper-left corner of (b) [56].

of the meta-atoms that create the holographic image. This necessitates the incorporation of pixel-by-pixel design to guarantee the acquisition of the target phase profile.

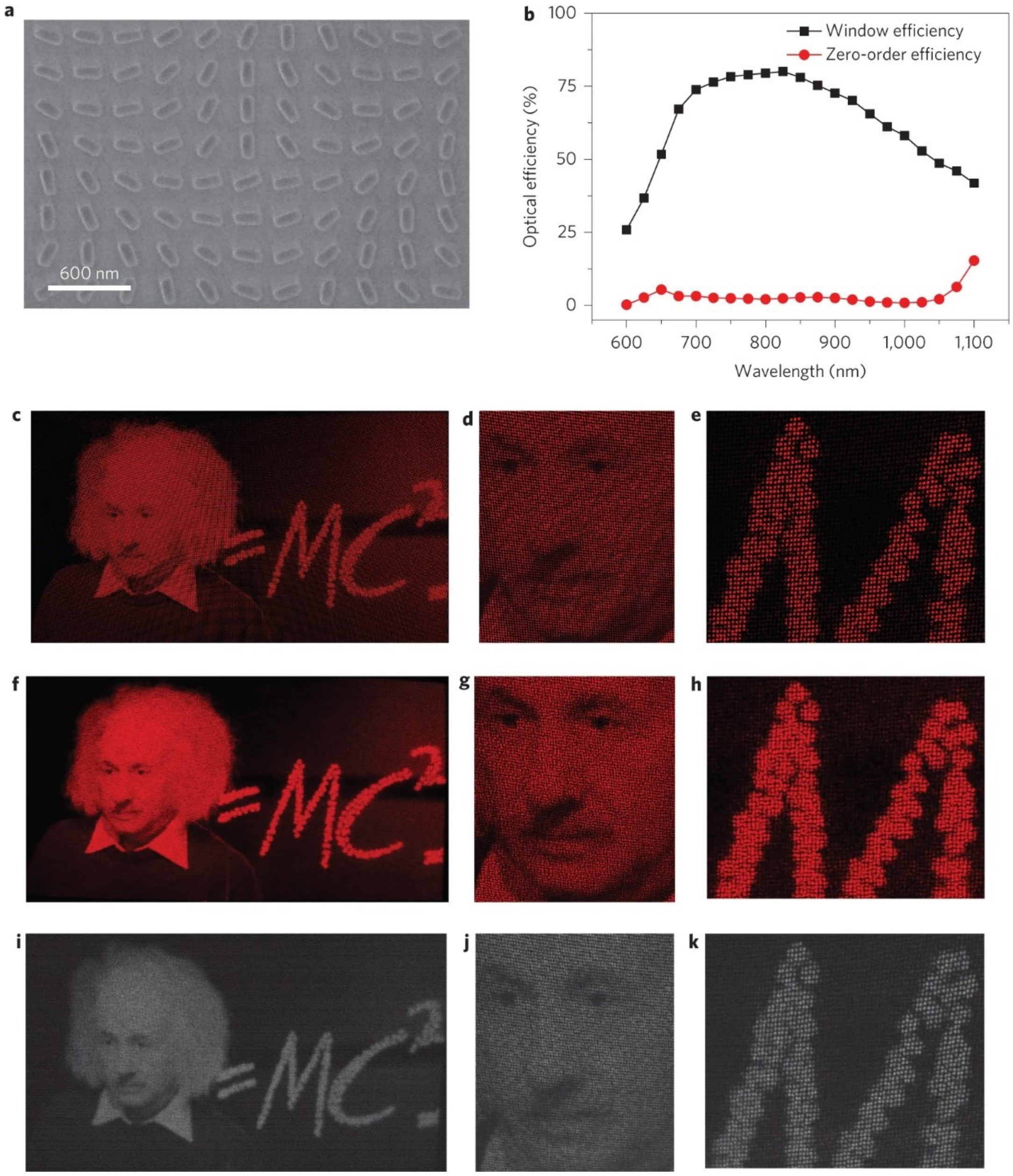

Fig. 1.19. Experimental holography using a nanorod-based metasurface. The created holographic image projection is taken using visible and infrared cameras. (a) SEM image of a portion of the fabricated nanorod array. (b) Experimentally obtained optical efficiency (determined by subtracting the zeroth-order beam signal from the image intensity) for both the image and the zeroth-order beam. The measurements show a high optical efficiency above 50% for the image beam over the range 630–1,050 nm. (c–e) Simulated holographic image of Einstein's portrait with an enlarged zoom of his face and the character ‘M’. (f–h) Experimentally obtained images captured by a ‘visible’ camera in the far field. The operating wavelength is 632.8 nm. (i–k) Experimentally obtained images captured by an infrared camera in the far field, with an operating wavelength of 780 nm [56].

Figure 1.19 shows the realisation of this design by demonstrating a Scanning Electron Microscopy (SEM) image of the fabricated sample and the measurement results. Panel (a) of this figure depicts how the meta-atoms are arranged in a different geometrical orientation, using the Pancharatnam-Berry technique to impose the required phase profile.

Panel (b) of this figure shows the measured efficiency of this structure versus wavelengths, including the visible range and near-infrared region. Figure 1.19(c-k) reports the simulated and measured images using a visible camera and an infrared camera. This example can be considered as a proof of concept that holography exploiting MSs can hold promise for several holographic functionalities [102-113].

As another example of optical holography, a significant progress in 3D imaging methods, this approach has obtained interest due to its capability to capture both the amplitude and phase information of the light scattered from objects. This functionality requires ultimate control over the complex phase in each hologram pixel. MSs can efficiently satisfy these requirements, allowing applications in holographic image projection [107].

MS holograms play a key role in creating the desired holographic function by encoding the information through the meta-atoms. For instance, Fig. 1.20 illustrates a simple idea of holographic image projection using a hologram [55].

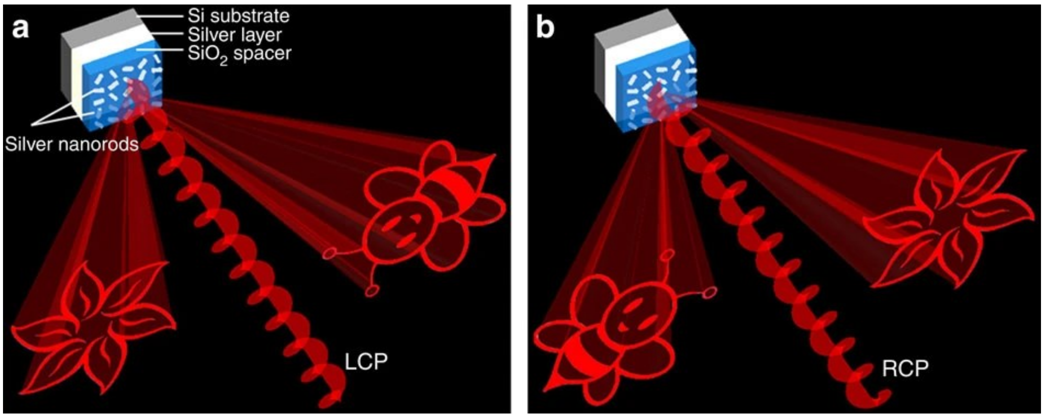

Fig. 1.20. Illustration of the effect of incident light on the created holographic images. The reflective-type metasurface consists of silver nanorods with spatially varying orientations on the top, a SiO_2 spacer (80 nm) and a silver background layer (150 nm) resting on a silicon substrate. (a) Under the illumination of LCP light, the holographic images 'flower' and 'bee' are reconstructed on the left and right side viewing from direction of the incident light, respectively. (b) The positions of the two holographic images are swapped when the helicity of incident light changes from LCP to RCP. The incident circularly polarised light excites the reflective-type metasurface at normal incidence and the reflected light that contributes to the images has the same polarisation as that of the incident light [55].

In panel (a), a left-handed circularly polarised (LCP) light impinges the hologram, creating two holographic images. Then, when the same hologram impinges by a right-handed circularly polarised (RCP) light, the holographic information is changed, specifically in this example, is rotated [55].

Full-colour holography is another interesting functionality proposed by MS-based holography [108]. For instance, Fig. 1.21 shows full-colour holography using both amplitude and phase modulations to reconstruct both two-dimensional (2D) and 3D holographic images [109]. There are various types of MS holograms with different characteristics, including performance, resolution, efficiency, polarisation selectivity, and full-colour operation. So, depending on the specific application's requirement, one can use an appropriate meta-atom.

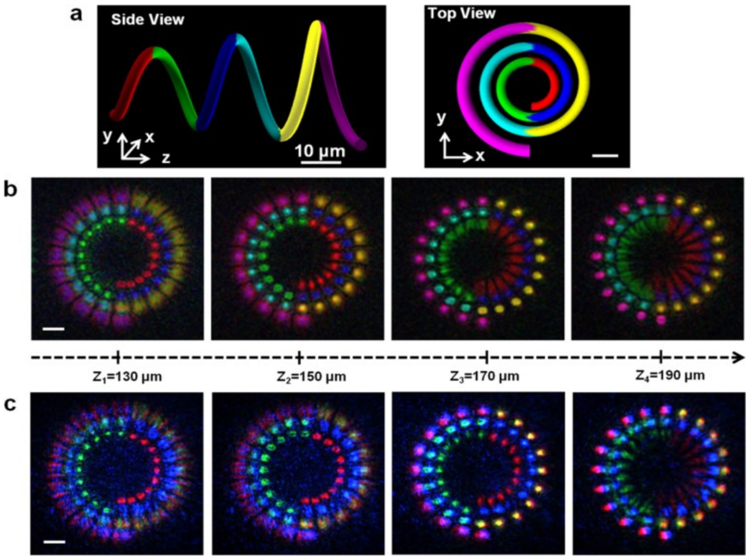

Figure 1.21. Reconstruction of 3D full-colour holographic images for a colour helix pattern with the aid of metasurfaces. (a) Side view and top view of the colour helix. (b) Simulated on-axis evolution of the holographic images of the colour helix on four 2D planes along the z direction. (c) Experimentally reconstructed 3D holographic images on different 2D planes. All the scale bars indicate 10μm [109].

1.3.2.1 Flexible holographic metasurfaces

Though having bespoke holographic MSs in a rigid and non-flexible substrate provides us with amazing functionalities, it would be more desirable to have them in a flexible and conformable platform. This can offer several advantages compared to that of MSs with rigid substrates.

First, nanoimprint lithography, as a high-throughput fulfilling industrial-scale manufacturing, offers roll-to-roll production of flexible MSs [114]. There is a substantial demand for roll-to-roll production to efficiently bring a high volume of MSs to the market due to its well-established technological maturity and cost-effectiveness [115-117].

Second, mechanical tuning of the flexible MS structure through stretching or vibration holds promise for new applications and functionalities such as searchability [119-122]. For instance, Fig. 1.22 qualitatively shows how the focal length of a MS lens can be tuned by stretching the flexible substrate.

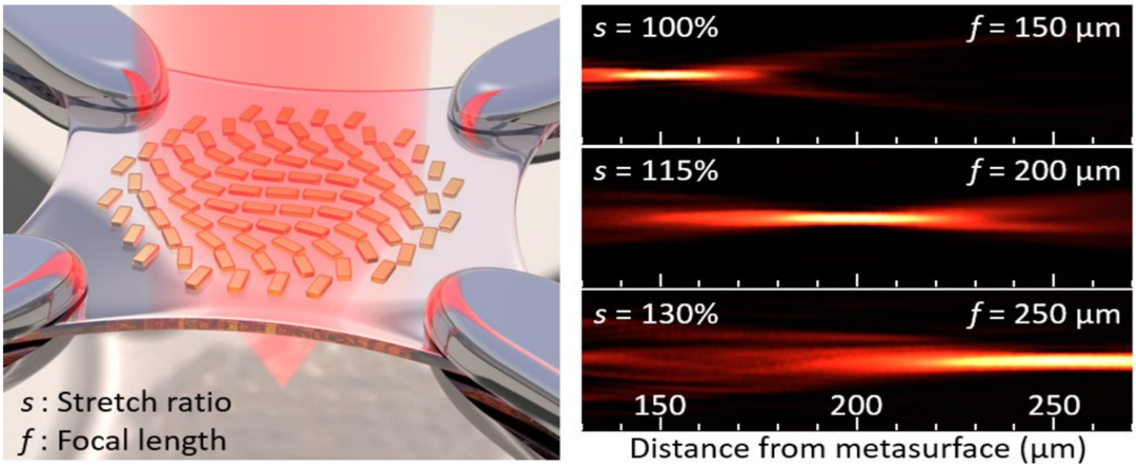

Fig. 1.22. A tunable metasurface on a stretchable substrate introduces a reconfigurable focal length of the structure. A schematic illustration of a metasurface on stretched PDMS is shown on the left image. The right image illustrates how the focal length of the metasurface is changed with regard to the stretchability of the substrate [118].

Most importantly, the conformability of flexible MSs, which can be applied to non-planar surfaces, introduces an excellent potential for several diverse applications [123-126], e.g., to apply ultrathin devices on contact lenses [127]. Additionally, flexible MSs can offer shape-dependent holographic applications, e.g., having MSs that the holographic information shown on the screen depends on how the MS is wrapped around the target object [106].

To shine a light on this concept, let us consider the capability offered by conformable MSs through this instance. Not surprisingly, the correlation between an object and its optical functionality is inevitable. For instance, a spherical lens focuses light on a point, while a cylindrical lens focuses light on a line. Now, consider a transparent object with an arbitrary shape. It will send the light passing through it to different points. Here, I explain how we can use flat lenses to decouple an object's geometry and optical functionality. Figure 1.23(a) illustrates a transparent arbitrary object covered by a planar thin layer. Figure 1.23(b) shows how light responds after passing through this object. Clearly, the light is not converging at a point. Fig. 1.23(c) depicts how the optical functionality of this object can be reformed as desired (focusing light to a point) by locally applying the phase profile required to create the desirable optical response [75].

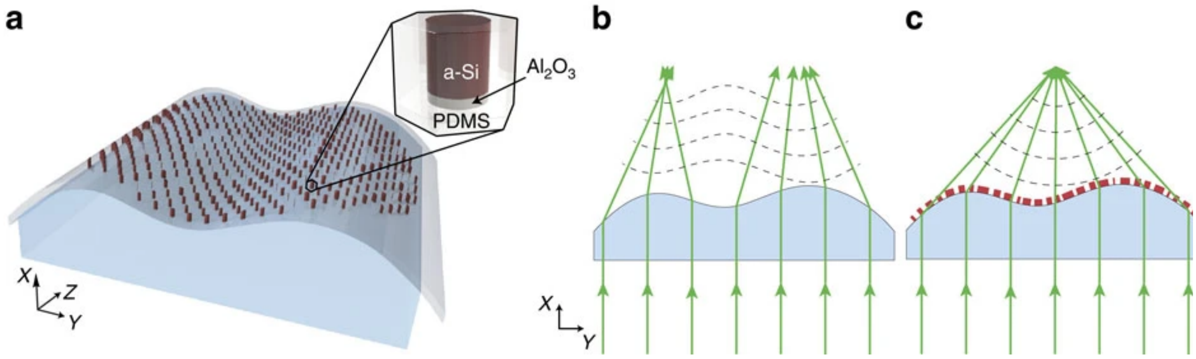

Fig. 1.23. (a) A schematic illustration of a dielectric metasurface layer conformed to the surface of a transparent object with arbitrary geometry. The inset draws the unit cell of the metasurface structure: an amorphous silicon (a-Si) nano-post on a thin layer of aluminium oxide (Al_2O_3) embedded in a low-index flexible substrate (PDMS for instance). (b) Cross-sectional view of the arbitrarily shaped object depicting how the object refracts light based on its geometry. As depicted, it generates an undesirable wavefront. (c) The same object with a thin dielectric metasurface layer conformed to its surface to manipulate its optical response to a desired wavefront [75].

First, the object without a flat lens layer is analysed and the phase profile of the optical waves transmitted through the outermost layer of the object is calculated. Then, along the outermost layer of the object, the optical path length and the corresponding optical path difference (OPD) of the rays transmitted through different points of the arbitrary object with respect to the chief ray are numerically calculated. Finally, exploiting an OPD-based approach, the required phase profile to realise the desired functionality is achievable [75].

As proof of concept, Fig. 1.24(a) reports the change in the focal length of a converging cylindrical lens from 8.1 mm to the desired value of 3.5 mm. This is done by adding a MS layer at the outermost layer of the cylindrical lens, as depicted in Fig. 1.24(a). Also, the measured intensity at the focal plane is shown on the right side of this panel. Figure 1.24(b) illustrates how a concave glass cylinder with a focal length of 12.7 mm using a planar MS layer is optically modified to focus the light 8 mm away from its surface. Again, the focal plane measurements are depicted on the right side of this figure. To this end, conformable holographic holograms are an excellent opportunity for real-life applications [105, 123, 125-126].

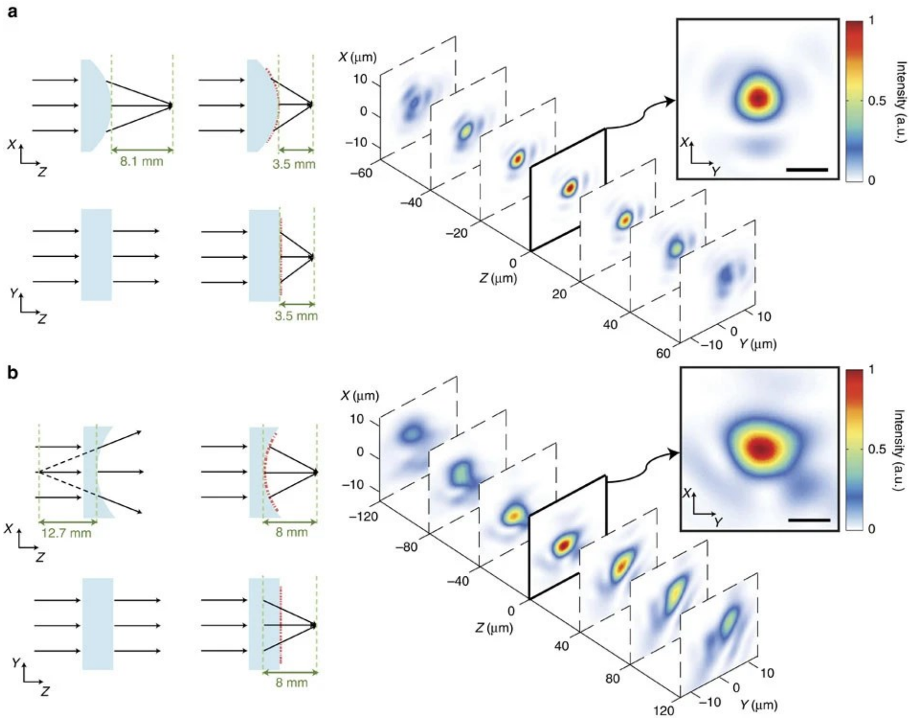

Fig. 1.24. Illustration of manipulating the optical response of a transparent object to a desired wavefront pattern. (a) A converging cylindrical lens with a radius of 4.13 mm and a focal distance of 8.1 mm is optically manipulated using a conformal metasurface with a diameter of 1 mm. The cylinder combined with the metasurface coated layer behaves as an aspherical lens with a focal length of 3.5 mm. (b) A different metasurface is mounted on a concave glass cylinder with a radius of 6.48 mm and a focal distance of 12.7 mm, which makes it focus to a spot 8 mm away from its surface (as an aspherical lens). Schematic illustrations (side and top views) are shown on the left, and intensities at planes parallel to the focal plane and at different distances from it are shown on the right. Intensities at the focal plane are depicted in the insets. The operational wavelength is 915 nm [75].

Shape-dependent holograms are one of the examples where the holographic image happens only if the hologram is placed in a specifically designed way [106]. The holographic information can either be robust with respect to deformation [47] or strongly dependent on the shape of support they are applied [75, 105-106]. This opens a new road and opportunities for new applications using holographic MSs. For example, Fig. 1.25 illustrates a reflective type MS working in the visible spectrum. It shows how the holographic information can be severely distorted when the polarisation of incidence and the substrate shape is changed (see caption) [105].

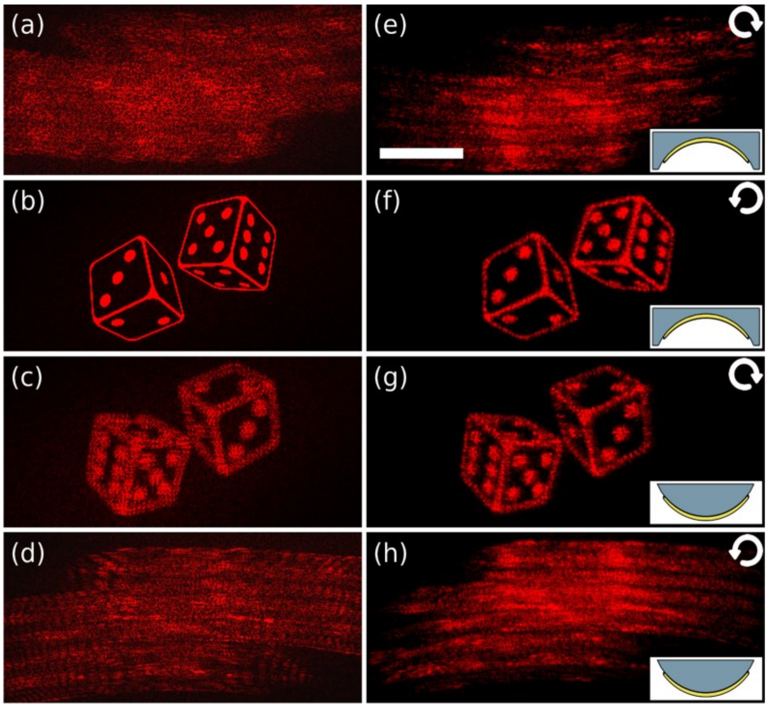

Fig. 1.25. (a–d) Simulated holographic image projections; (e–h) Experimental holographic image projection. (a, e) and (b, f) were taken on a concave substrate with a radius of curvature of 6 mm. (c, g) and (d, h) were taken on a convex substrate with identical radius of curvature. (a, e) and (c, g) were taken with right-handed circularly polarised incident light. (b, f) and (d, h) were taken with left-handed circularly polarised incident light. The left-handed circularly polarised images are naturally rotated 180° about the *z* axis in the *xy* plane. The scale bar is 10 mm [105].

Figure. 1.26 shows another example of how holographic information can depend on the form of support [106]. This increases the potential applications of holographic MSs.

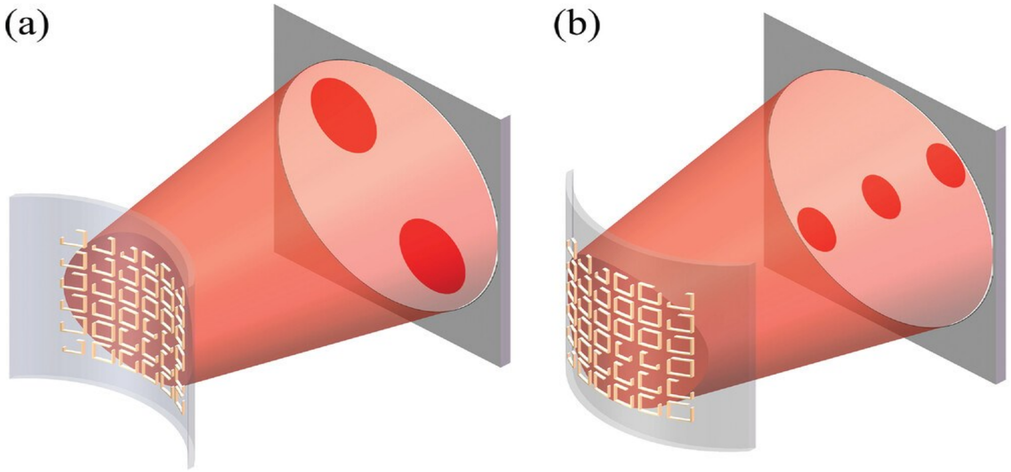

Fig. 1.26. Shape-dependent conformable holographic MSs, where the projected pattern will change depending on how it is conformed on an object. (a) MS applied to a convex object depicting two points, (b) the same MS applied to a concave object depicting three points [106].

In conclusion, holographic MSs can play a pivotal role in optical technologies, given the bespoke functionalities. A holographic MS can be more functional by making it flexible. Flexibility offers more potential for real-life applications.

1.3.3 Other applications

Given that usually, the scale of molecules and cells is in the range of hundred microns to hundred nanometres, biologists and photonics engineers are actively collaborating on some projects to study the biological particles of interest through the nano-photonics tools. Interestingly, optical MSs are made from meta-atoms whose dimensions scale from a few hundred nanometres to a few microns. This introduces various applications using MSs in biology [128-129].

From bioimaging to biosensing, MSs can play a significant role in studying biological particles [128-129]. Its valuable role in optical chiral imaging, endoscopic optical coherence tomography, fluorescent imaging, super-resolution imaging, magnetic resonance imaging, and quantitative phase imaging is fully described in ref [130]. Besides, in biosensing applications, antibodies and proteins, DNAs, cells, and cancer biomarkers are detected using these fascinating 2D structures [130-131].

Furthermore, MSs enable extraordinary abilities to guide, block, absorb, concentrate, and disperse waves both on the surface at grazing incidence and in space at normal and oblique incidences. Figure 1.27 schematically illustrates this concept for some of these properties [7]. The existence of such a potential to manipulate the characteristic features of the scattered light opens up a window of appealing applications, some of which have already been discussed.

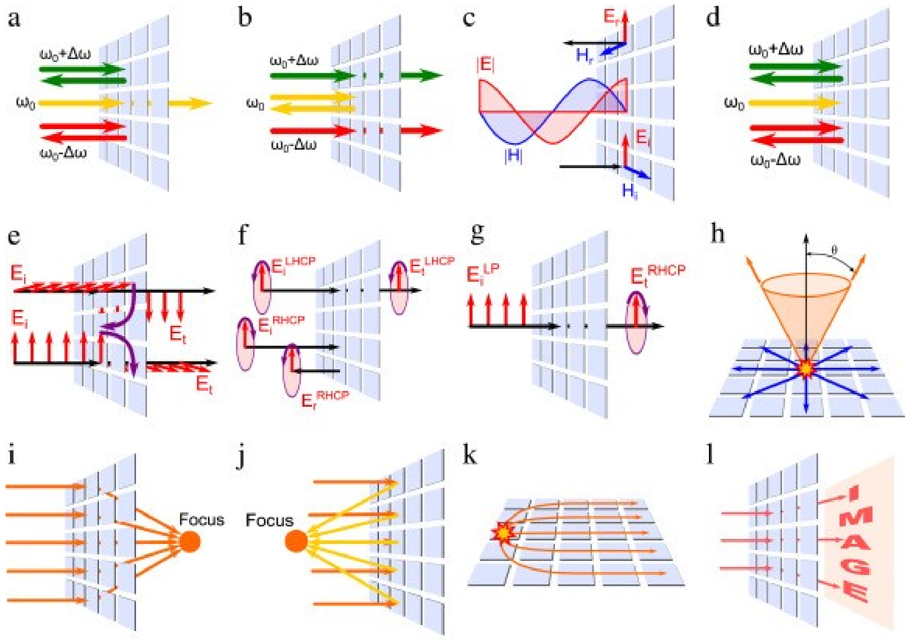

Fig. 1.27. Illustrating various functionalities enabled by metasurfaces: (a) band pass frequency selective surface; (b) band stop frequency selective surface; (c) high-impedance surface; (d) narrowband perfect absorber; (e) twist polariser; (f) right-handed circular-polarization frequency selective surface; (g) linear-to-circular polarisation converter; (h) two-dimensional leaky wave antenna with a conical-beam pattern; (i) focusing transmit array; (j) focusing reflect array; (k) flat Luneburg lens; (l) hologram [7].

1.4 Thesis structure

This introductory chapter has established the fundamental principles that underpin this work.

Chapter 2 illustrates the design and modelling used in this work. First, it outlines a numerical method to design holograms using a well-known technique. Secondly, It details the design of novel meta-atoms.

Chapter 3 describes the fabrication procedures for the different MSs of this study. This chapter contains a significant novelty in nanofabrication. Hence, the challenges are appropriately reported, and the solutions are discussed.

Chapter 4 outlines the experimental setups exploited in this study.

Chapter 5 disseminates a novel conformable polymeric MS membrane in the visible spectrum. The proposed design can facilitate mass-scale production of holographic MSs.

Chapter 6 communicates the concept, hologram design, and experimental results of holographic optical trapping and image projection in the visible range using a quiet novel transmissive MS platform.

Chapter 7 conveys work on incoherent holographic MSs. In particular, the concept, hologram design, and experimental results are discussed.

Finally, chapter 8 summarises the work of this thesis and describes the outlook.

Chapter 2

Modelling

This thesis is principally concerned with the creation of holographic MSs. In this chapter, I present all aspects of the numerical modelling required to design a holographic MS for a given application. First, I will present how existing computer-generated holography methods can be used to design a phase-modulating mask that can shape light into a desired pattern. Secondly, I will discuss how I numerically designed new meta-atoms that will be used as the basic building blocks of these phase masks. In particular, I introduce new meta-atom designs that allow us to introduce new materials that have not been previously harnessed in MS design. Specifically, I describe the design for the zirconium dioxide (ZrO_2) meta-atoms in the visible range, which is a novel material for MS engineering and is the most used meta-atom throughout the majority of this thesis. I also introduce the design of a new meta-atom for conformable visible light MSs.

2.1 Design of holographic metasurfaces

There exist different approaches for designing holograms that directly can be applied to MSs. Among these methods, the point source algorithm, Genetic algorithm, and Gerchberg-Saxton algorithm (GSA) can be mentioned [132-133]. A conjugate gradient minimisation-based hologram calculation technique is another approach that uses a spatial light modulator and offers high-fidelity phase and amplitude control [134]. In this thesis, I used GSA and explained this approach here. It generates the hologram from the target image using the source intensity and other parameters, such as the source shape, wavelength and the hologram pitch. The GSA propagates the light between two spatially separated planes, the hologram plane and the holographic image plane. As a phase retrieval algorithm, it converges to the right solution of the hologram through many iterations [135]. Figure 2.1 illustrates the schematic view of this algorithm, with a Gaussian source intensity distribution and a smiley face as the target image. Here, I describe it through even steps: 1) set the holographic image as the target image. 2) Back-propagate the holographic image to the hologram plane. 3) Replace the intensity achieved by propagation with the intensity of the source. 4) Propagate the updated complex field to the holographic image plane. 5) Replace the intensity with the intensity of the target image. 6) Calculate the least square differences of the absolute values between the holographic image and target image, and repeat steps 2-6 if this value is greater than a pre-defined value. 7) Return the hologram phase.

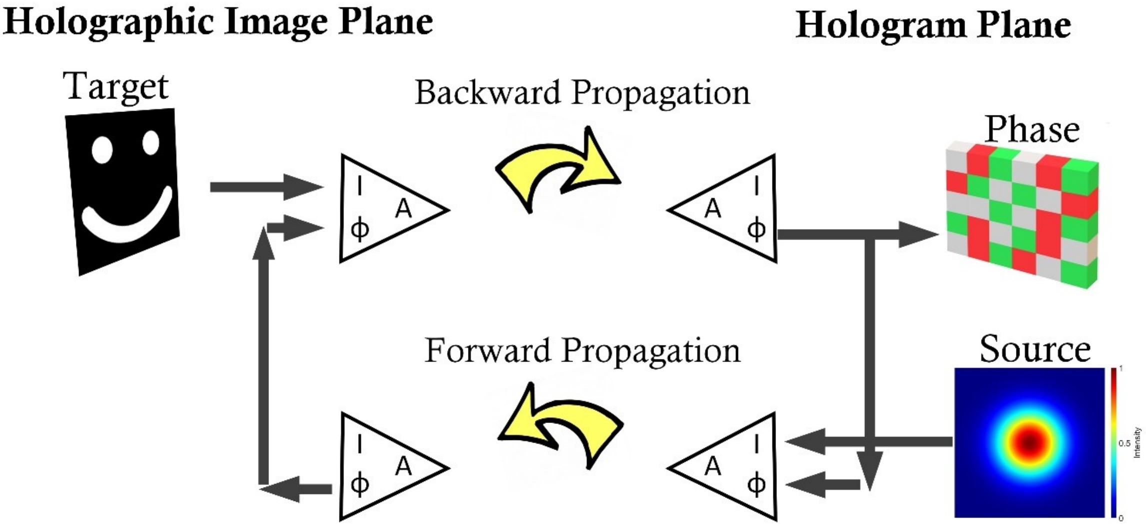

Fig. 2.1. Graphical illustration of the GSA(A, Φ, and I represent amplitude, phase, and intensity, respectively).

These propagations are achievable through a Fast Fourier Transforms (FFT) or a numerical integration method. The FFT method is simple to implement and ideal to generate a simple hologram. For instance, Appendix A presents a simple MATLAB code to generate a hologram using the FFT method. However, in some cases, the FFT is not suitable to describe light propagation, e.g. when the image plane is not flat and not distant enough from the hologram plane. In these cases, it is best to use numerical integral methods, such as the Rayleigh-Sommerfeld (RS) method [105, 136]. It gives the freedom to design the coordinates of the hologram, e.g. to design a curved or arbitrarily shaped hologram, at the desired distance between the hologram and holographic planes. Hence, the RS method opens up an opportunity to design conformable MSs.

The RS numerical integral method in the cartesian coordinate is derived as below [105, 136]:

$$U(x_I,y_I,z_I)=-\iint U(x_O,y_O,z_O)\frac{2(z_I-z_O)}{|r_I-r_O|}\times\left(ik-\frac{1}{|r_I-r_O|}\right)\times\frac{\exp(ik|r_I-r_O|)}{4\pi|r_I-r_O|}dx_O dy_O \quad , \tag{2.1}$$

where U is the complex light fields at the coordinates (x_j, y_j, z_j), identified by position vector r_j, the subscripts j= I, O refer to the holographic image and hologram (MS) planes respectively, and *k* is the wave vector. The origin of the coordinate system is the centre of a virtual, undistorted hologram plane, as denoted in Fig. 2.2.

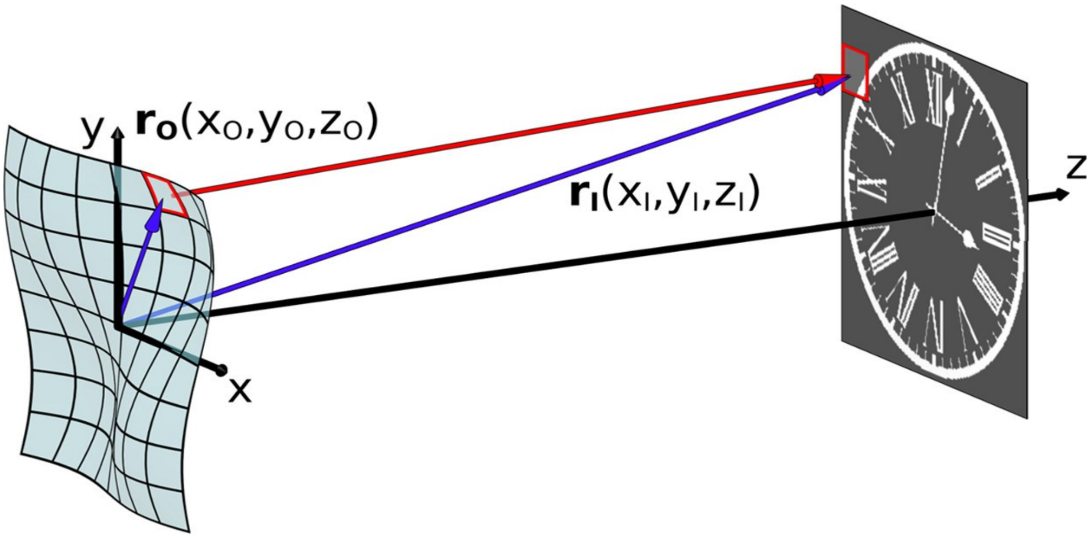

Fig. 2.2. Illustration of light propagation using the RS equation from $\mathbf{r}_O(x_O, y_O, z_O)$ to $\mathbf{r}_I(x_I, y_I, z_I)$ [105, 136].

Propagating light through the numerical integral can require intense computational power, as the propagation is evaluated point by point. Given this, an approximation is needed where the number of points increases.

The Fraunhofer condition defines Far-field as distance ≥ 2 × D^2/λ, where D is the maximum linear size of the antenna source and λ is the wavelength [137]. In this region, the radiated energy at a given angular distribution is constant, and the power decays based on the inverse square law with distance.

Full details of these approximations are presented in [136]. Here, I summarised them by presenting the outcome.

In the near-field, the term *ik* is dominated by the larger values of $\frac{1}{|r_I - r_O|}$ term [138]. As a result, equation (2.1) can be written as [136]:

$$\begin{aligned} U(x_I, y_I, z_I) \approx & -\iint U(x_O, y_O, z_O) \frac{2(z_I - z_O)}{|r_I - r_O|} \\ & \times \frac{1}{|r_I - r_O|} \times \frac{\exp(ik|r_I - r_O|)}{4\pi|r_I - r_O|} dx_O dy_O \end{aligned} \quad . \tag{2.2}$$

The Far-field (Kirchoff) approximation disregards the contribution of the near-field components and considers only the far-field terms [138]. In far-field, the fractional term $\frac{1}{|r_I - r_O|} \to 0$. Consequently, equation (2.1) can be derived as [136]:

$$\begin{aligned} U(x_I, y_I, z_I) \approx & -\iint U(x_O, y_O, z_O) \frac{2(z_I - z_O)}{|r_I - r_O|} \\ & \times ik \times \frac{\exp(ik|r_I - r_O|)}{4\pi|r_I - r_O|} dx_O dy_O \end{aligned} \quad . \tag{2.3}$$

The Fourier approximation requires a few assumptions to convert equation (2.1) to FFT under certain conditions. The most pivotal points employed by the assumptions are far-field operation and a physically small holographic image compared to the distance between two spatially separated planes, the hologram and holographic image planes [139]. Under these assumptions, by defining:

$$\begin{aligned} v &= \frac{x_I}{\lambda(z_I - z_O)} \\ u &= \frac{y_I}{\lambda(z_I - z_O)} \end{aligned} \quad , \tag{2.4}$$

equation (2.1) can be written as:

$$U(u, v) \approx \frac{1}{z_I - z_O} \iint U(x_O, y_O) \times \exp(-2\pi i(ux_O + vy_O)) dx_O dy_O \quad . \tag{2.5}$$

Considering the standard two-dimensional Fourier transform, this equation can be derived:

$$F(u, v) \approx \iint f(x, y) \times \exp(-2\pi i(ux + vy)) dx dy, \tag{2.6}$$

and finally,

$$U(u,v) \approx \frac{1}{z_I - z_O} FFT(U(x_O, y_O)) \quad . \tag{2.7}$$

Independently of the used approximation, the intensity of a given light field U_j at a given position (x_j, y_j, z_j) can be defined as:

$$I(x_j, y_j, z_j) = |U(x_j, y_j, z_j)|^2, \tag{2.8}$$

and the corresponding phase can be derived as:

$$\phi(x_j, y_j, z_j) = \arctan\left(\frac{\mathrm{Im}(U(x_j, y_j, z_j))}{\mathrm{Re}(U(x_j, y_j, z_j))}\right), \tag{2.9}$$

where Im and Re represent the imaginary and real parts of U(x_j, y_j, z_j), respectively.

Notably, amplitude-only holograms modulate the amplitude information to encode the hologram while keeping the overall phase constant. This amplitude modulation is usually achievable by engineering point-by-point the absorption of the hologram. While this approach is simple, it ends in a low-efficiency hologram owing to the absorption of a portion of the incident light.

On the other hand, phase-only holograms use the modulation of the phase information while keeping the overall amplitude information constant. Thus, it offers higher achievable efficiency compared to amplitude-only holograms.

Holograms that use both amplitude and phase modulation to encode the information create the highest quality holographic images as they regenerate the complete information of the hologram [140, 141].

Throughout this thesis, phase-only holograms were used as they are simpler to fabricate while exhibiting similar efficiencies to that of full holograms.

2.1.1. Implementation of the GSA with RS integration

In this thesis, all the hologram designs are made using the GSA method with the RS numerical integral method as the light propagator.

The key parameters are:

1. **Hologram resolution**: it mentions the number of hologram pixels, e.g. 100×100.
2. **Holographic image resolution**: it refers to the number of holographic image pixels, denoting the resolution, e.g. 1000×1000.
3. **Hologram pixel pitch**: it refers to the periodicity of the meta-atoms used to encode the hologram.
4. **Holographic image pixel pitch**: it indicates the holographic image's pixel size.
5. **Source intensity**: Gaussian distribution or a plane wave can be used.
6. **Wavelength**: it refers to the propagation wavelength between the hologram and holographic image planes.
7. **Closest separation z**: it conveys the distance between the hologram and holographic image planes.
8. **Holographic image offset**: it states the position of the holographic image with respect to the x- and y-axis.

Using GSA with the FFT and RS numerical integral in the far-field approximations, a simple hologram with 100 iterations is designed with the parameters listed in Table 2.1.

Table. 2.1. **Hologram parameters.**

Parameter	**Value**
Hologram resolution	500×500
Holographic image resolution	100×100
Hologram pixel pitch	400 nm
Holographic image pixel pitch	0.7 mm
Source intensity	Plane-wave
Wavelength	488 nm
Closest separation z	200 mm
Holographic image offset in x-y-z	-50,50,0 mm

Figure 2.3(a) shows the target image. The simulated holographic image using RS numerical integral approximation in the far-field is depicted in Fig. 2.3(b). FFT approximation result is illustrated in Fig. 2.3(c). Finally, the phase profile of this hologram shown in panel b) is presented in Fig. 2.3(d).

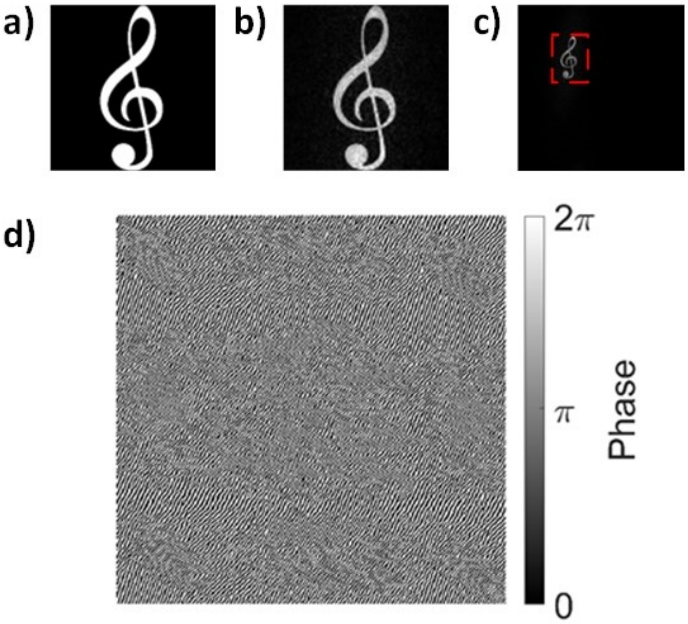

Fig. 2.3. GSA hologram design, a) target image. Simulated holographic image using b) RS numerical approximation illustrates the designed image shown in the red box in section (c), and c) Simulated image using FFT approximation with the off-set consideration (see Table 2.1), d) RS numerical approximation phase profile.

With this setting, the size of the holographic image is 70×70 mm^2.

The phase profile obtained by the GSA can then be implemented with MS, where each meta-atom imparts the required phase to the scattered field. In the following, I will present the design of meta-atoms used in this thesis.

2.2 Meta-atom designs

This section presents three different meta-atom designs of which two are novel. Here, the aim is to design phase-only holograms in transmission. Therefore, the meta-atoms need to provide phase modulation with high transmission. Following this, this section details the optical response of the designed meta-atoms when they are made of different materials. In particular, first, it introduces ZrO_2 as the core material of the most used unit cell for this thesis. Then, it discusses the meta-atoms made of ZrO_2, SU-8, and polymethyl methacrylate (PMMA).

2.2.1 Introduction to zirconium dioxide (ZrO_2)

Zirconium dioxide, known as zirconia, is an oxide of zirconium. It offers an excellent weakly-dispersive-like optical response in the ultraviolet (UV) and visible range. Due to its unique properties, it can be suitable for a variety of purposes across many industries, including biomedical implants [142], protective coating layers [143-144], and optical materials [145]. It is most famous for producing hard ceramics [146-147], while it is widely used for the production of various dental implants due to its hardness, chemical unreactivity, and biocompatibility [148]. Having excellent resistance to corrosion and different chemicals, very high fracture toughness, high hardness and density, good frictional behaviour, low thermal conductivity, solid electrical insulation and generally long lifetime make this material interesting to be used in light-matter interactions [149]. Besides, ZrO_2 can be deposited relatively fast and at low temperatures. These properties of ZrO_2 make it a great candidate to be employed for the technology offered by MSs in areas such as light-matter interaction applications, including but not limited to holography, optical trapping, and biomedical applications.

The visible range is of primary importance due to its relevance to human vision. ZrO_2 has a moderately high refractive index in the visible range, with low dispersion. Besides, it is transparent as a thin-film material. Therefore, ZrO_2 shows untapped potential to be used as the dielectric material for MSs operating in the visible range. Figure 2.4 illustrates the typical real and imaginary parts of the refractive index of amorphous ZrO_2, used in this work. The film was deposited via Atomic Layer Deposition (ALD) and measured via ellipsometry, as further discussed in the next chapter. Throughout the entire visible spectrum, ZrO_2 exhibits a refractive index greater than 2 and negligible losses.

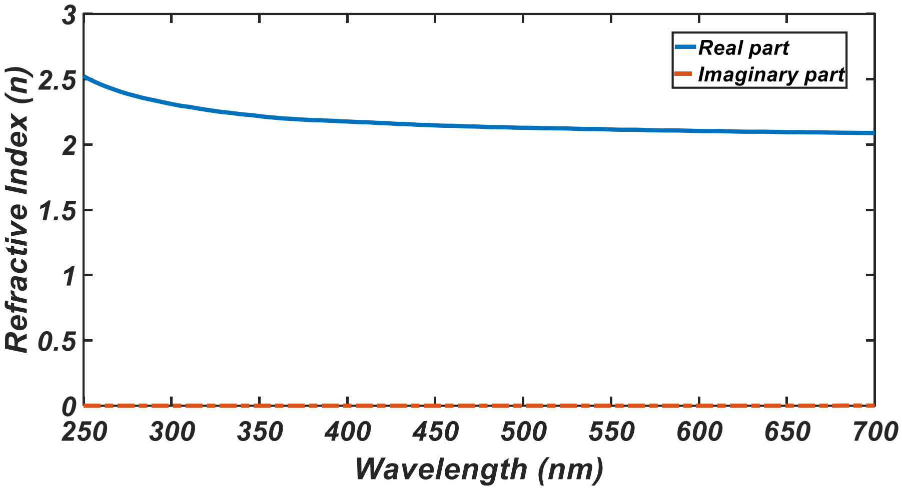

Fig. 2.4. The measured ZrO_2 refractive index.

2.2.2 Pillar meta-atoms

Here, I discuss the meta-atom design which is made of a pillar on a substrate. Figure 2.5 illustrates the unit cell design of the ZrO_2 pillar meta-atoms. It consists of a thick microscope glass as a substrate, a layer of 50 nm Indium Tin Oxide (ITO) as a conductive layer to reduce the effect of electron backscattering, and ZrO_2 pillars with height t_a = 650 nm. The meta-atoms are arranged in a hexagonal lattice with p= 350 nm. The change in their radius creates the required phase response. In this example, the operating wavelength is λ=632.8 nm.

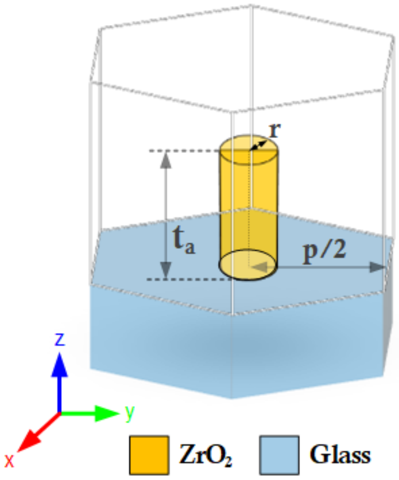

Fig. 2.5. Schematic view of the ZrO_2 pillar meta-atoms.

The meta-atom is designed to work in an air environment. The design is done using commercial multi-physics software COMSOL [150], where the dispersion data of microscope glass (bk7), ITO, and ZrO_2, measured by Ellipsometer, are used to model this unit cell. In the design, a linearly polarised (E-field on the x-axis) plane wave illuminates the structure at normal incidence. To minimise the simulation time, symmetrical boundary conditions have been applied in xz and yz planes where the z-axis is considered as an open space boundary. These conditions are applied throughout all the simulations with COMSOL for the rest of this section's designs.

The radius sweep of 20 nm to 175 nm provides high transmission with the phase modulation offered by the meta-atoms, as depicted in Fig. 2.6. This design provides 0-2π phase modulation, which is crucial for phase-only holograms.

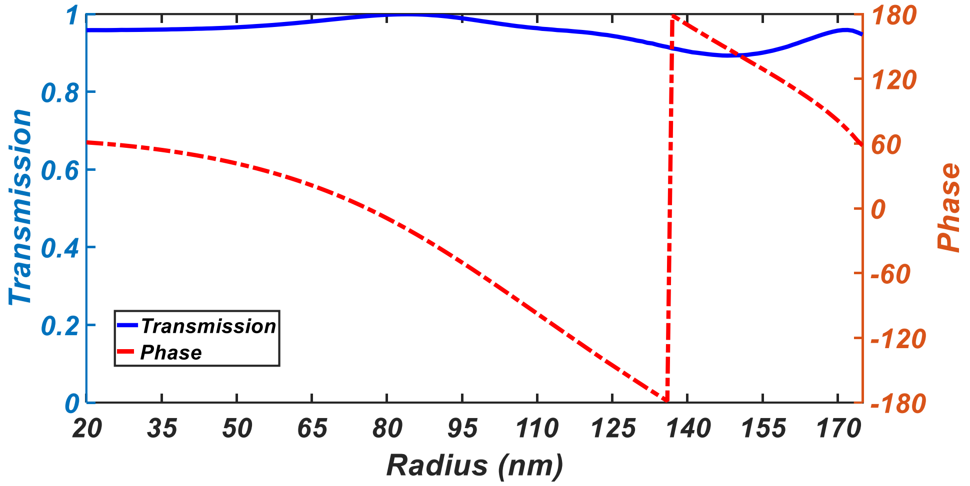

Fig. 2.6. COMSOL simulation results of the transmission and phase of ZrO_2 nanopillars of differing radius, for a wavelength of 632.8 nm.

Figure. 2.7 depicts the electric field (E-field) distribution for a simulated structure. This structure considers a quarter of two pillars in a rectangular shape combined with the boundary conditions, to apply the hexagonal lattice constant. As expected, the electric field distribution is strong inside the pillars and the coupling between them is negligible.

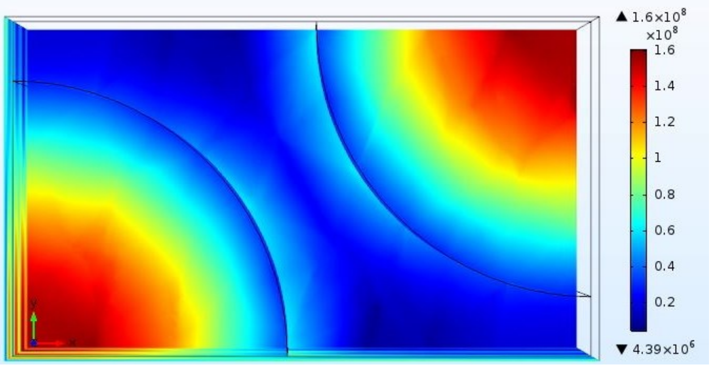

Fig. 2.7. E-field distribution of the ZrO_2 pillar meta-atom (r = 140 nm) designed at λ = 632.8 nm.

It is noteworthy to mention that this unit cell design is versatile within the visible range as long as the meta-atoms are considered to work in subwavelength dimensions. Thus, depending on the application, these meta-atoms can be designed for other visible wavelengths while providing qualitatively the same results.

This design is similar to that used in [151-152], providing full-phase coverage with high transmission. In my case, given the hardness of ZrO_2 and due to the required fabrication scheme, this design is not very practical. Therefore, I developed the following design, which has less ideal performance but offers other benefits such as easier fabrication and a more robust structure.

2.2.3 Pillar with top meta-atoms

Figure 2.8 shows a novel ZrO_2 meta-atom structure. It offers an independent optical response of the meta-atoms due to the top ZrO_2 cap, as this flat layer physically separates the ZrO_2 meta-atoms from the medium they are designed to work. To fabricate the previous design, it was necessary to pattern a photoresist and then deposit ZrO_2, followed by an etch-back step and then remove the photoresist. However, in this design, the etch-back step followed by removal of the photoresist is not required, which is the main difference between this design and the previous one. This will be further discussed in Chapter 4 where I detail the fabrication of meta-atoms.

As illustrated, the unit cell comprises a thick microscope glass as a substrate, a 50 nm thin layer of ITO, ZrO_2 pillars as the core material with the height t_a, and radius r, embedded

in PMMA, a ZrO_2 top cap, with a hexagonal lattice constant p consisting of a triangular shape. The lattice constant, height of ZrO_2 pillars, and atop cap can be optimised depending on the application and operational wavelength. Further, the operational medium atop the ZrO_2 flat cap can be chosen as desired. Here, I considered air for holographic applications and water for biological applications, where the meta-atoms operate in a microfluidic environment to interact with biological samples of interest.

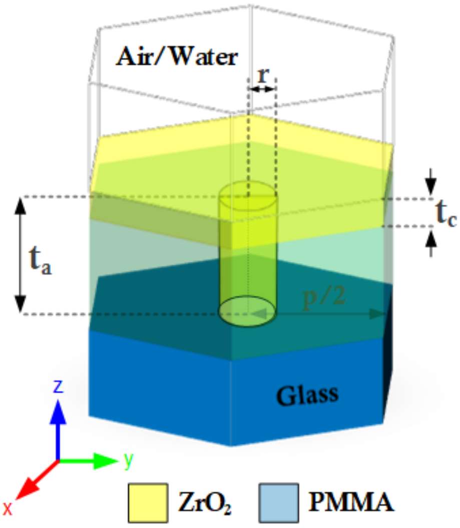

Fig. 2.8. Schematic view of the ZrO_2 pillar with top meta-atoms.

2.2.3.1 ZrO_2 meta-atom designs for holographic applications at 488 nm and 532 nm

This design considers air as the operational medium for the meta-atoms. Given the perspective of the unit cell presented in Fig. 2.8, I designed meta-atoms to encode holograms at 488 nm and 532 nm with the details provided in Table 2.2.

Figure 2.9 illustrates the transmission and phase modulation of these meta-atoms. The achieved phase modulation at $\lambda = 488$ nm and $\lambda = 532$ nm is 300° and 265°, respectively. The resonances shown in Fig. 2.9(a) are mainly due to the comparable scale of the lattice constant with the illuminated wavelength. These resonances can be removed by reducing the lattice constant size. For instance, the resonances disappeared in Fig. 2.9(b) due to the decrease of the lattice constant and increase of the operational wavelength.

Table. 2.2. **Meta-atom parameters at 488 nm and 532 nm, designed for holographic applications.**

	Parameter	**Value**
488 nm	Operational wavelength	488 nm
	Lattice constant (p)	400 nm
	Radius scan (r)	20-200 nm
	ZrO_2 pillar height (t_a)	700 nm
	ZrO_2 atop cap (t_c)	180 nm
532 nm	Operational wavelength	532 nm
	Lattice constant (p)	300 nm
	Radius scan (r)	20-150 nm
	ZrO_2 pillar height (t_a)	700 nm
	ZrO_2 atop cap (t_c)	180 nm

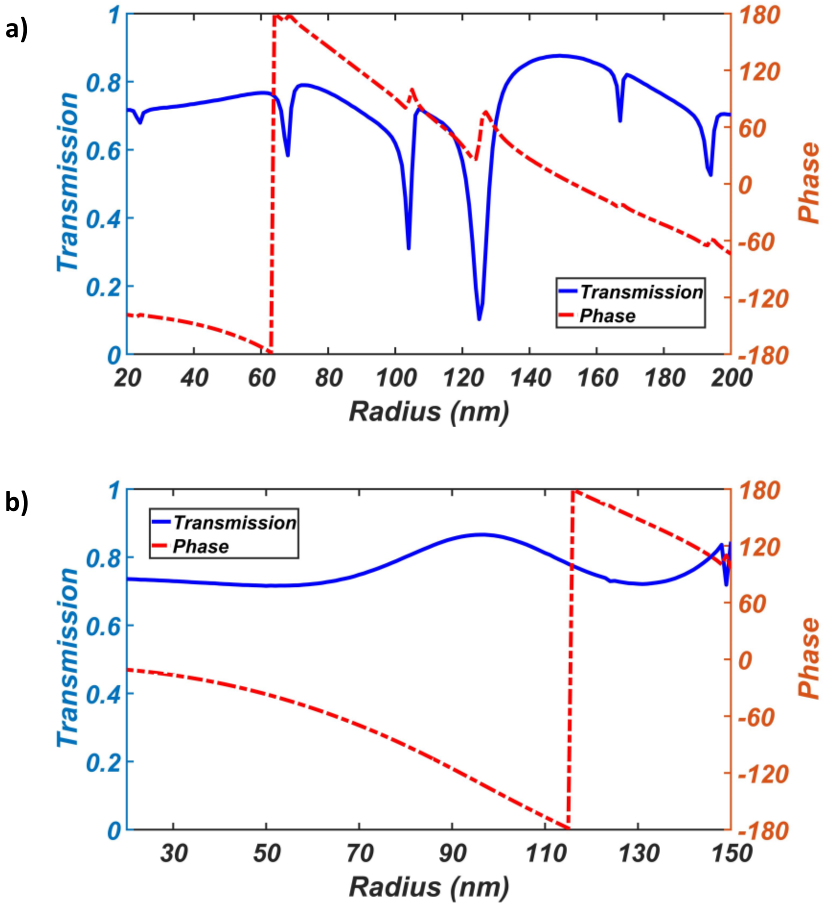

Fig. 2.9. Optical response of the meta-atoms designed at (a) 488 nm, and (b) 532 nm for holographic applications.

However, in the practical implementation of the meta-atoms designed at λ = 488 nm, I did not use the resonance areas to realise the required phase shift. Table 2.3 reports on the 16-level phase quantisation for these designs. It should be emphasised that the ZrO_2 pillar height for both cases is identical, but the phase coverage is not the same. The structure provides less phase modulation at larger operational wavelength, e.g. at the case of λ = 532 nm. Nevertheless, this can be solved by increasing the aspect ratio of the pillars. This, however, is not only a matter of design but also depends on the accessible nanofabrication facilities.

Table 2.3. **16-level phase quantisation for meta-atoms at 488 nm and 532 nm.**

488 nm	**Phase**	-168°	-146°	-123°	-101°	-78°	-56°	-33°	-11°
	Radius	57 nm	17 nm	-	-	-	187 nm	174 nm	159 nm
	Phase	11°	33°	56°	78°	101°	123°	146°	168°
	Radius	147 nm	137 nm	115 nm	109 nm	96 nm	88 nm	79 nm	71 nm
532 nm	**Phase**	-175°	-152°	-130°	-107°	-85°	-62°	-40°	-17°
	Radius	114 nm	104 nm	96 nm	87 nm	77 nm	66 nm	53 nm	31 nm
	Phase	5°	27°	50°	72°	95°	117°	140°	162°
	Radius	-	-	-	-	-	143 nm	134 nm	123 nm

Figure 2.10 shows the E-field distribution for the designed structure at λ = 532 nm. The electric field confinement is strong inside the pillars. However, this E-field distribution is different from that of the previous design as there is PMMA between the meta-atoms.

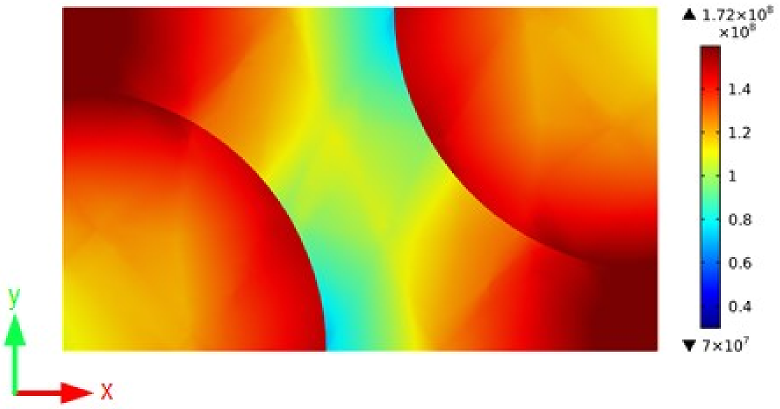

Fig. 2.10. E-field distribution of the meta-atom (r = 115 nm) designed at λ = 532 nm for holographic applications.

2.2.3.2 ZrO_2 meta-atom designs for optical trapping applications at 488 nm and 532 nm

The NA of a lens plays an important role when it comes to optical trapping applications. Here, the goal was to design a high numerical aperture metalens using ZrO_2 meta-atoms for optical trapping at 488 nm. Hence, the lattice constant is chosen to be small enough to satisfy the required NA. This comes with slightly less phase modulation offered by the meta-atoms and imposes a practical limitation on the maximum achievable NA. Full details of the relation between the lattice constant and the numerical aperture of a metalens are discussed in chapter 6 of this thesis. Table 2.4 reports the meta-atoms parameters for both designs at 488 nm and 532 nm.

Table. 2.4. **Meta-atom designed parameters at 488 and 532 nm for optical trapping applications.**

	Parameter	**Value**
488 nm	Operational wavelength	488 nm
	Lattice constant (p)	200 nm
	Radius scan (r)	10-100 nm
	ZrO_2 pillar height (t_a)	700 nm
	ZrO_2 atop cap (t_c)	180 nm
532 nm	Operational wavelength	532 nm
	Lattice constant (p)	210 nm
	Radius scan (r)	10-105 nm
	ZrO_2 pillar height (t_a)	700 nm
	ZrO_2 atop cap (t_c)	180 nm

The operation of these meta-atoms is considered in two different media, where atop ZrO_2 cap can be air (used for characterisation) or water (used for optical trapping experiment) as the operational medium. The transmission and phase modulation of the unit cells for these two scenarios are shown in Fig. 2.11(a-b). These meta-atoms offer higher transmission when they are considered to work in water rather than air. This increase in transmission for the water case is expected as the wave encounters a less refractive index change when it passes through the ZrO_2 cap to water rather than the air case. Here, the achieved phase modulation for structures optimised at 488 nm and 532 nm is slightly smaller than those of larger lattice constants, decreasing to 290° and 255°, respectively.

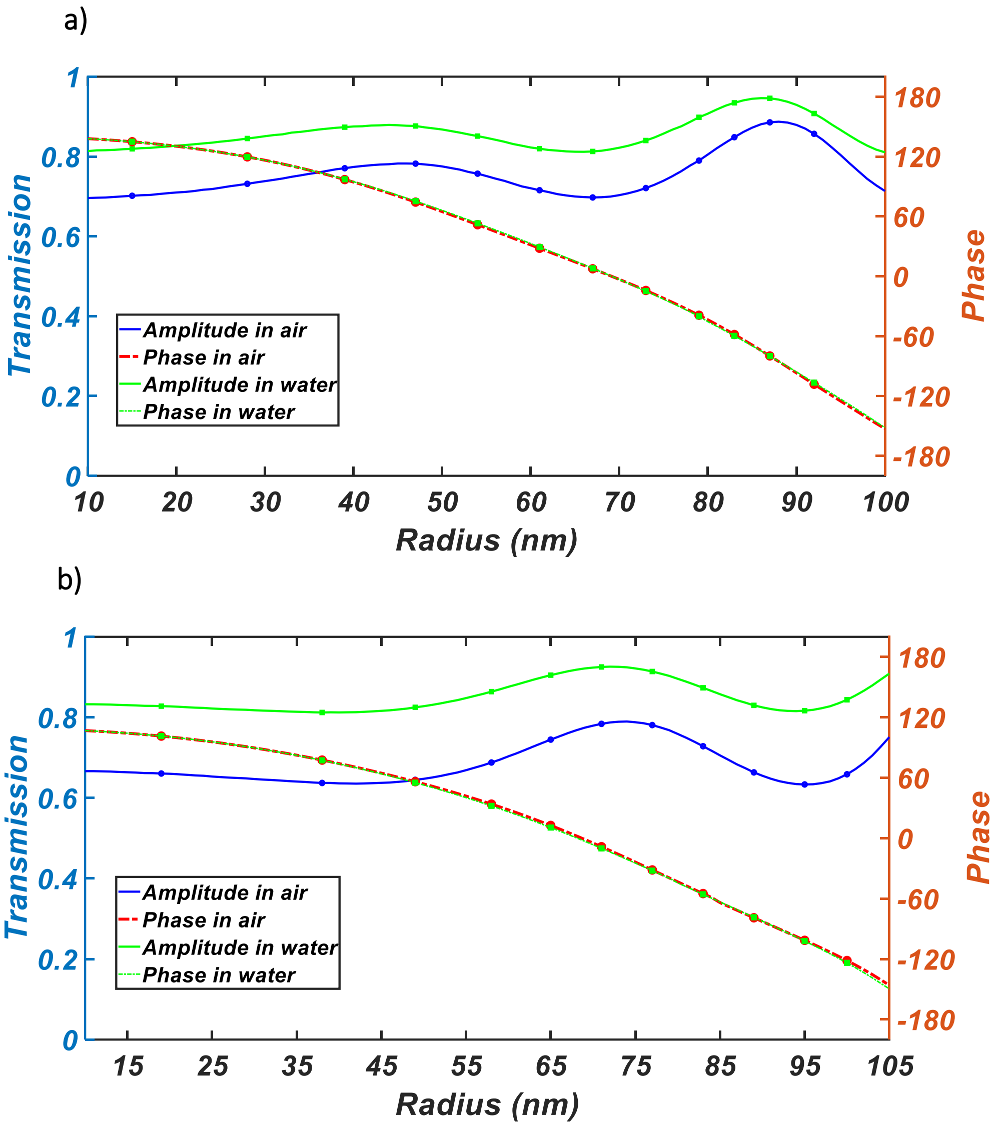

Fig. 2.11. Optical response of the meta-atoms designed at (a) 488 nm and (b) 532 nm for optical trapping applications.

Importantly, owing to the medium-independent response of meta-atoms, the phase modulation for the air and water cases is the same.

Table 2.5 reports on the phase quantisation of the meta-atoms for both wavelengths. Notably, this quantisation can be used for air or water as the operational medium.

Table 2.5. **16-level phase quantisation for meta-atoms at 488 nm and 532 nm.**

488 nm	**Phase**	-173°	-150°	-128°	-105°	-83°	-61°	-38°	-16°
	Radius	-	-	-	92 nm	87 nm	83 nm	79 nm	73 nm
	Phase	7°	29°	52°	74°	97°	119°	142°	164°
	Radius	67 nm	61 nm	54 nm	47 nm	39 nm	28 nm	15 nm	-
532 nm	**Phase**	-168°	-146°	-123°	-101°	-78°	-56°	-33°	-11°
	Radius	-	-	100 nm	95 nm	89 nm	83 nm	77 nm	71 nm
	Phase	11°	33°	56°	78°	101°	123°	146°	168°
	Radius	65 nm	58 nm	49 nm	38 nm	19 nm	-	-	-

2.2.4 Air-hole meta-atoms

This section presents a novel approach for designing meta-atoms with high transmission and complete phase modulation while the unit cells are made of a single material. Importantly, this method can be implemented using any suitable material having the ability to be processed, to create patterned membranes. Here, using two popular high-contrast photoresists, SU-8 and PMMA, I present all polymeric MS membranes. Then, I show how this approach can be extended for the silicon case.

2.2.4.1 Design of SU-8 meta-atoms

SU-8, a very popular epoxy-based, negative tone resist that can be patterned using photolithography and electron beam lithography. Besides, it shows a relatively high average refractive index $n_p \simeq 1.58$ within the visible range with a negligible absorption coefficient. Figure 2.12 illustrates the schematic view of this unit cell. It consists of an air cylinder with the height t_a and radius r, in a hexagonal lattice constant p consisting of a triangular shape. The substrate is made of the same material and the change in its thickness (t_p) qualitatively has minimal effect on the optical response of the meta-atoms. In this configuration, the radius of the air pillar determines the phase of the transmitted light.

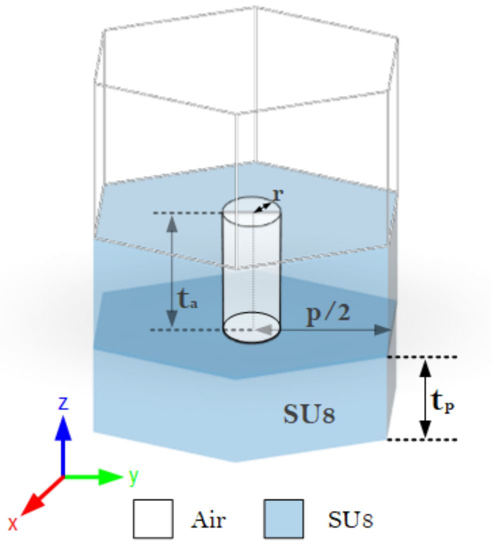

Fig. 2.12. Schematic view of the SU-8 meta-atoms.

The unit cell was numerically modelled with COMSOL commercial finite element software. To minimise the simulation time, symmetrical boundary conditions in the xz and yz planes were applied, and adopted open boundary conditions for the z-axis were considered. The designed parameters for meta-atoms optimised at λ=532 nm are presented in Table 2.6. Figure 2.13 illustrates the phase modulation and transmission of this unit cell for varying air cylinder radii, for polarisation aligned along the x and y axes. As seen, it reveals a polarization-independent response due to the symmetry of the air hole in the unit cell.

Table. 2.6. **SU-8 meta-atom designed parameters at 532 nm for holographic applications.**

Parameter	**Value**
Operational wavelength	532 nm
Lattice constant (p)	300 nm
Radius scan (r)	20-150 nm
Air hole pillar height (t_a)	1000 nm
SU-8 substrate (t_p)	0.0 nm

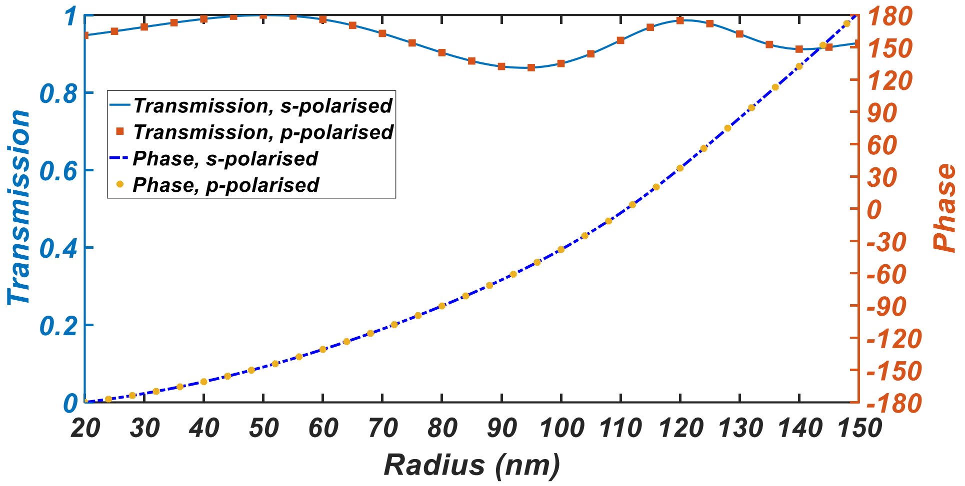

Fig. 2.13. Optical response of the SU-8 meta-atom designed at 532 nm for holographic applications.

Table 2.7 reports on twelve-level phase quantisation for the practical implementation of these meta-atoms.

Table 2.7. **12-level phase quantisation for SU-8 meta-atoms at 532 nm.**

Phase	-175°	-145°	-115°	-85°	-55°	-25°	5°	35°	65°	95°	125°	155°
Radius	26 nm	51 nm	68 nm	82 nm	94 nm	104 nm	113 nm	120 nm	127 nm	133 nm	139 nm	145 nm

The effect of the geometrical parameters on the response of the meta-atoms, sketched in Fig. 2.12, is numerically modelled and shown in Fig. 2.14(a-b). Panel a) of this figure shows how the transmission and phase of the transmitted light are affected by the air cylinder height, in a range of ±30% around the nominal value. In this range, the phase coverage of the structure spans from $3\pi/2$ to $5\pi/2$, with a marginal effect on the amplitude of the transmitted light. Not surprisingly, the thickness of the membrane that guarantees a 2π coverage of the phase is higher than λ/n_p since the presence of the air region reduces the effective index of the unit cell.

Figure 2.14 (b) shows the optical response of the meta-atoms for varying substrate thickness. The results show that the phase coverage is unaffected, and the transmission changes are qualitatively not different. Likewise, changing the lattice constant p produces qualitatively similar results, provided that the subwavelength condition is retained. Figure 2.15 reports on the optical response of the meta-atoms with the same parameters as

Table 2.6 but a lattice constant p = 400 nm. For larger p, the phase changes less quickly with the radius. This could help to manage potential fabrication imperfections, as deviation from the intended meta-atom size would lead to more contained local error in the phase.

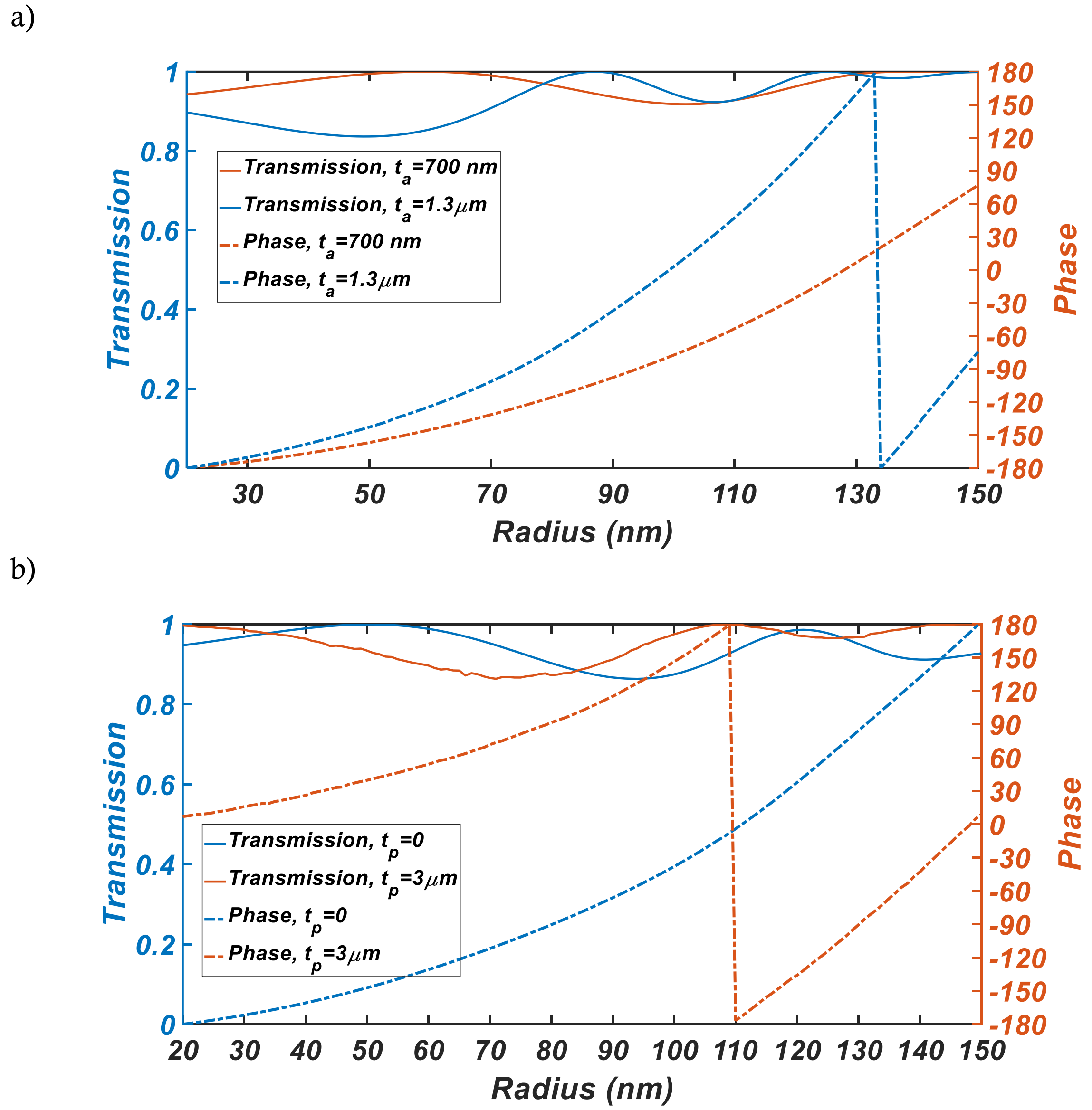

Fig. 2.14. Optical response of the SU-8 meta-atoms with regards to geometrical variation in (a) the air hole cylinder height, and (b) the SU-8 substrate thickness.

Figure 2. 16(a-b) depicts the E-field distribution of this meta-atom in the xy and xz planes. Panel a) illustrates the confinement of the electric field in the SU-8 area.

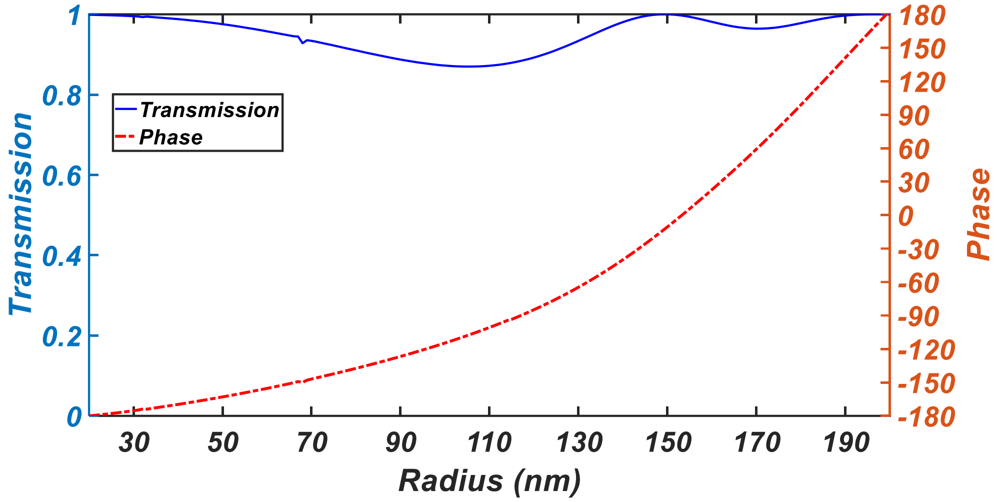

Fig. 2.15. Optical response of the SU-8 meta-atom designed at 532 nm with p = 400 nm.

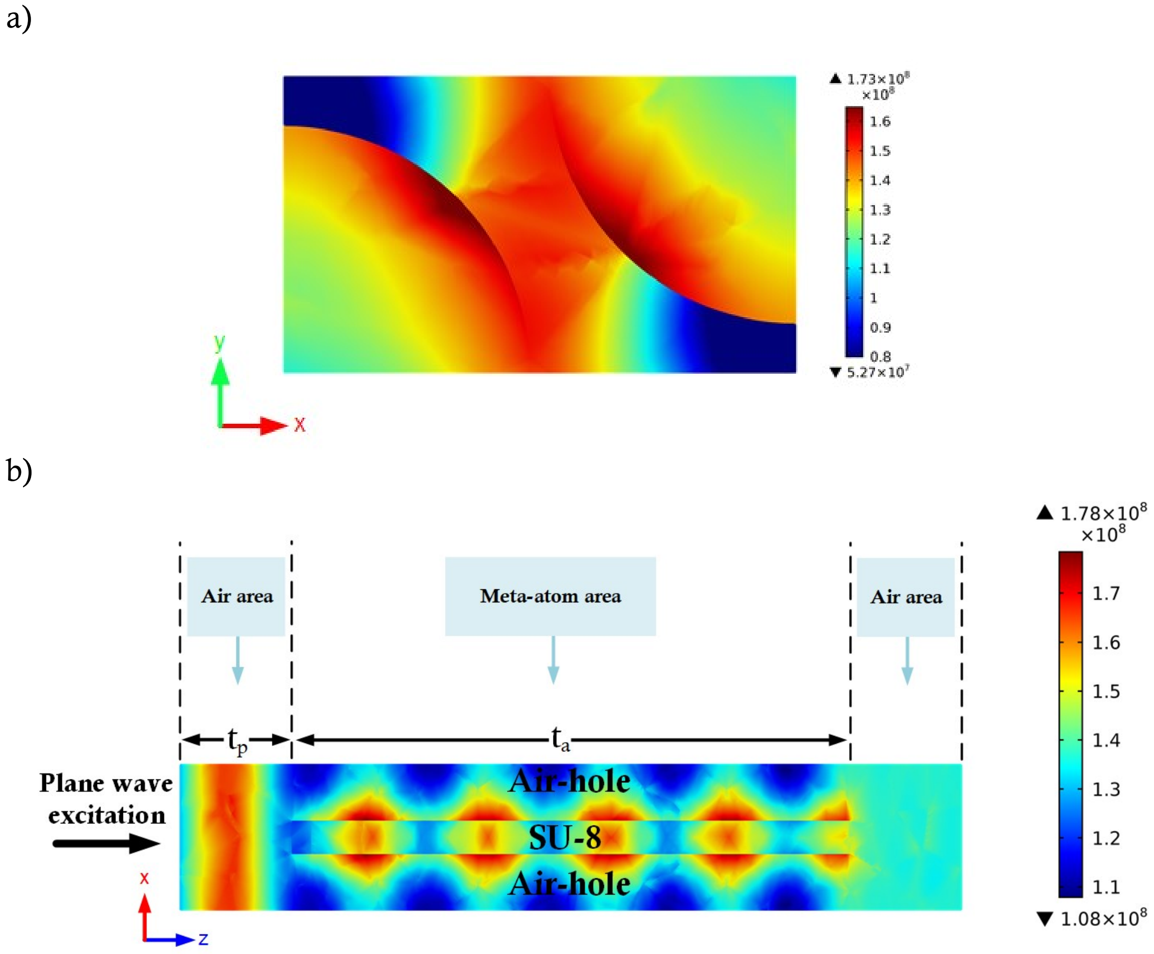

Fig. 2.16. E-field distribution (excited with a y-polarised plane wave) of the SU-8 meta-atom (r = 125 nm) designed at λ = 532 nm for holographic applications. (a) shows E-field at z = 530 nm plane, and (b) illustrates E-field at y = 75 nm plane.

However, panel b) gives a more intuitive view of how the light is propagating through this structure.

2.2.4.2 Design of PMMA meta-atoms

As mentioned, the designed unit cell provided in Fig. 2.12 is versatile for a suitable material with the ability of Nanopatterning. PMMA, a transparent high-resolution positive photoresist, offers a good membrane platform for the implementation of polymeric MSs as it can be patterned using photolithography and electron beam lithography. It offers a slightly lower average refractive index $n_p \simeq 1.49$ within the visible range with a negligible absorption coefficient. The unit cell of this design is presented in Fig. 2.17, where PMMA meta-atoms are designed at $\lambda = 532$ nm. Again, the same boundary conditions as of the SU-8 case were applied in the COMSOL simulations.

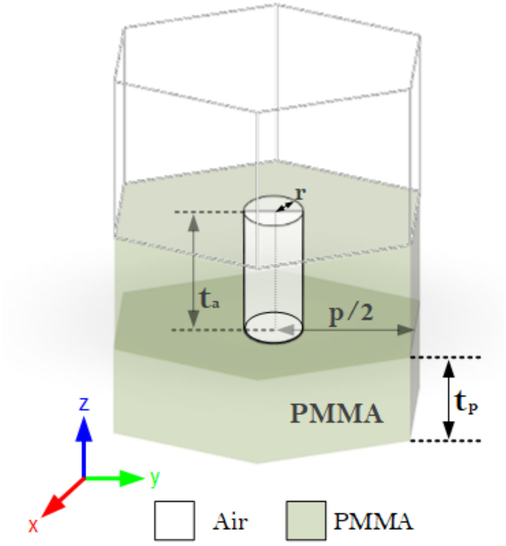

Fig. 2.17. Schematic view of the PMMA meta-atoms.

The designed parameters are reported in Table 2.8. As expected, the smaller refractive index of PMMA compared to SU-8 resulted in slightly taller air cylinders in the unit cell.

Table. 2.8. **PMMA meta-atom designed parameters at 532 nm for holographic applications.**

Parameter	**Value**
Operational wavelength	532 nm
Lattice constant (p)	300 nm
Radius scan (r)	20-150 nm
Air hole pillar height (t_a)	1170 nm
PMMA substrate (t_p)	0.0 nm

Figure 2.18 reports on the transmission and phase modulation of this unit cell. This structure offers a high transmission while the phase modulation covers 0-2π. Again, and likewise, to the SU-8 unit cell, the change in the periodicity qualitatively produces the same results as long as the subwavelength condition is considered. Table 2.9 reports on the twelve-level phase quantisation of this unit cell. The E-field distribution of this unit cell is very similar to that of SU-8 meta-atoms.

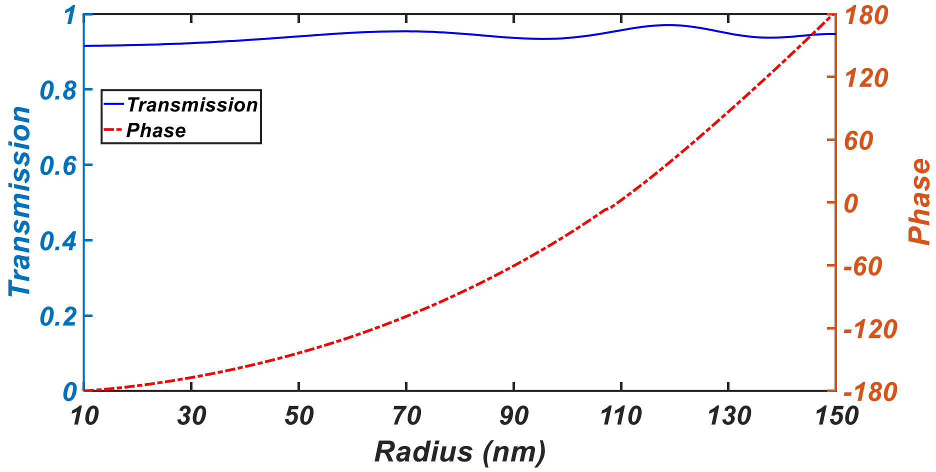

Fig. 2.18. Optical response of the PMMA meta-atom designed at 532 nm.

Table 2.9. **12-level phase quantisation for PMMA meta-atoms at 532 nm.**

Phase	-175°	-145°	-115°	-85°	-55°	-25°	5°	35°	65°	95°	125°	155°
Radius	21 nm	48 nm	67 nm	81 nm	92 nm	102 nm	110 nm	118 nm	125 nm	131 nm	138 nm	144 nm

2.2.4.3 Design of silicon meta-atoms

MSs made of silicon could gain an advantage in the context of mass-scale manufacturing simply due to the maturity of the current technology and existing facilities for manufacturing silicon chips. Hence, it would be useful to extend the air-hole design method to (crystalline) silicon, as illustrated in Fig. 2.19. For consistency, the meta-atoms are designed at λ = 532 nm, while they can be designed at other visible wavelengths.

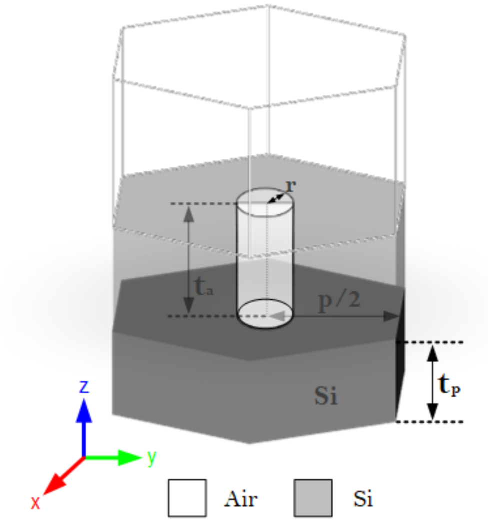

Fig. 2.19. Schematic view of the silicon meta-atoms.

To simulate this structure, the same boundary conditions as of the SU-8 case were applied. The designed parameters are reported in Table 2.10.

Table. 2.10. **Silicon meta-atom designed parameters at 532 nm for holographic applications.**

Parameter	**Value**
Operational wavelength	532 nm
Lattice constant (p)	190 nm
Radius scan (r)	20-95 nm
Air hole pillar height (t_a)	230 nm
Si substrate (t_p)	0.0 nm

Figure 2.20 depicts the optical response of this unit cell. As expected, the high refractive index of silicon results in a severe phase change with respect to the pillar radii, and a much thinner membrane compared to previous cases. However, the increased impedance mismatch between the structure and surrounding environment leads to a less favourable transmission response.

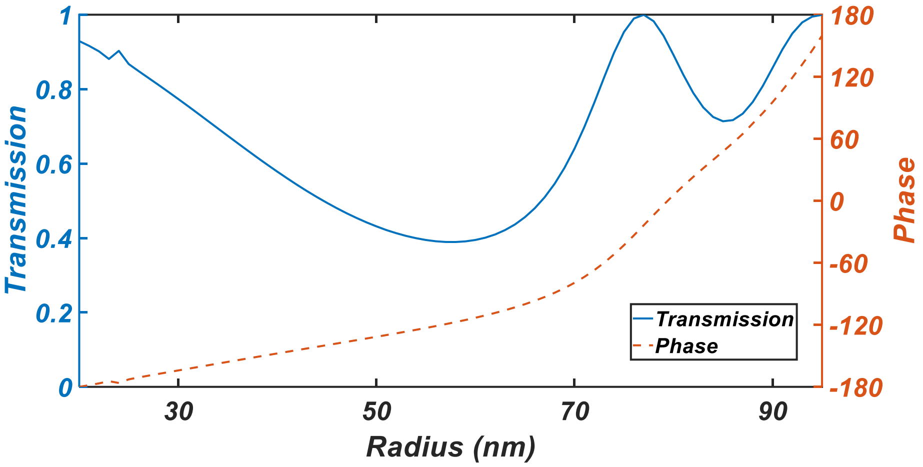

Fig. 2.20. Optical response of the silicon meta-atom designed at 532 nm.

In this design, the substrate thickness (t_p) was considered zero. Hence, given the proposed thickness of the membrane (230 nm), it is compatible with commercially available Silicon-On-Insulator (SOI) chips to facilitate its fabrication. It should be noted that silicon with this thickness can still be used as a flexible and conformable structure [153]. Hence, one can embed this MS membrane in a transparent flexible substrate such as SU-8 or PDMS for conformable applications. Table 2.11 reports on the twelve-level phase quantisation of this unit cell.

Table 2.11. **12-level phase quantisation for silicon meta-atoms at 532 nm.**

Phase	-175°	-145°	-115°	-85°	-55°	-25°	5°	35°	65°	95°	125°	155°
Radius	23 nm	41 nm	59 nm	69 nm	69 nm	73 nm	80 nm	84 nm	87 nm	90 nm	92 nm	94 nm

Figure 2.21 depicts the E-field distribution for this meta-atoms. The E-field distribution is more strong in the silicon part rather than the air pillar. It should be noted that the proposed structure in Fig. 2.19 can be designed to work in reflection depending on the target application. This, however, can be done by considering a thick crystalline silicon substrate under the meta-atoms structure and further optimising the design.

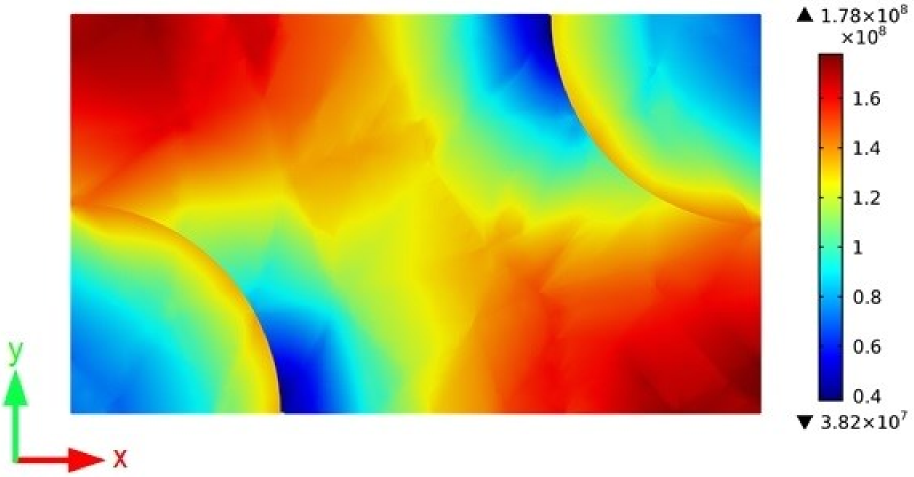

Fig. 2.21. E-field distribution of the silicon meta-atom (r = 50 nm) designed at λ = 532 nm for holographic applications.

2.3 Conclusion

I discussed the methodology for designing holographic MSs using the GSA algorithm. This algorithm is extensively used to design holograms throughout the following chapters. The design of novel meta-atoms using ZrO_2 in the visible range is comprehensively described. Furthermore, I presented a novel design consisting of air holes and further designed meta-atoms made of SU-8, PMMA, and silicon. In the next Chapter, I discuss the creation of these described meta-atoms.

2.4 Contribution

The hologram design formalisation of the GSA with RS was done by James Burch [136]. I used the combination of his code and mine to design the holograms. Then, I designed, analysed, and simulated all the ZrO_2 meta-atoms for different applications in the visible range. Importantly, I introduced and developed a new versatile method for the design of all-polymeric conformable holographic MSs in the visible range and ran all the simulations.

Chapter 3

Fabrication

This chapter presents the fabrication procedures of the novel MSs used in this thesis. Particularly, it addresses the fabrication methods to create rigid and flexible holographic MSs in the visible range. These techniques led to the creation of MS membranes with cm^2 sizes and thicknesses of hundreds of nanometres.

3.1 Fabrication procedures

This section provides general information about the fabrication procedures and conditions, including nanofabrication tools and materials to realise the required structures.

All fabrication was conducted in either of the two Class 10,000 cleanrooms, which refers to the number of particles larger than 0.5 µm per cubic foot. Processes that require high sensitivity, such as spin-coating, were carried out in a Class 1000 wet-deck. To put things into perspective, a standard room contains tens of millions of particles larger than 0.5 µm in the same volume. Additionally, the cleanrooms' temperature and humidity were tightly controlled to ensure greater consistency in the fabrication processes, such as spin-coating.

3.1.1 Materials

Various materials were exploited to realise the fabrication of MSs for this thesis, with the primary constraint being the chemical stability of these materials. This means that selected materials must withstand all subsequent steps in the fabrication process. For instance, if the material degrades or is entirely removed during subsequent developing or baking steps, it is considered to exhibit poor chemical stability. Consequently, a meticulous selection of materials is essential, tailored to the specific structures intended for fabrication. In the following, the materials used in this thesis are discussed.

Glass slides, as the most used substrate for this thesis, are cost-effective and optically transparent. This transparency makes it suitable for transmissive devices which were the main idea of this thesis. Importantly, glass slides exhibit chemical inertness, making them compatible with the entire fabrication process. Nevertheless, glass has a limited ability to dissipate charges during electron beam lithography (EBL) or SEM, often necessitating an additional conductive layer.

Silicon, due to its outstanding properties, was the second most used substrate in the fabrication process. Commercially produced silicon wafers are planar with minimal defects, crucial as subsequent materials layered onto them are influenced by any defects present in the initial substrate. Also, silicon's relative inertness offers compatibility with a broad spectrum of subsequent chemical processes. Furthermore, its crystalline structure facilitates easy cleaving, a vital step in membrane release for flexible structures. Lastly, silicon exhibits sufficient electrical conductivity to minimise charging effects during both EBL processes and SEM, eliminating the need for an additional conductive layer.

Zirconium dioxide, due to its availability and outstanding material properties described in Chapter two, has been selected and used as the core material of the most implemented meta-atoms in this thesis. Across the visible range, it offers a weakly-dispersive high refractive index with negligible loss. Its hardness and transparency combined with its biocompatibility make ZrO_2 an ideal material platform for real-life applications. Compared to TiO_2, ZrO_2 temperature resistance and its mechanical strength is advantageous. In addition, TiO_2 conformal deposition typically happens in high temperatures while that of ZrO_2 occurs at 80 °C. Recently, Hafnium dioxide (HfO_2) has been explored as an interesting alternative material [154]. Compared to HfO_2, ZrO_2 offers a higher refractive index in the visible range while it is cheaper. However, it should be mentioned the choice between these materials depends on various factors such as the specific requirements of the given application, the operating conditions, and the fabrication process.

I have explored and used a variety of polymers to ensure they are the ideal material for the intended fabrication procedure. The three polymers that I used the most and found ideal for the fabrication of this thesis are PMMA, SU-8, and Omnicoat. PMMA is a high-resolution positive tone resist, transparent, and affordable. This material was used mainly for EBL patterning. Nevertheless, PMMA is less chemically inert, as it dissolves in common solvents such as acetone and MF-319.

SU-8, a negative tone polymer resist manufactured by Microchem and available in various molecular weights, derives its name from the epoxy groups present in its monomers. Upon exposure to UV radiation or an electron beam (Ebeam), these epoxy groups undergo polymerisation, forming a highly stable compound with outstanding chemical stability. It is essential to mention that after exposure, SU-8 is chemically stable.

In this thesis, two different SU-8 resist types, SU-8 2050 and SU-8 2000.5, with varying molecular weights and viscosities, were employed. The viscosity of the resist determines, among other factors, the thickness of spun resist layers using a spin coater. The viscosity of SU-8 resists was further customised by blending different ratios of 2050 and 2000.5 with the solvent Cyclopentanone. Increasing Cyclopentanone content results in a thinner layer at the same spin speed, while a higher proportion of 2050 results in a thicker layer.

Omnicoat, a polymer available from Microchem, was initially formulated as an adhesion promotion layer for SU-8 to enhance the quality of spun SU-8 layers. However, in this thesis, Omnicoat served a different purpose as a sacrificial layer. The primary goal of this sacrificial layer was to facilitate the removal of SU-8 membranes from a rigid carrier as the last step of the fabrication for flexible structures. Omnicoat demonstrates chemical stability during the SU-8 development, including baking, exposure, and other required developing procedures. Nonetheless, it dissolves in two chemical solvents, MF319 and 1165, both available from Microchem. This enables the removal of Omnicoat from the structure, resulting in realising the membrane attached to it previously.

Gold was the metal material of choice for the work done in this thesis due to its compatibility with all fabrication processes. Its adhesion can be enhanced by applying a 3 nm layer of NiCr. It is physically soft, conductive, and chemically inert. This makes it exceptionally well-suited for Reactive Ion Etching (RIE). I have used gold mostly as a hard mask for the RIE step and to use its properties in SEM, to ensure the PMMA development.

3.1.2 Nanofabrication processes

In this section, I detailed the process of using the machines involved in fabricating my structures, rather than delving into the details of their working principles.

3.1.2.1 Electron Beam Lithography

EBL was employed to define patterns for all the samples presented in this thesis. This process utilises a highly focused electron beam to expose and create patterns in photoresist materials. These materials can be positive or negative tone resists that can be selected depending on the intended pattern. The bond structure within the resist undergoes alterations upon exposure to electrons or UV radiation. Subsequently, the loosely bonded areas can be eliminated through a developing step following exposure.

The utilized EBL system was a RAITH eLine Plus Nanofabrication. In this system, electrons accelerate from the tip at variable energies, reaching up to 30 keV. Numerous lenses facilitated beam collimation and adjustments to spot position, focal distance, aperture alignment, and stigmation. Different apertures control the current and spot size while further collimating the beam. For instance, larger apertures such as 30 μm lead to faster writing time for larger features. In contrast, smaller apertures such as 7 μm provide slower writing time but offer higher accuracy and they can more accurately define features in a few hundred nanometres scale. The spot position on the sample could be adjusted in three dimensions by altering the stage position.

To implement the designed pattern with EBL, the preparation of a position list prior to writing is required. This position list was the position of meta-atoms to realise the required phase shift for the target MS. All the position lists in this thesis were obtained through a customised MATLAB code written by myself, and then imported to the RAITH eline Plus software. It is essential to mention that for all the patterns made, proximity correction was applied to optimise the received dose by each meta-atom, to ensure all of them can fully develop at the same time. This requirement is due to the different sizes of the meta-atoms, so they need a different amount of exposed dose to be fully developed simultaneously with other meta-atoms. It should be noted that the final delivered dose to a feature/meta-atom consists of three doses including base dose, design dose, and dose factor. The base dose is the same for all the features. The design dose can be the same for all the features or it can be optimised, e.g. using a proximity correction procedure. The dose factor can be engineered for each structure separately. For instance, smaller features/meta-atoms required a larger dose in my fabrications.

Before each writing, the system was aligned. This was done initially using a scalpel blade to create a scratch at the corner of each sample, to align the focus, aperture, and stigmation. Further adjustments included focus optimization for the sharpest SEM image, wobbling the focus for aperture alignment, and finding a circular object for stigmation adjustment.

Then, after importing the position list to the software, an initial beam optimization involved burning a contamination spot into the resist, near the intended exposure area of the structures. Subsequent spots were burned to further optimize the beam.

It should be noted that in all the samples I have used a customised dose test including different features with different doses to examine the outcome after development. I used these features to make sure my target MS is fully developed.

3.1.2.2 Atomic Layer Deposition

ALD is a powerful thin-film deposition technique that offers precise control over film thickness and composition by growing layer-by-layer deposition. It is a controllable cyclic process in vapor-phase, to create thin films on various substrates with remarkable conformity and uniformity. The film thickness then can be controlled by the number of cycles in a sub-nanometric scale. Each cycle usually consists of two half-reactions which leads to the deposition of one atomic layer. Each reaction comes from a precursor, where the target material is stored.

The ALD used was a Cambridge Savannah ALD System with six precursors for different materials, and a circular-shaped chamber, large enough to introduce numerous samples with an average size of 5 × 5 cm^2. The chamber does have inner and outer rings with controllable temperature. It uses nitrogen as the carrier gas to carry the vaporised materials to the chamber. During the ALD procedure, the chamber was under vacuum. The processing time for each sample can be relatively slow due to the ALD cyclic nature but it depends on the material under deposition and the target thickness. Deposition of some materials requires higher temperatures. This high temperature under vacuum combined with the long processing time can introduce a challenge as the patterned features of the sample should withstand this situation until the target thickness is met. In my case, I used ALD to deposit ZrO_2 and for the target thickness, it took around five hours. This time under the aforementioned situation was enough to melt my patterned sample which was made of a polymer (this point will be addressed later in this chapter). However, this is a fair cost to deposit high precision thicknesses with conformable coating combined with uniformity across large areas.

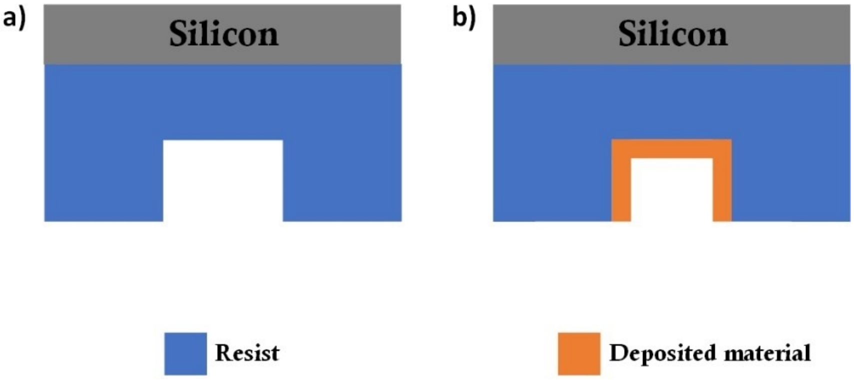

Fig. 3.1. Schematically showing the conformal deposition using ALD technique. The deposition growth from side walls and is not directional.

In this thesis, using ALD was inevitable as I was required to deposit my material in high-aspect-ratio structures in which ALD could provide this deposition with uniformity. However, this goal was not achievable with other deposition methods like Ebeam evaporation. This is simply because controlling the deposited film's uniformity for high aspect ratio features was challenging. One of the main features of ALD rather than other deposition methods is shown in Fig. 3.1. This figure illustrates the deposited material in the ALD technique grows from the walls, and is not directional. This makes it a well-suited method for the deposition of high-aspect-ratio features.

3.1.2.3 Electron Beam Evaporation

The evaporation processes described in this thesis were conducted using an Edwards AUTO 306 Electron Beam evaporator. This evaporator mainly consists of a chamber, a sample holder on top of the chamber, a shutter, rotational crucibles systems allowing different crucibles with different materials, and an electron gun which directs the beam onto the underside of a selected tungsten crucible.

By turning the beam on, the energy emitted by the electrons through the gun transfers to the crucible, heating the metal contained inside it. At sufficiently high beam intensity, the metal undergoes evaporation in a directed manner towards the sample, located at the top of the chamber. A quartz crystal was used to monitor the deposition rate, calculate the tooling factor, and eventually measure the final deposited thickness. It should be noted that the tooling factor can vary depending on the deposition rate. All evaporation procedures were carried out in a high vacuum environment ($\approx 10^{-5}$ Pa) to minimise collisions between metal and air molecules.

The shutter was used to block the material from reaching the sample at both the start of the evaporation and the end of the evaporation. This was important when the evaporation started because the deposition rate was not yet fixed, and it could be excessively high, resulting in a risk of damage to the sample by imparting too much heat. On the other hand, the deposition rate could be too low, potentially compromising the formation of high-quality films. Therefore, the shutter provides material deposition onto the sample only when the evaporation rate falls within the fixed target range.

Furthermore, the evaporator incorporates sample rotation around the centre to enhance uniformity by eliminating angular dependence. This tool was specifically used when a uniform layer was needed. However, for deposition onto the patterned sample, e.g. to deposit some metal into a developed sample to examine their development, this rotation was avoided. This was due to the creation of some deposited unfavourable features around the patterned features, making it challenging to examine the sample.

3.1.2.4 Reactive Ion Etching

In this thesis, a customized RIE machine was employed to transfer the required patterns in the desired material. Usually, a layer of 40 nm gold, as the mask was used for this purpose. Argon was selected for the RIE steps due to its substantial mass, effectively milling the gold. In this process, a direct current (DC) bias propels heavy argon ions at high velocities into the sample, resulting in a uniform physical milling of the material. The pivotal factor in the RIE procedure is the DC bias, determining the kinetic energy transferred during argon-sample collisions. Additionally, argon etching is a straightforward physical process, obviating the need for chemical etchant gases in the case of thin gold layers. Materials with different thicknesses may necessitate a more intricate etching process to ensure parallel sidewalls.

To operate the RIE procedure, the sample was initially loaded in a high vacuum chamber, which was then evacuated to approximately 10^{-6} Pa to eliminate impurities that could impact etching properties. Argon is introduced into the chamber at a controlled rate using a mass flow controller to achieve a predetermined pressure. A radio frequency (RF) signal ionises the gas at 13.56 MHz, and the heavy ions remain relatively stationary. The electrons, however, are accelerated to the top plate and the walls where they are connected to the ground. This procedure creates a static DC field within the chamber and generates a plasma.

Also, I have used the mixture of oxygen (O_2) and Sulfur hexafluoride (SF_6) to etch polymers like SU-8 and PMMA. A similar process except for the employed gasses was used for these processes. The pre-set power of the RF signal combined with the etching pressure are important elements in determining the etching rate. Hence, the etching time is dependent on the etching rate and the target thickness. For a 40 nm gold layer, the typical etching time was 8 minutes, while for a 1 μm SU-8 layer, it was 6 minutes, resulting in an approximate etching rate of 5 nm minute^{-1} for gold, and 166 nm minute^{-1} for SU-8, respectively. It should be noted for all the etching processes performed for this thesis, I waited 10 minutes to ensure the introduced gasses into the RIE chamber were evenly spread, leading to an even etching process.

3.2 ZrO_2 metasurfaces for visible light holography and optical trapping

To fabricate ZrO_2 MSs operating in the visible range, the workflow illustrated in Fig. 3.2 and described in detail later in this section was followed. These procedures were the same for MSs functioning for the holography and optical trapping applications and took around four days per sample.

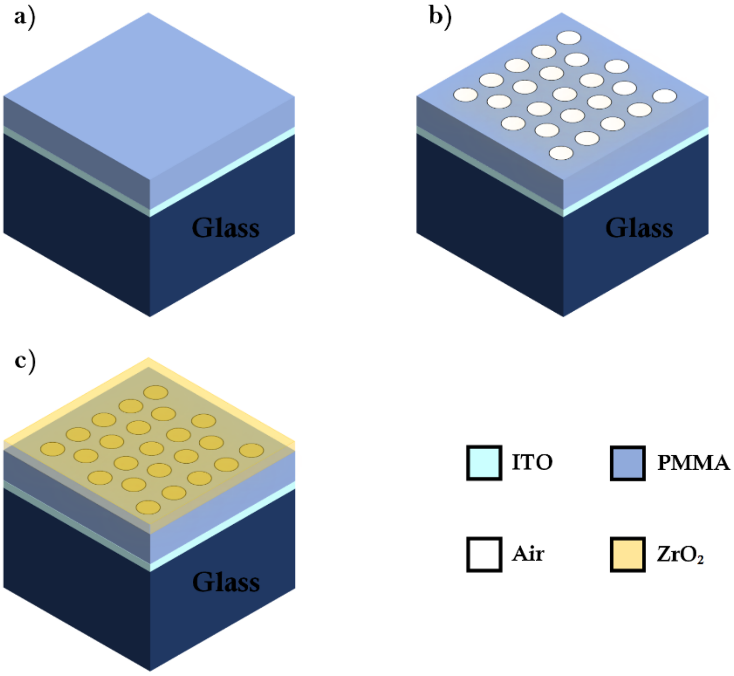

Fig. 3.2. Schematic of the fabrication process for the ZrO_2 MSs. (a) A glass substrate was initially coated with a thin ITO layer by evaporation and a thick PMMA film by spin-coating. (b) PMMA layer was patterned through the standard EBL process. Nanopillars were defined after the development process. (c) ZrO_2 nanopillars with a flat surface atop were obtained after the ALD process.

However, achieving a working recipe to fabricate these structures was challenging and it happened after examining a lot of sacrificial samples. The challenges followed by their solutions are presented in the following.

3.2.1 Challenges and solutions

The fabrication scheme of these ZrO_2 MSs is presented in Fig. 3.2. However, in the interest of simplification and clarification, I address Fig. 3.3 which can clearly show the required process. Hence, I discuss the challenges considering this nanofabrication process.

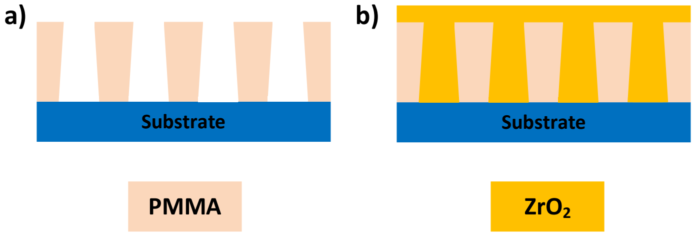

Fig. 3.3. Schematic of the fabrication procedure for ZrO_2 MSs. (a) EBL and development, and (b) ALD procedure to fulfil the nanofeatures with ZrO_2.

I started to make the designed MS patterns using silicon rather than glass substrate as it is a semiconductor and compatible with the EBL procedure. This step was required to make sure the developing recipe works for the most suitable situation. Then, it was easier to make them on glass.

The MS features consisted of high-aspect-ratio pillars, and the electron backscattering phenomenon was not an issue with silicon. Figure 3.4 shows microscope and SEM images of the created pattern on a silicon substrate with 350 nm PMMA coated on top. For simplicity, I started with a square lattice constant and considered all the pillars to have identical radii as clearly shown in Fig. 3.4(c). After reaching the stage shown in Fig. 3.4(f), where I could create nanopillars with fully developed features for one fixed pillar radii, the next crucial step was to develop a fabrication recipe to create fully developed nanopillars with various radii and an increased thickness in the PMMA layer. The minimum and maximum pillar diameter sizes were 30 nm and 374 nm, respectively. Creating these nanopillars with different geometrical sizes combined with an increased layer of PMMA up to 700 nm, imposed a considerable challenge in their nanofabrication process.

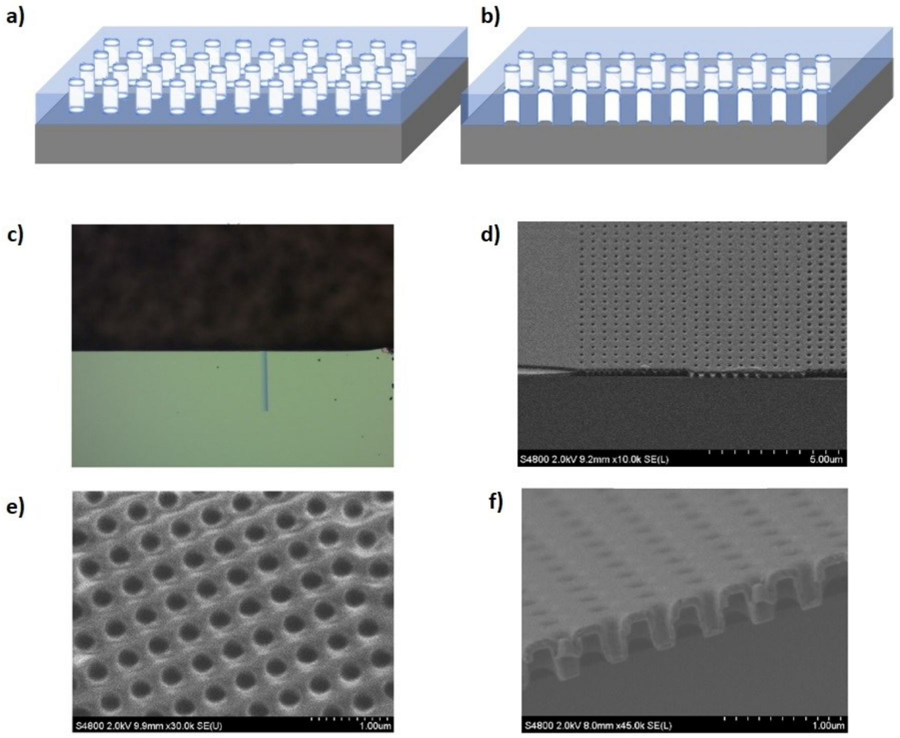

Fig. 3.4. (a) Schematic showing a sacrificial sample to create nanopillars on a silicon substrate with 350 nm coated PMMA on top. (b) Schematic showing the cleaved sample from its edge. (c) shows the cleaved sample to inspect the nanopillars with SEM. The blue line indicates the feature areas. (d) SEM image of the cleaved sample, looking from its cleaved edge while the sample is tilted. (e) SEM image of the nanopillars from the top. (f) SEM image of the cleaved sample with higher magnification. This clearly shows the pillars were fully developed.

The nature of this challenge comes from the fact that all the nanopillars must develop simultaneously together. Hence, the delivered EBL exposure dose of each of them should not be identical. Generally, smaller pillars require a higher EBL exposure dose while the larger pillars require a smaller EBL exposure dose.

Figure 3.5 illustrates SEM images of some attempts with sacrificial samples. These samples were made of a silicon substrate with 700 nm coated PMMA on top. I created many of these sacrificial samples to optimise two important factors: (i) delivered EBL exposure dose to pillars with different radii, and (ii) development time. To shine a light on this matter, Fig. 3.5(a-d) illustrates SEM images of developed samples, while it is clear that some of the nanopillars are either merged or completely washed away. These images indicate the cycle of exposure and development was ineffective. One might consider that because some of the pillars were merged, the nanopillars were fully open and they had reached the bottom of the substrate (silicon). This can be inspected by depositing a layer of metal on the sample, in particular, on PMMA and then removing it. The nanopillar pattern should be retained if they were fully opened. Figure 3.5(e) presents the SEM images of the sample after the evaporation of 5 nm NiCr for adhesion purposes followed by 30 nm of gold. Figure 3.5(f) shows the SEM image of the sample after the removal of PMMA. It is clear that a considerable number of nanopillars were not fully opened and did not reach the silicon substrate.

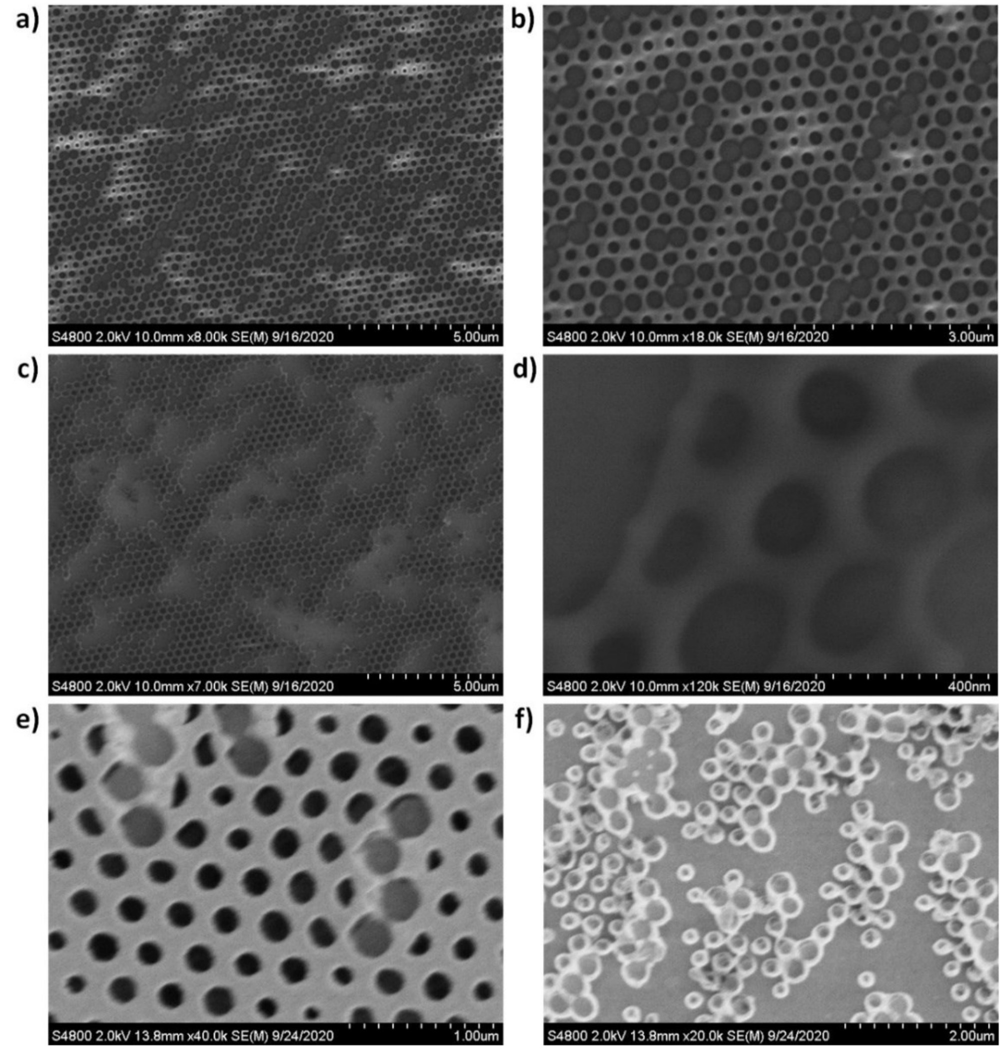

Fig. 3.5. SEM images of sacrificial samples with silicon substrate and 700 nm PMMA coated on top. (a-d) SEM images of different developed samples with different delivered EBL exposure doses and development times. (e) SEM image of a developed sample with 35 nm deposited metal on top of it. (f) SEM image of a sample after removal of PMMA.

Figure. 3.6 illustrates an SEM image of a developed sample obtained after carefully cleaving it to see the nanopillars from their cleaved edge.

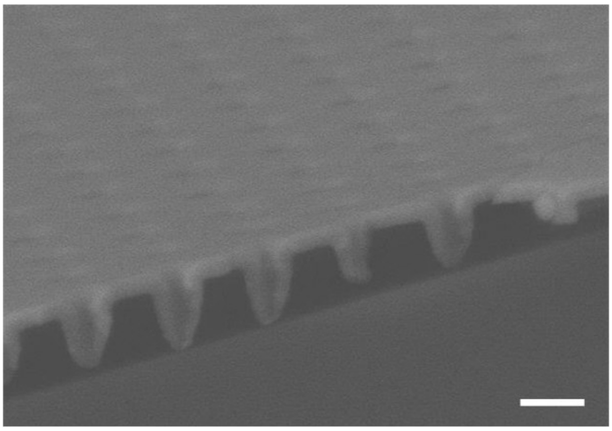

Fig. 3.6. SEM images of a sacrificial sample to inspect the created nanopillars. The scale bar is 500 nm. The image shows that even though the features are open from the top, they are not fully opened with straight walls to the bottom of the substrate.

Addressing this issue posed a significant challenge. It involved determining the precise parameters for exposure and development. After an extensive effort to optimise the proximity correction, required doses, development time, and other involved parameters to ensure complete pattern development, I should have transferred this approach to the glass substrate to realise transmissive structures.

During this transition, the first issue I faced was the electron backscattering as glass is a dielectric material and the electron charging during the EBL writing would have destroyed the resolution and the geometry of the target features. Especially, the side walls of the features shown in Fig. 3.3(a) were not developed as straight walls and adjacent pillars occasionally merged. To address this problem, I decided to coat a thin conductive layer onto the glass before spun coating the photoresist. This helped to overcome this issue.

The second major issue I was dealing with was the developing stage in which not all the meta-atoms with different sizes were developed at the same time. The larger meta-atoms were overdeveloped and merged with the adjacent features and the smaller meta-atoms were underdeveloped, not reaching the glass substrate. Though optimising the proximity correction to optimise the given exposure dose to each pillar can help, this was not enough to solve the issue. The final solution, after many tests, was reached by optimising the ratio of deionised (DI) water to IPA which is addressed further in this Chapter.

To illustrate the importance of having straight-developed walls (see Fig. 3.3(a)), Fig. 3.7 shows an example of a failed sample due to incomplete development and not having straight walls for larger nanopillars. After ZrO_2 deposition, as schematically shown in Fig. 3.3(b), the centre part of the nanopillar is not filled with ZrO_2 which significantly affects its performance. This challenge was overcome by optimising the parameters for the fabrication.

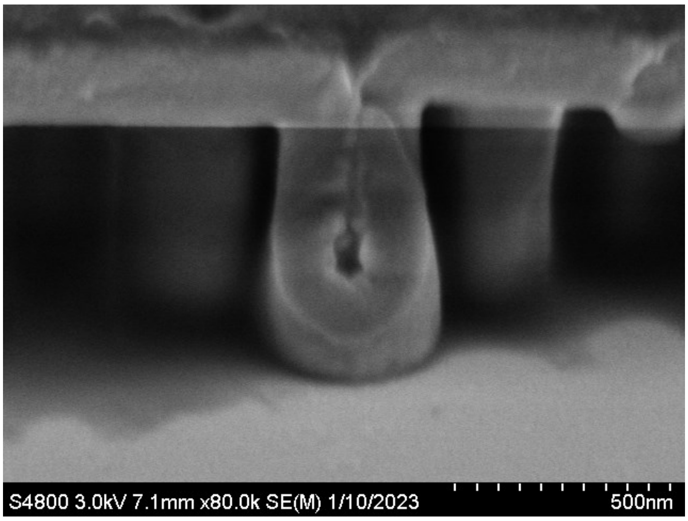

Fig. 3.7. SEM image of a nanopillar.

To validate the solution and ensure all the nanopillars with different sizes were fully developed, a gold deposition of 40 nm was done on a developed sacrificial sample. Then, the PMMA was lifted off to see the results. Figure 3.8(a) shows an SEM image of a part of this sacrificial sample after EBL and development. Figure 3.8(b) illustrates an SEM image of the lifted-off sample. This procedure was followed and repeated a couple of times to ensure the samples were fully developed in different fabrication runs.

After this stage, where I had fully developed patterns, the next step was to fill the nanopillars with conformal deposition of ZrO_2 using the ALD technique.

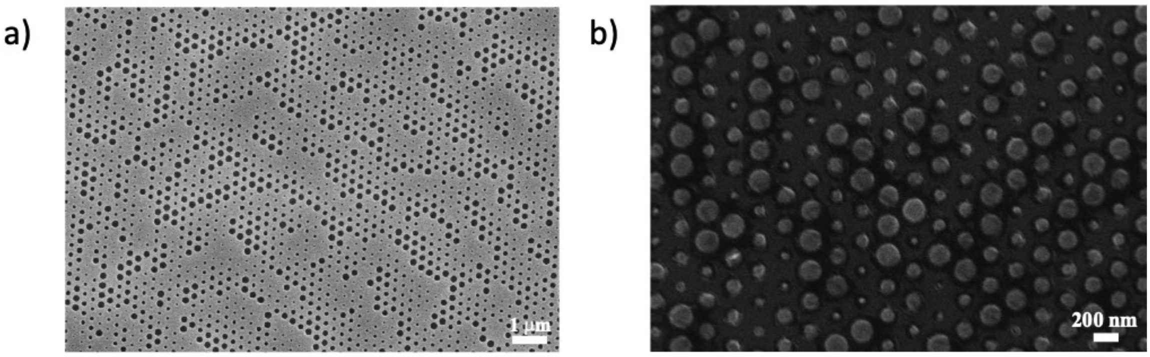

Fig. 3.8. Sacrificial sample to ensure development. (a) SEM image of the sample after the EBL and developed procedure. (b) SEM image of the lifted-off sample.

The sample should stay and survive in the ALD chamber for approximately five hours to gain the required deposition thickness. This was a problem because the patterned PMMA was melting inside the ALD chamber, so the obtained sample after the ALD procedure was not the structure that was initially designed. The solution to this issue was to post-bake the sample again on a hotplate with the reported temperature and time following this Chapter and to decrease the ZrO_2 deposition temperature to 80 °C. At this stage, I developed a working recipe to successfully fabricate ZrO_2 MSs.

Figure 3.9 (a-b) shows some microscope images of the developed samples with different side lengths which were fabricated for optical trapping purposes. Figure 3.9(c) illustrates the sample after the ALD procedure. Figure. 3.9(d-f) depicts some SEM images of the cleaved samples to inspect the fabricated nanopillars.

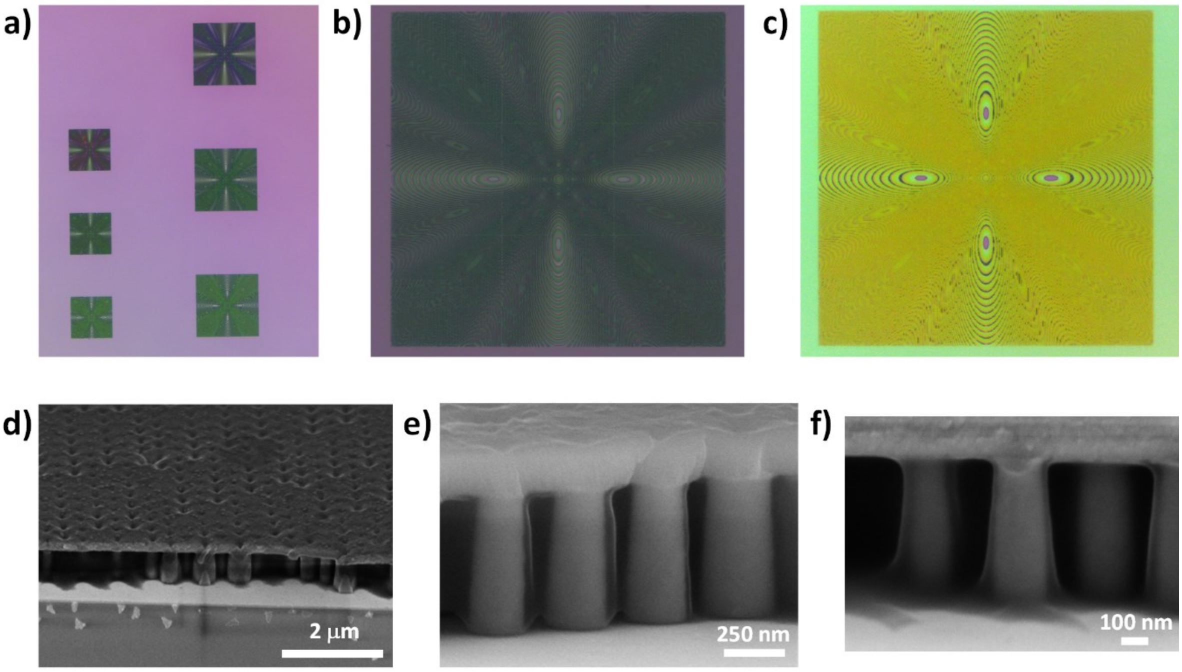

Fig. 3.9. Microscope (a-c) and SEM (d-f) images of fabricated samples.

3.2.2 Fabrication procedure for ZrO_2 metasurfaces

1. Cleaned the microscope glass by submerging it in acetone and then isopropyl alcohol (IPA) under sonication. Each cleaning step was carried out at room temperature for 5 minutes. Deposited 50 nm of ITO onto the glass substrate to act as a thin conductive layer. The typical deposition parameters are shown in Table 3.1.

Table. 3.1. **Typical deposition parameters.**

Parameters	**Value**
Base Pressure	1e-6 mPa
Deposition Pressure	1e-5 mPa
Deposition rate	0.3 nm min^{-1}

2. Spin-coated a thick layer of PMMA as the photoresist to define the pattern, at 1250 rpm for 1 minute. The thickness of this layer was 700 nm. This thickness is dictated by the design.
3. Baked for 5 minutes at 180 °C.

4. EBL step using a RAITH eLine Plus with the parameters recorded in Table 3.2.

Table. 3.2. **Typical electron bean parameters for defining nanopillars.**

Parameters	**Value**
Extra High Tension (ETH)	30 kV
Base dose	150 μC cm^{-2}
Dose factor	0.65
Working distance	9.7 mm
Write field size	100 × 100 μm^2
Aperture size	10 μm
Basic step size	6 nm
Area step size	20 nm

5. Developed the PMMA resist with DI water and IPA solvent with a ratio of 1:1, for 1 minute at room temperature.
6. Post-baked the sample for 20 minutes at 95 °C. This step was necessary to increase the rigidity of the PMMA membrane to prevent the melting of the pattern into the ALD chamber. The baking temperature was chosen to be below the glass transition temperature.
7. Deposited 180 nm ZrO_2 onto the sample by inserting the sample into the ALD chamber. To create ZrO_2 using ALD, H_2O and TDMAZr precursors with the parameters recorded in Table 3.3 were used. These parameters gave the average deposition rate of 1.78 Å per cycle.

Table. 3.3. **parameters used for atomic layer deposition of ZrO_2.**

Parameters	**Value**
Inner ring temperature	80 °C
Outer ring temperature	80 °C
Valve manifold temperature	120 °C
Exhaust line temperature	120 °C
Trap temperature	120 °C
TDMAZr precursor temperature	75 °C
Chamber pressure during deposition	0.270 Torr
H_2O pulse time	0.3 s
Waiting time	7 s
TDMAZr pulse time	0.03 s

Figure 3.10 shows the finished ZrO_2 MSs with the microscope glass substrate, mounted on a 30 mm cage for experimental purposes. In addition, Fig. 3.11 displays an SEM image of the finished fabricated sample, where it was cleaved, and the image was taken from the cleaved edge of the sample.

Fig. 3.10. An image showing the MSs on a roughly 7.5 × 7.5 cm^2 glass microscope mounted on a 2D stage for an experiment.

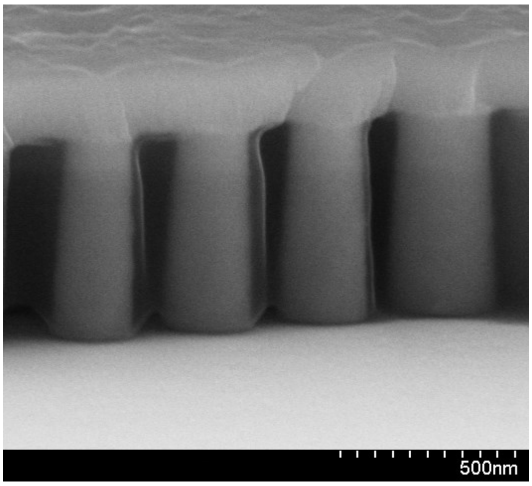

Fig. 3.11. An SEM image of a cleaved ZrO_2 MS, looking at the edge of the cleaved part.

3.3 Polymeric membrane metasurfaces

In this section, I introduce a new type of meta-atoms operating at the visible range, consisting of an airhole inside a polymeric material. All-polymeric membrane MSs operating in the visible range can be made using two popular photoresists, PMMA and

SU-8. The choice of material depends on the application and fabrication procedure, e.g. a negative or positive photoresist should be patterned. Also, The PMMA refractive index in the visible range is slightly lower than that of SU-8.

Here, I present the fabrication of All-polymeric SU-8 membrane MSs. To fabricate SU-8 MSs, the workflow depicted in Fig. 3.12 and described in detail below was followed. These procedures took around four days per sample.

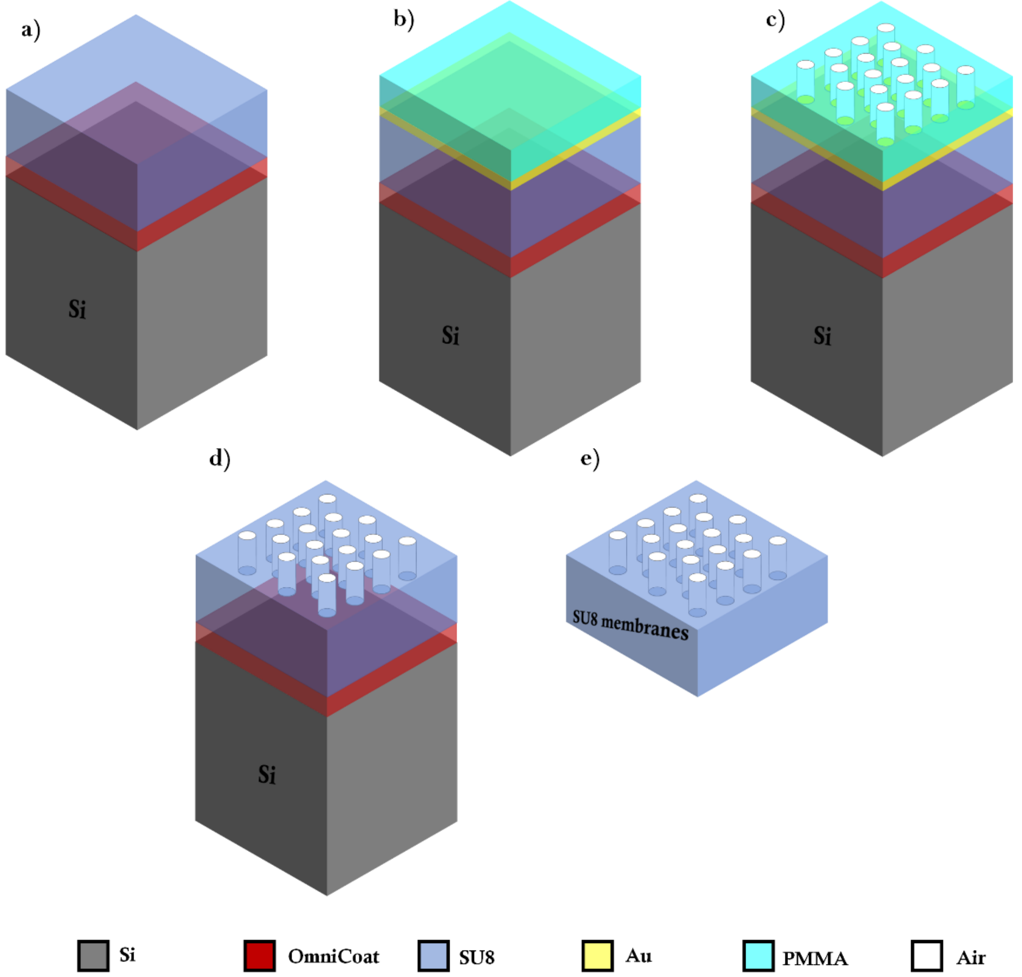

Fig. 3.12. Schematic of the fabrication process for the SU-8 MSs membranes. (a) A standard silicon carrier was initially coated with a thin Omnicoat as a sacrificial layer and then a thick SU-8 layer by spin-coating. (b) Then, the sample was coated with a thin layer of gold via evaporation. After that, a thin PMMA layer was spun coated onto the gold layer. (c) PMMA layer was patterned through the standard EBL process. Air nanopillars were defined after the development process. (d) Air nanopillars inside the SU-8 layer appeared after two RIE steps to etch the gold inside the nanopillars and then to etch the SU-8 layer, respectively. The leftover gold atop SU-8 was removed with a wet-etching process. (d) Flexible SU-8 MS membrane was obtained through a lift-off process.

3.3.1 Fabrication procedure for SU-8 metasurfaces

1. Cleaned the silicon carrier by submerging it in acetone and then isopropyl alcohol under sonication. Each cleaning step was carried out at room temperature for 5 minutes.
2. Spin-coated a sacrificial layer of Omnicoat (Microchem) at 1000 rpm for 45 seconds. The thickness of this layer was 100 ± 15 nm.
3. Baked for 1 minute at 230 °C.
4. Spin-coated a thick layer of SU-8 (Microchem) to act as a flexible membrane, this was a blend of SU-8 2050 and SU-8 2000.5 mixed 1:1, at 1000 rpm for 1 minute. The thickness of this layer was 6 ± 0.1 μm. This thickness was chosen to guarantee both the high flexibility and robustness of the MS membrane.
5. Baked for 5 minutes at 65 ◦C, then 5 minutes at 90 °C.
6. UV-exposed the SU-8 layer, to cross-link it, for 5 minutes.
7. Baked, to finalise cross-linking in the SU-8, for 5 minutes at 65 °C, and another 5 minutes at 90 °C.
8. Hard-baked, for 20 minutes at 170 °C
9. Evaporated 40 nm of gold onto the SU-8 to act as a hard mask. This layer was thick enough to protect the SU-8 underneath.
10. Spin-coated a thin layer of PMMA A2 950 K at 1000 rpm for 1 minute. The thickness of this layer was 200 ± 30 nm.
11. Baked for 5 minutes at 180 °C.
12. EBL step using RAITH eLine Plus with the parameters in Table 3.4.

Table. 3.4. **Typical electron bean parameters for defining nanopillars.**

Parameters	Value
ETH	30 kV
Base dose	150 μC cm^{-2}
Dose factor	0.75
Working distance	10 mm
Write field size	100 × 100 μm^2
Aperture size	10 μm
Basic step size	10 nm
Area step size	20 nm

13. Developed the PMMA resist with DI water and IPA solvent with respectively a ratio of 3:7, for 1 minute at room temperature.
14. Dry RIE step to remove the gold at the end of the nanopillars to make it ready for transferring the pattern from PMMA to the SU-8 layer. This step was carried out with Argon gas for 9 minutes, with the parameters reported in Table 3.5.

Table. 3.5. **RIE parameters to remove 30 nm gold.**

Parameters	**Value**
Base pressure	1e-6 mPa
Etching pressure	3e-2 mPa
Argon flow rate	500 sccm
RF Power	20 W
DC Bias	-300 V

15. Dry RIE step to etch the SU-8 layer at the end of the nanopillars to transfer the pattern to the SU-8 layer. The gold atop the unpatterned SU-8 layer protects the SU-8 underneath. This step was carried out for 6 minutes with a mixture of SF_6 and O_2 gases, with a ratio of 1:5, respectively. This etching with the parameters reported in Table 3.6 guarantees the removal of 1 μm SU-8, which was dictated by the design.

Table. 3.6. **RIE parameters to etch 1 μm of SU-8.**

Parameters	**Value**
Base pressure	1e-6 mPa
Etching pressure	2e-2 mPa
SF_6 flow rate	20 sccm
O_2 flow rate	100 sccm
RF Power	20 W
DC Bias	-252 V

16. Cleaved 4 edges of the sample to allow the lift-off solvent to dissolve all parts of the sacrificial layer.
17. Dissolved the Omnicoat layer, to release the membrane from the silicon carrier, using MF319 (Microposit). Then, the sample was transferred to DI water for rinsing and transferring the membrane to the desired carrier.

Figure. 3. 13 illustrates an image of the finished flexible SU-8 MS membrane, taken with a standard camera.

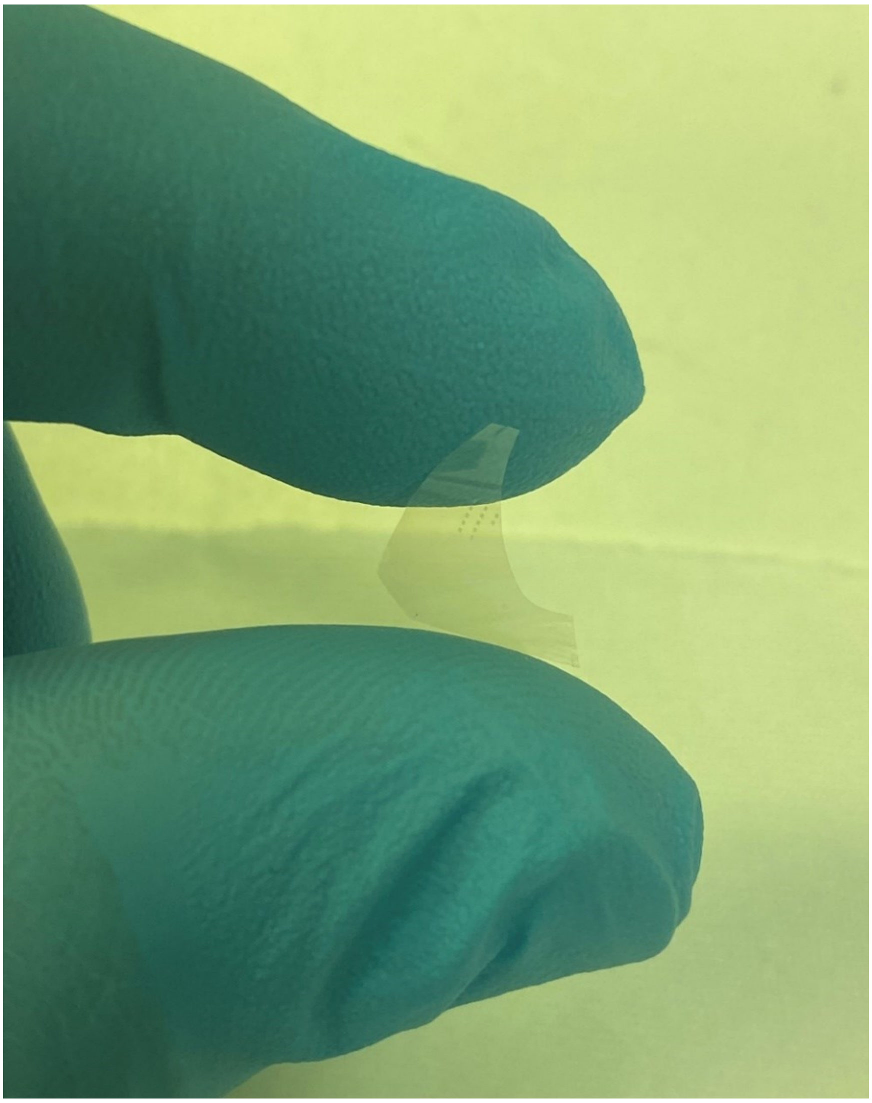

Fig. 3.13. An image showing the SU-8 MS membrane. The square-shaped structures are MSs with $200 \times 200\ \mu m^2$ size.

3.4 Conclusion

This chapter details the fabrication procedures for holographic MSs operating in the visible range used in this thesis. In particular, it reveals the fabrication of two different meta-atoms, ZrO_2 and SU-8 MS platforms. The challenges combined with their proper solutions are discussed. Furthermore, the presented methods could be incrementally improved, or the materials could be easily swapped if required. Specifically, for the flexible MS membrane platform made by SU-8, the main rate-limiting step for large-scale production was the EBL time. In theory, the nanoimprinting method with roll-to-roll printing could overcome this issue.

Generally, implementing automation could simplify the techniques used in this thesis for mass-scale production. The yields were already approaching 100%. In the next Chapter, I describe the experimental setups made to characterise the fabricated MSs. In particular, I use the setups to characterise MSs created by air-hole meta-atoms in Chapter 5, and pillar with top meta-atoms in Chapters 6 and 7.

3.5 Contribution

I carried out all the fabrication steps for all samples from similar processes utilised in the Synthetic Optics research group. I customised the existing recipes for fabrication procedures in this research group to satisfy my needs. In particular, I was extensively exposed to Nanofabrication tools, including Spin coater, hot plate, EBL eLine Plus, Ebeam evaporator, Sputerrer, Atomic layer disposition, RIE, Ellipsometry, Dek-talk profiler, and EVG system. In addition, I worked with a variety of photoresists and materials to develop a working recipe for the fabrication of two different platforms presented. In general, I made approximately eighty ZrO_2 MS samples, and eight SU-8 samples.

Chapter 4

Characterisation

This chapter outlines the experimental setups used in this thesis. In particular, it addresses the optical setups utilised to characterise the operation of holographic MSs in the visible range, for holographic imaging and optical trapping applications.

4.1 Experimental setup to characterise the efficiency of the metasurfaces

This section presents the experimental setups that were developed to measure the performance of the different types of MSs presented in Chapter 2. Also, the method of measuring the efficiency is described in detail.

4.1.1 Characterisation of the ZrO_2 and SU-8 metasurfaces

The efficiency of the holographic MSs is dependent on the target holographic image as different meta-atoms interact with the incident light and deflect the light in different directions to create the target holographic image. Hence, it is best to design a hologram to focus light into a point to enable the consistent measurement of the efficiency. Therefore, to quantitatively appraise the efficiency of these transmissive MSs, their ability to focus the light in a dot-shaped hologram using a customised setup is measured. The MSs were excited using a broadband supercontinuum laser (SuperK, NKT Photonics) in the visible range, mainly from 488 nm to 700 nm in increments of 50 nm. SuperK lasers use non-linear optical effects such as supercontinuum generation in photonic crystal fibres to generate a broad spectrum of wavelengths. Then the light is carefully guided and interacts with the fibre structure. Eventually, this interaction causes the light to spread out and break up into many different colours. Here, Fig. 4.1 shows the setup with the bandwidth of the beam $\approx$ 10 nm.

The laser beam was passed through a linear polariser and then expanded to a beam with a diameter of 1.5 cm with a telescope made of two lenses with focal lengths of 50 mm and 400 mm. After that, the beam was focused on the MS sample with a lens with a focal length of 1000 mm. This leads to a small beam with a narrow angular distribution and

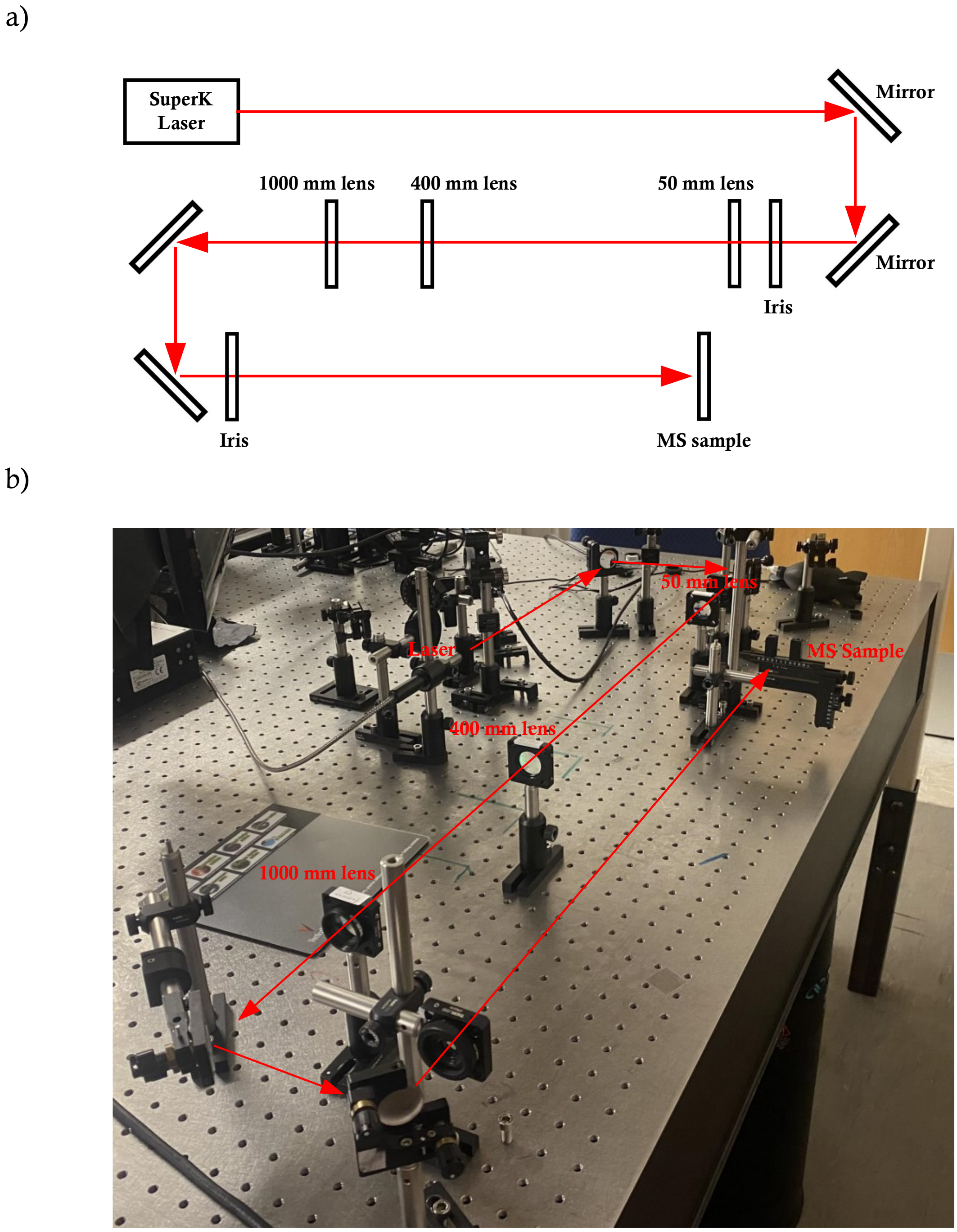

Fig. 4.1. The experimental setup to measure the efficiency of transmissive MSs. (a) schematic view, and (b) image of the experimental setup.

gives a good approximation of the normal incident. The setup produced a spot size of ~250 µm in diameter at the plane of the sample at the designed wavelength. Notably, the size of the MSs for characterisation was 200 × 200 µm^2. Thus, the focused laser beam obtained by this setup efficiently overfilled the square MS sample. Given this, the ratio of the power onto the MS sample was scaled to determine the incident power to the sample. The beam size as a function of wavelength was measured using a Thorlabs BC106N-VIS/M CCD beam profiler to measure the accurate beam size in each wavelength used.

The efficiency of the MSs was then obtained by a designed hologram that produced a dot-shaped image at 30 degrees with respect to the MS normal, at the designed wavelength. Figure 4.2, schematically shows this concept. It should be noted that the MS structure deflected the light at 30 degrees for the designed wavelengths. However, the efficiency measurements were done across the visible range and the detector position moved when measuring in different wavelengths due to the dependence of the diffraction angle on the incident wavelength.

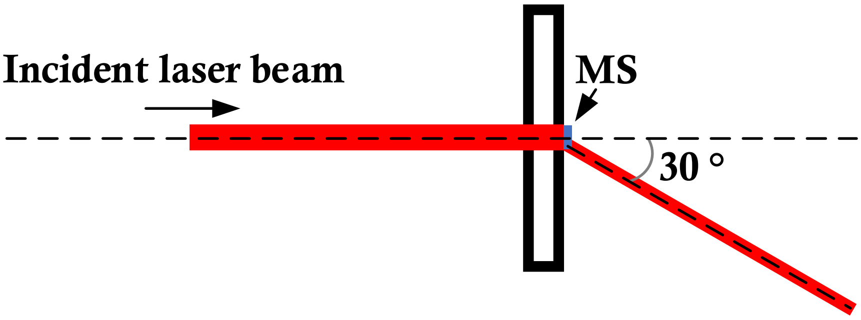

Fig. 4.2. Illustration of a MS design for efficiency measurements.

The diffraction efficiency was then obtained by normalising the power in the two first diffracted orders, normalised to the power of the (not diffracted) zeroth order. The power measurements were done using a Thorlabs S130C Photodiode Power Sensor. Figure. 4.3 intuitively shows a typical image of the focused spot created by the MS designed at λ = 488 nm.

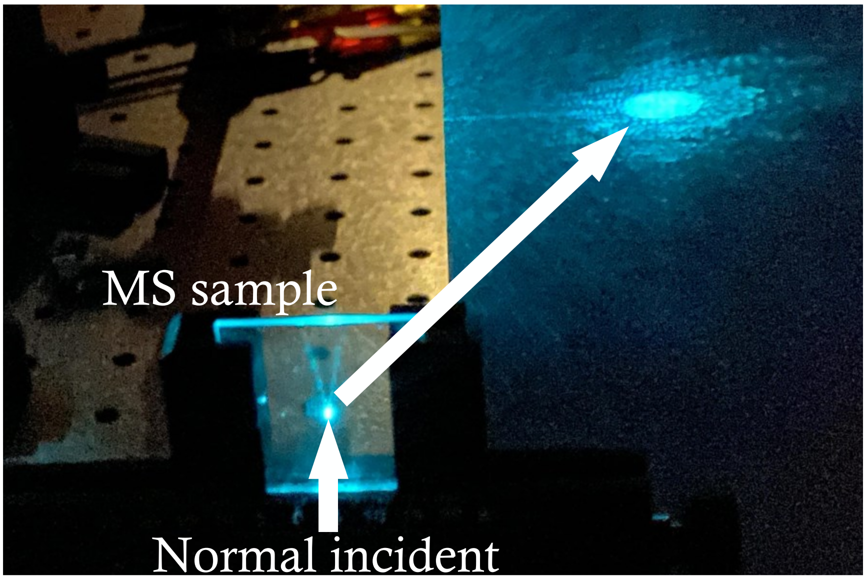

Fig. 4.3. The focused spot at 30° using the MS designed at λ = 488 nm.

Figure 4.4 illustrates the collection of images taken by this MS performing across the visible range at different wavelengths. It should be noted that these images were taken by placing a white screen instead of the power meter to show the performance of these MSs. Hence, their value is qualitative and not quantitative. The camera and exposure conditions were almost identical for all images.

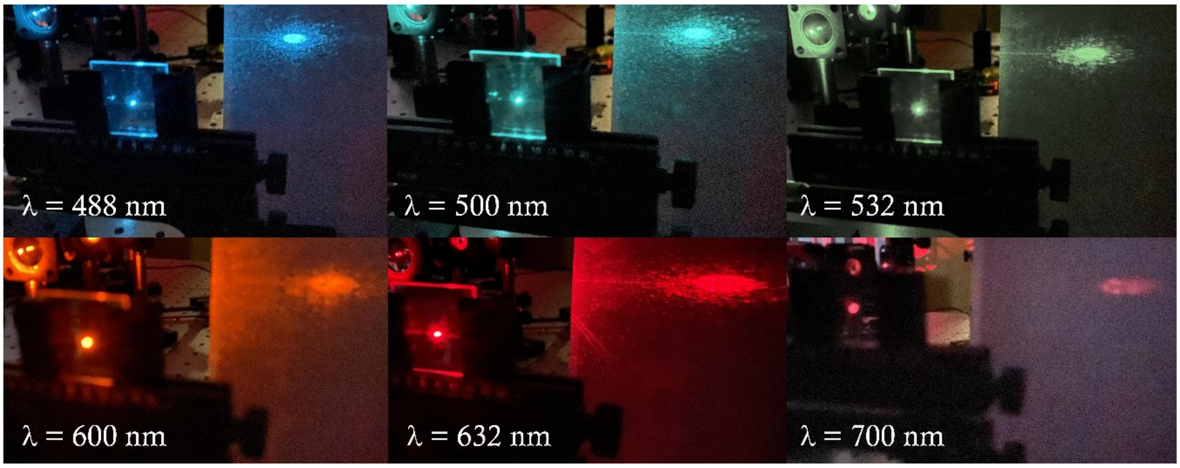

Fig. 4.4. The performance of the ZrO_2 MS to create a focused spot across the visible range.

4.2 Experimental setup for optical trapping applications of metasurfaces in microfluidic environments

The MS samples were prepared via a 100-micron-thick plastic strip and then sealed with a 150-micron-thick glass coverslip, where DI water and the particles of interest were placed in the space between the MS and the glass coverslip, as depicted in Fig. 4. 5. Notably, the MS structure was in the centre of this black plastic strip.

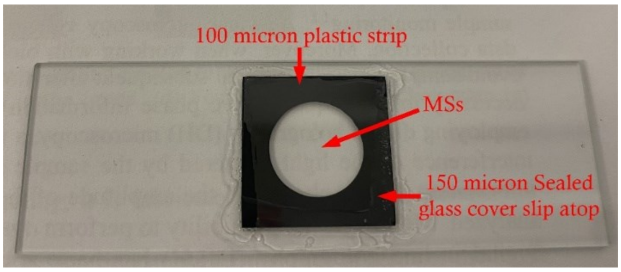

Fig. 4. 5. Sample preparation for operating in microfluidic environments.

Then, the experiment was done with the setup sketched in Fig. 4.6. It consists of two lasers with designed optics and a 4f system to access the microscope objective lens from top and bottom.

A gem-solid state continuous wave laser at 532 nm was linearly polarised and expanded to a beam with a diameter of 1.3 cm with a telescope made by two lenses with focal lengths of 100 mm and 1000 mm. The selection of lenses was made to magnify the input beam large enough to cover the circular aperture of the next optics. Then, to access the microscope objective from the bottom, the beam was redirected using a movable mirror and the beam was collimated again using a 4f system, made of two lenses with focal lengths of 750 mm. It should be noted that the use of a 4f system was necessary to control the collimation and size/magnification of the delivered beam to the back of the high NA objective lens, given the long optical path between the laser and the microscope. In addition, it simplified the alignment and stability of the system as the optical axis of the input and output beams remained aligned. The beam then reached the back of the objective lens using a long pass filter that reflected 532 nm.

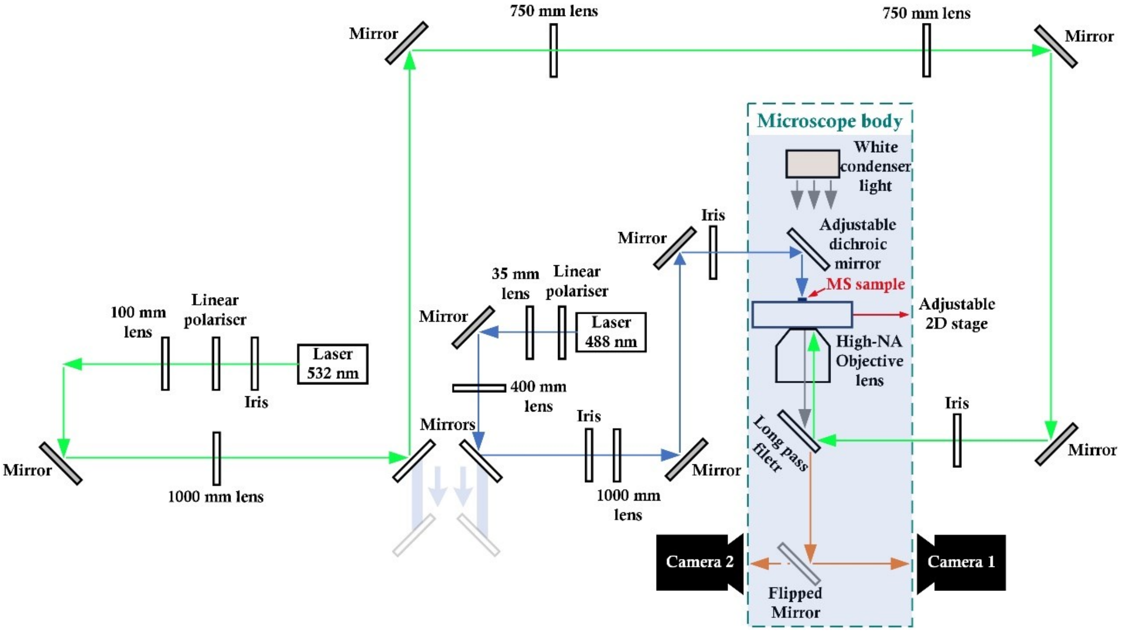

Fig. 4.6. Experimental setup for optical trapping applications at 488 nm and 532 nm.

Also, a toptica solid-state laser at 488 nm was linearly polarised and expanded to a beam of 1.2 cm with a telescope made by two lenses with focal lengths of 35 mm and 400 mm. Again, the selection of lenses was made to ensure the output beam would cover the whole area of the next lens. Then, the beam was focused on the metasurface that was mounted on an adjustable microscope 2D stage via a periscope, with a lens with a focal length of 1000 mm. This setup produced a spot size of ~250 µm in diameter at the MS. Given the long focal distance of 1000 mm and considering the input beam covering the whole area of the lens, the focused beam with a good approximation can be considered as a plane wave. To access the objective lens atop with laser beam at 532 nm, the three mirrors illustrated in Fig. 4.6 were displaced.

It should be emphasized that the alignment of this setup was not an easy task and took a lot of time for different experiment runs. Delivering the green laser beam from the back of the objective was not challenging as the 4f system helped with its alignment and this part of the setup was stable and worked well. However, delivering a collimated beam from the top to the MS sample and making sure it illuminates the sample at normal incident was challenging and time-consuming. This was simply because of the small distance between the MS sample and the last optics used (dichroic mirror) combined with a set of mirrors and irises used in the setup to redirect the light up from the optical table. The periscope system combined with the mirrors used in the setup provided a good degree of freedom for alignment, but it also made the setup very sensitive to small changes. To tackle this challenge, I used an adjustable dichroic mirror providing alignment in three dimensions, to align the input beam, right before the MS sample, as shown in Fig. 4.6. To make sure the beam was illuminating at the normal incident, I used a glass microscope slid covered

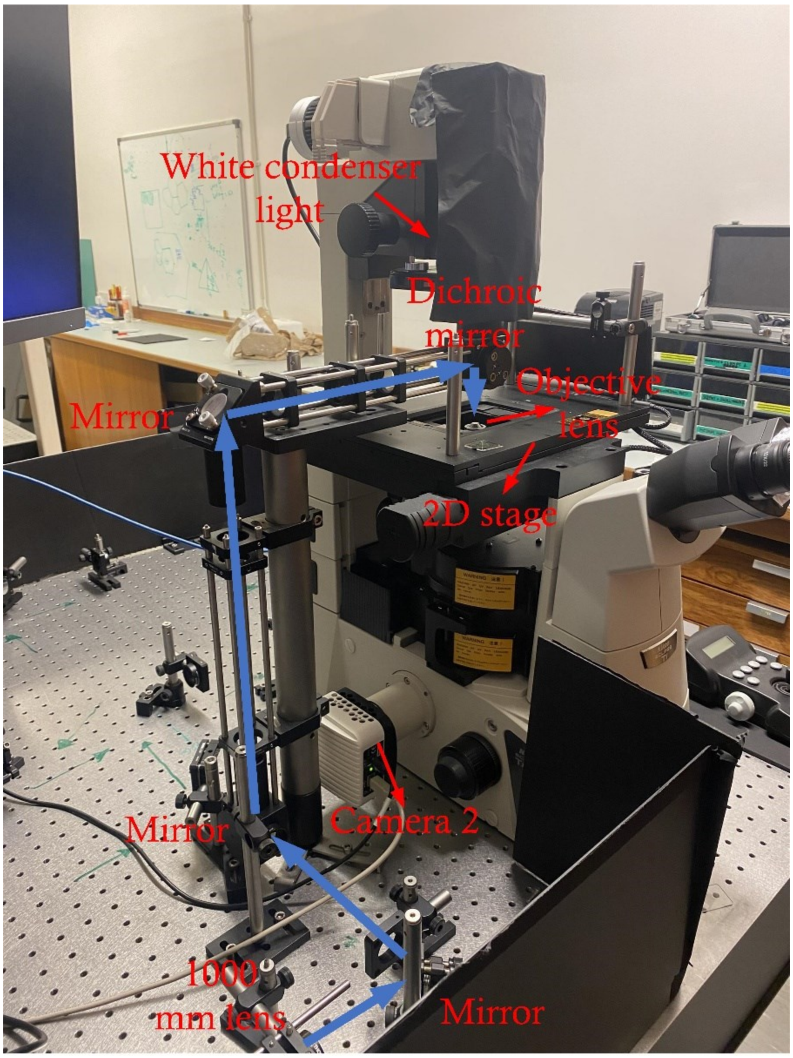

Fig. 4.7. The experimental setup for optical trapping and imaging applications at 488 nm and 532 nm.

with 200 nm gold, and placed it instead of the sample for many times. This made the beam reflect and I made sure the incident beam and the reflected beam were covering each other far away from the sample.

In this experimental setup, as Fig. 4.7 illustrates the microscope part, a Nikon microscope (Eclipse Ti-U) with a PRIOR 2D stage providing movement in the x- and y-axis for alignment, was used. Also, this setup provided a calibration in the z-axis where one can trace the movement in the z-axis with regard to the image plane. In the experiment, I used two cameras: ININITY3-3UR, mainly for alignment, and a Baumer VCXU-13M for recording purposes. I recorded the images and videos exploiting the condenser white light of the microscope where a long pass filter was set before the camera. Importantly, a water immersion 60X microscope objective lens with NA = 1.2 was used for experimental and recording purposes.

More details about the use of this setup will be provided in Chapter 6, where the experiments are described.

4.3 Conclusion

The experimental setups required to characterise the holographic MSs for efficiency measurements and optical trapping applications were presented. The method of measuring their efficiency was described and experimental images were shown. The optical trapping setup with two lasers operating at 488 nm and 532 nm was discussed in detail and the challenges and solution were highlighted. In the next Chapters 5 to 7, I will discuss how these setups are used in different applications.

4.4 Contribution

I made the required setup to characterise the efficiency of the MSs. Also, I customised the optical trapping setup which was already built to satisfy my needs. I re-aligned it from scratch several times to optimise the coupling from the top.

Chapter 5

Conformable polymeric metasurfaces for holographic applications at visible wavelengths

This chapter details a new class of flexible MSs that was explored in this thesis. Photonic MSs are commonly constituted through the periodic arrangement of meta-atoms, each comprising two or more distinct materials. This essential prerequisite imposes notable constraints during the design and manufacturing processes, which are especially prominent in the context of adaptable and conformable MSs. Here, I report on the design and fabrication of a new class of MS membranes for holographic applications constructed solely from polymeric materials, which are efficient and polarisation-independent across the visible spectrum. These findings represent a substantial stride toward streamlining the mass production of flexible holographic MSs.

5.1 Introduction

MSs can be designed using different approaches such as Huygens', Pancharatnam-Berry, and High-contrast techniques, as expounded in Chapter 1. Irrespective of the chosen methodology to design meta-atoms, these approaches generally require the integration of multiple materials, which is essential to elicit the desired response from the meta-atoms, such as embedding high-contrast dielectric nanopillars on/in a substrate with low index or resorting to plasmonic effects on metallic layers deposited over dielectric features. The presence of distinct materials within the structure increases both the cost and intricacy associated with the design and manufacturing processes.

This constraint is of great importance in the context of flexible holographic metasurfaces (FHMS), which are conventionally fabricated using pliable substrates that house either dielectric or metallic nano-features, situated either on their surface or embedded within the flexible support, to create the meta-atoms [47, 75, 106].

When compared to flat and rigid holographic metasurfaces (HMSs), FHMSs extend the design possibilities for generating high-quality holograms. They can be applied conformally to a variety of chosen surfaces, providing the target object with customized photonic capabilities, independently from the material or shape of the underlying target object [47]. On the other hand, the resulting holographic information can be designed in a way that either exhibits resilience to deformation [47] or be intricately linked to the contours of the support structure [75, 105-106].

Despite the capabilities offered by sophisticated fabrication methods to incorporate dielectric and metallic nano-features into polymeric substrates, it would be highly desirable to enable the realisation of FHMs using simple, low-refractive-index polymer materials.

This approach would alleviate numerous design and manufacturing limitations, enabling the comprehensive utilization of the diverse attributes inherent to polymers. For instance, depending on the specific application, it would become feasible to fine-tune aspects such as flexibility, cost-effectiveness, ease of manufacturing, weight, and stretchability.

Here, I present a thin-film all-polymeric FHMS membrane operating in the visible range. This is similar to traditional instances of photonic crystals [154], which are offered for sensing and filtering applications [156-158]. Within the landscape of MS technology, this kind of transparent membrane has recently been proposed for imaging in the infrared region [159]. However, here, a transparent MS membrane is proposed to work in the visible range with the engineered meta-atoms inside a polymeric membrane.

The proposed structure works in transmission and offers a full 2π phase modulation of the scattered light, as described in detail in Chapter 2. In the following, the hologram design, fabrication, discussion on imperfections, and holographic images across the visible spectrum are presented.

5.2 Design

This part outlines the design of meta-atoms and the hologram for visible light holography. Notably, the meta-atom design was presented in Chapter 2. Here, I describe the design of meta-atoms in more detail, considering their operation at other visible wavelengths. Then, the hologram design for efficiency measurements and holographic imaging across the visible range are presented.

5.2.1 Meta-atom design

This approach can be realised by exploiting any suitable material that shows the capability of patterning using nanofabrication techniques. In this context, I opted to utilise SU-8, a widely used epoxy-based negative-tone resist, amenable to precision patterning through both photolithography and electron beam lithography techniques [160], and exhibiting long-term stability [161]. SU-8 films offer versatility in thickness, ranging from several tens of nanometres to several hundred microns, and can be patterned in high aspect ratio features. Furthermore, SU-8 exhibits a comparatively elevated average refractive index ($n_p \simeq 1.58$) and negligible absorption coefficients across the entire visible range, as shown in Fig. 5. 1.

In the interest of readability and clarity, Fig. 5. 2(a-b) shows a sketch of the meta-atom, with $t_a = 1$ µm, $p = 300$ nm, $t_p = 0.0$ nm, and its optical response at $\lambda = 532$ nm, as presented in Chapter 2.

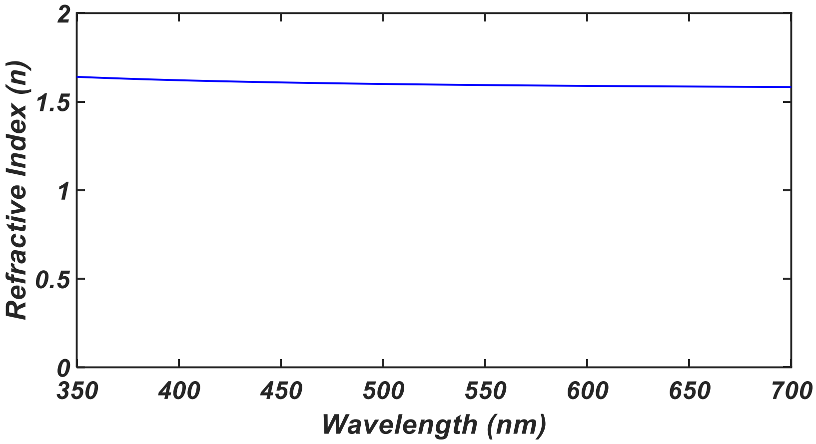

Fig. 5.1.SU-8 2000 (Microchem) refractive index across the visible range [162].

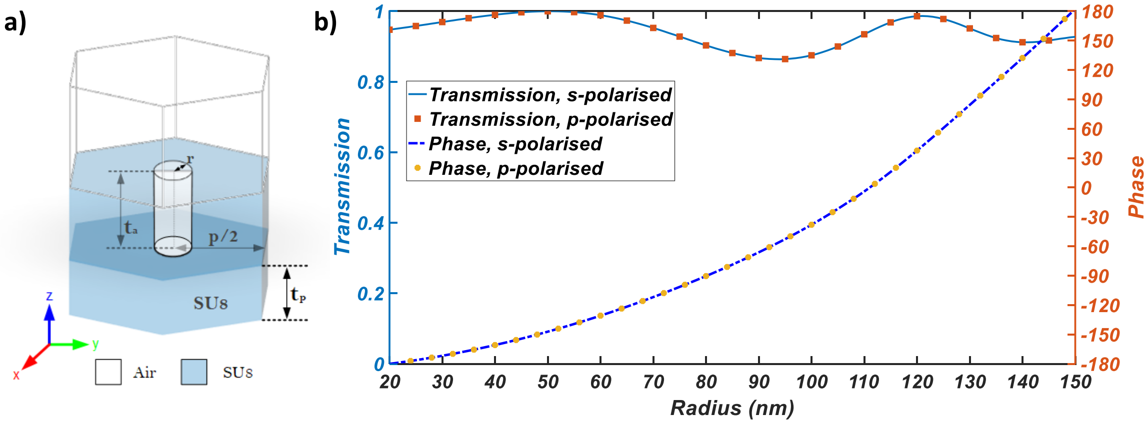

Fig. 5.2. (a) Schematic view of the SU-8 meta-atoms. (b) Optical response of the SU-8 meta-atom designed at 532 nm for both polarisations.

The dependence of the optical response of the meta-atoms from its geometrical parameters has already been studied in Chapter 2. It is noteworthy to remember that for a constant t_a, the phase shift is fully determined by the pillar radius, whereas t_p has minimal effect on the qualitative response of the device. Therefore, it is best to have $t_p>t_a$ for practical purposes.

Here, I will elaborate on the optical response of the designed meta-atoms at other visible wavelengths than the designed wavelength (λ_d = 532 nm). This could open a vision to understand the optical behaviour of the final device across the visible range spectrum.

Figures 5.3(a-b) illustrate the phase and transmission response of the optimised meta-atoms for operation at λ_d but excited at λ=488 nm and λ=632 nm, respectively.

As expected, at shorter wavelengths, the phase modulation covers a range superior to 2π, as shown in Fig. 5.3(a). This means that having a working device with 2π phase coverage at λ=488 nm requires a lower height for air holes (t_a<1 μm). However, at longer wavelengths, the meta-atoms are incapable of covering 2π phase shift. Similarly, this means that having a 2π phase coverage at λ = 632 nm requires taller air holes (t_a>1 μm). In both cases, the transmission is qualitatively similar and offers an average transmission greater than 85%. However, I expect a reduction of the efficiency due to dephasing, but the degradation is more severe in the long wavelength range. This is confirmed by the experimental results to measure efficiency presented later in this chapter.

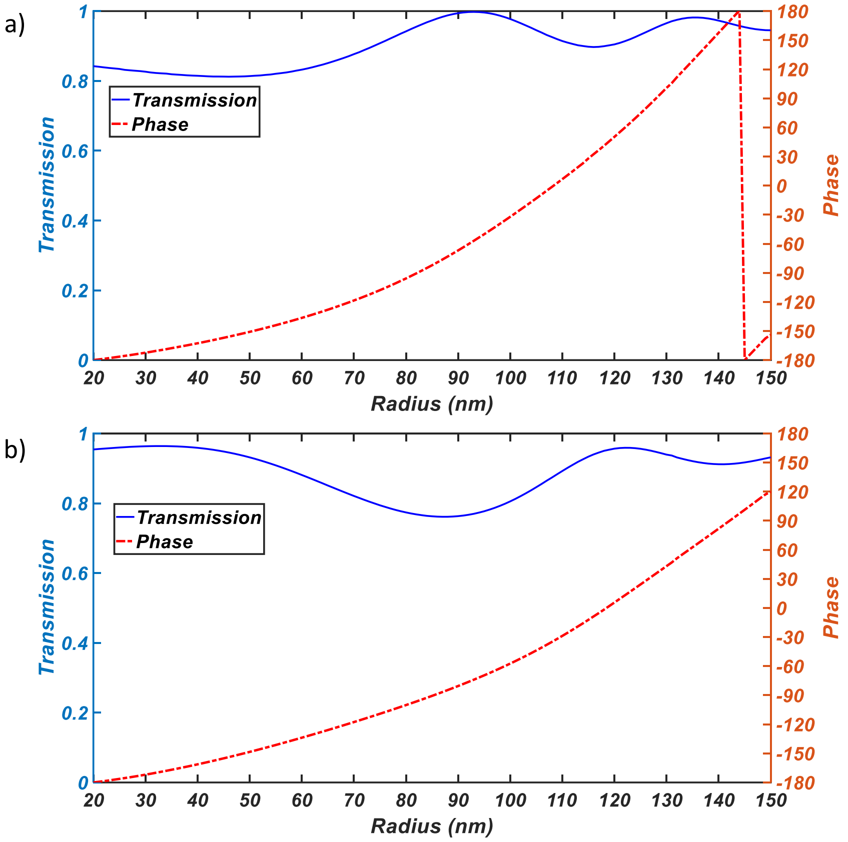

Fig. 5.3. Optical response of the SU-8 meta-atom designed at λ_d = 532 nm, but excited at (a) λ = 488 nm and (b) λ = 632 nm.

5.2.2 Hologram design

To measure the efficiency, a hologram to create a dot-shaped holographic image with the parameters reported in Table 5.1 was designed.

Table. 5.1. **Hologram parameters to design a dot-shaped hologram for SU-8 MS at 532 nm.**

Parameter	Value
Hologram resolution	666×666
Holographic image resolution	200×200
Hologram pixel pitch	300 nm
Holographic image pixel pitch	0.4 mm
Source intensity	Plane-wave
Wavelength	532 nm
Distance in z	150 mm
Holographic image offset in x-y-z	86.6,0,0 mm

Figure 5.4 reports on the target image, simulated holographic image, and the phase profile obtained by the RS numerical method for this hologram.

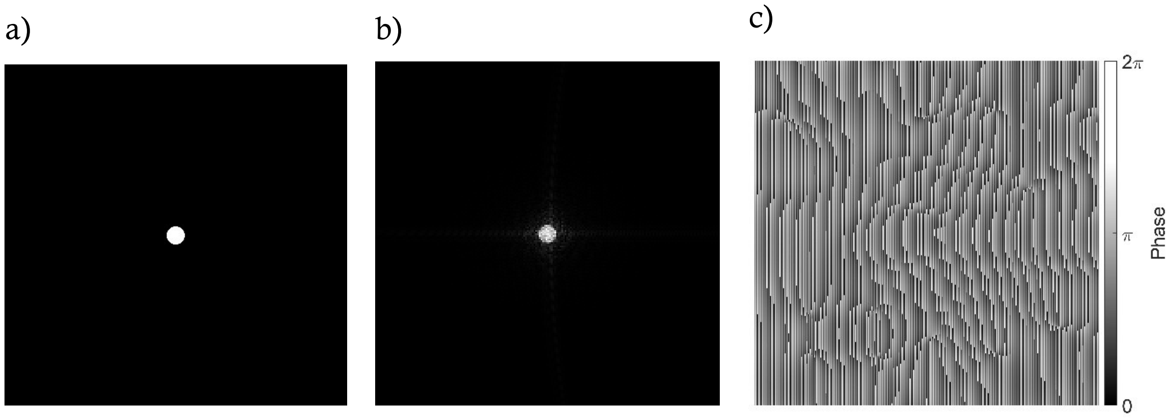

Fig. 5.4. (a) Target image to design a dot-shaped hologram. (b) Simulated holographic image. (c) Phase profile.

As a proof of concept, I designed a holographic image of a penguin image, with the parameters reported in Table 5.2.

Table. 5.2. **Hologram parameters to design a penguin hologram for SU-8 MS at 532 nm.**

Parameter	Value
Hologram resolution	667×667
Holographic image resolution	333×333
Hologram pixel pitch	300 nm
Holographic image pixel pitch	0.7 mm
Source intensity	Plane-wave
Wavelength	532 nm
Distance in z	150 mm
Holographic image offset in x-y-z	86.6,0,0 mm

Figure 5.5 reports on the target image, simulated holographic image, and the phase profile obtained by the RS numerical method for this hologram.

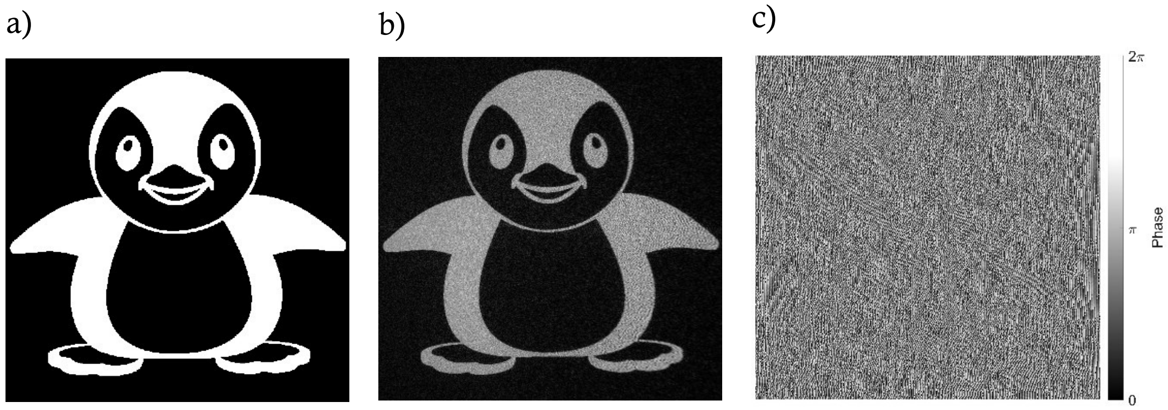

Fig. 5.5. (a) Target image to design a penguin hologram. (b) Simulated holographic image. (c) Phase profile.

The phase profile is then mapped to the required radii to realise this hologram using a MATLAB code created by myself. A 12-level phase quantisation is used, as reported in Chapter 2, which guarantees high-quality holographic images.

5.3 Fabrication

The fabrication procedure of these polymeric membranes is presented in Chapter 3. Here, I will elaborate on the fabricated devices in detail and show some SEM images of the fabricated sample. Fig. 5.6(a-c) illustrates the fabrication workflow. Fig. 5.6(d) displays the flexible membrane of the SU-8 MSs, and Fig. 5.6(e) depicts the SEM image of the sample before the RIE step. Then, to ensure the pattern was transferred to the SU-8 layer, SEM images of the final fabricated sample were taken. Figure 5.7 shows the SEM images of the SU-8 FHMS.

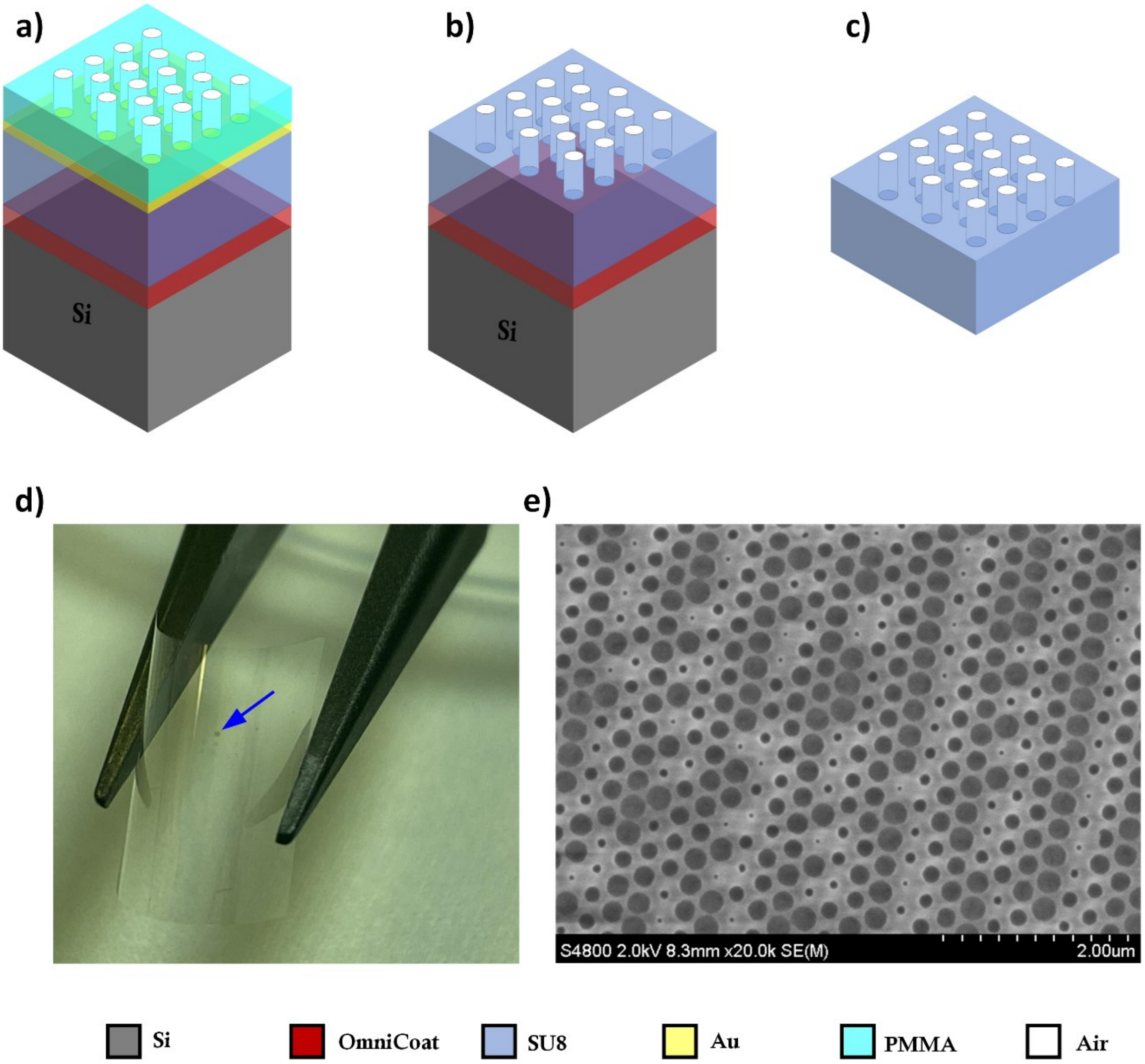

Fig. 5.6. Schematic of the fabrication workflow of the flexible SU-8 MS membrane. (a) Silicon carrier was initially coated with Omnicoat, SU-8, and gold, followed by PMMA, which was patterned through a standard EBL process. b) Following the development, the MS pattern was transferred onto the SU-8 layer. (c) The MS was released from the carrier through a lift-off process. (d) Image of the fabricated sample. The blue arrow indicates the MSs area (e) SEM image of the fabricated sample [163].

It is useful to mention it is very hard to create high-definition SEM images of the sample, and therefore make a quantitative comparison between the design and the experimental data, due to excessive electron charging. This effect is particularly strong for the fully etched sample (Fig. 5.6(c)), when no metal is present, and therefore the image had to be taken at a lower magnification, as shown in Fig. 5.7(a). However, the presented figures show that the holes were all clearly defined, and the largest holes were almost touching.

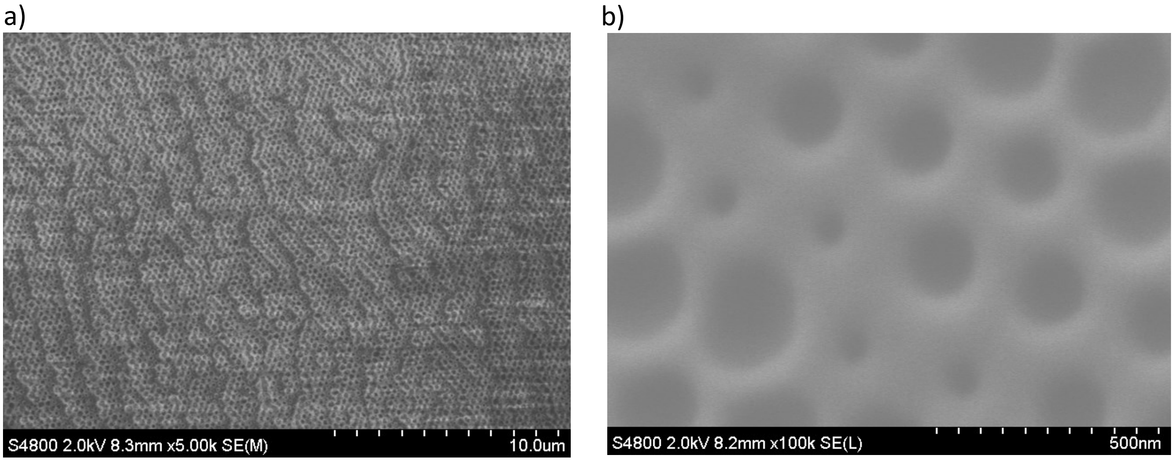

Fig. 5.7. SEM images of the SU-8 FHMS.

5.4 Experimental setup

Here, the experimental setup that was developed to measure the efficiency and acquire the holographic images made by SU-8 FHMSs is discussed. The setup was identical for efficiency measurements and obtaining the holographic images. The only difference was that to measure the efficiency, I replaced the screen with a power meter to record the power. The MSs were excited using a broadband supercontinuum laser (SuperK, NKT Photonics) in the designed wavelength in the visible range, mainly at 488 nm and 532 nm, with the setup shown in Fig. 5.8. The laser beam was passed through a linear polariser and then expanded to a beam with a diameter of 1.5 cm with a telescope made of two lenses with focal lengths of 50 mm and 400 mm. After that, the beam was focused on the MS sample with a lens with a focal length of 1000 mm to approximately act as a plane wave. The setup produced a spot size of ~250 µm in diameter at the plane of the sample at the designed wavelength. Notably, the size of the MSs for characterisation was considered 200 × 200 μm^2. The holographic images were created after the sample on the screen at the designed angle of 30 ° respect to the MS normal. Then, the images were taken by a standard camera with a fixed position with respect to the screen.

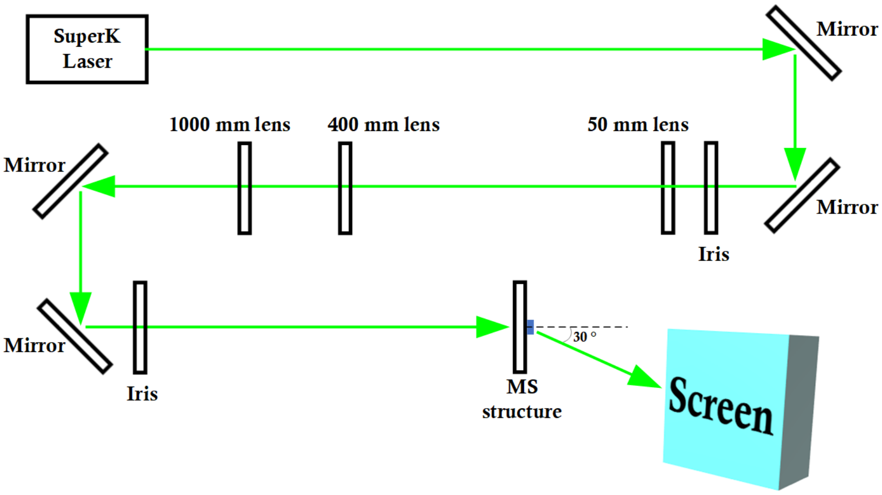

Fig. 5.8. Experimental setup to acquire the holographic image made by SU-8 FHMSs.

5.5 Results and discussion

The efficiency measurements as a function of wavelength for polarisations along with the x- and y-axis are illustrated in Fig. 5.9. The efficiency peaks at 64% at 532 nm and is lower in other wavelengths. These results show the insensitivity of the designed device to the

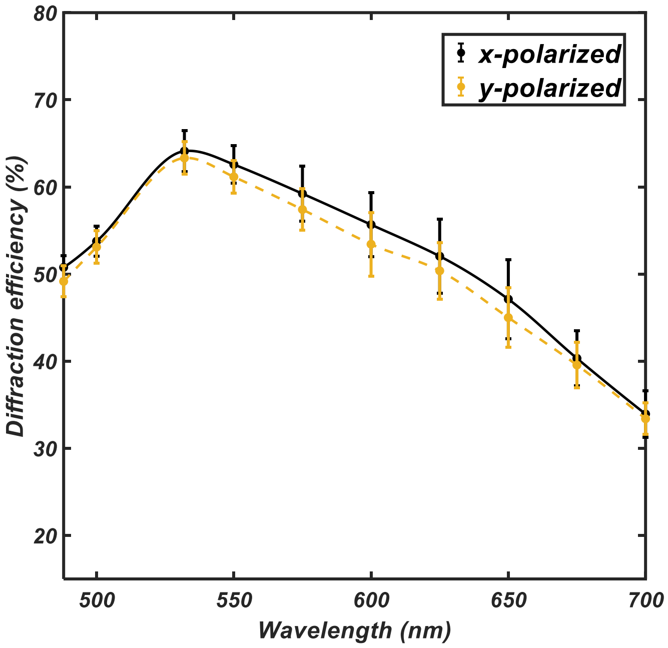

Fig. 5.9. The diffraction efficiency of the SU-8 MS designed at 532 nm as a function of wavelength for x- and y-polarised light [163].

polarisation state of the incident light. The measured values for both polarisations are not completely matched, which contributes to the imperfections in the experiments. It is useful to mention at wavelengths except the design wavelength, the inability of the MS to modulate the phase as designed, results in lower efficiency.

It is noteworthy to compare the efficiency of this platform with the efficiency of other MSs operating in the visible region. For instance, MSs with high refractive index meta-atoms achieved efficiencies >66% in transmission [88, 164], while those employing metal-insulator-metal meta-atoms reached an efficiency of 80% in reflection [56].

Figure 5.10 demonstrates the experimental holographic image of the MS membrane, displaying a target image positioned 15 cm away from the MS at a 30-degree angle relative to the normal incident. The MS membrane is placed on a glass slide for practical considerations. It is emphasised that the observed results remain consistent whether the MS is framed and suspended or positioned on a glass slide.

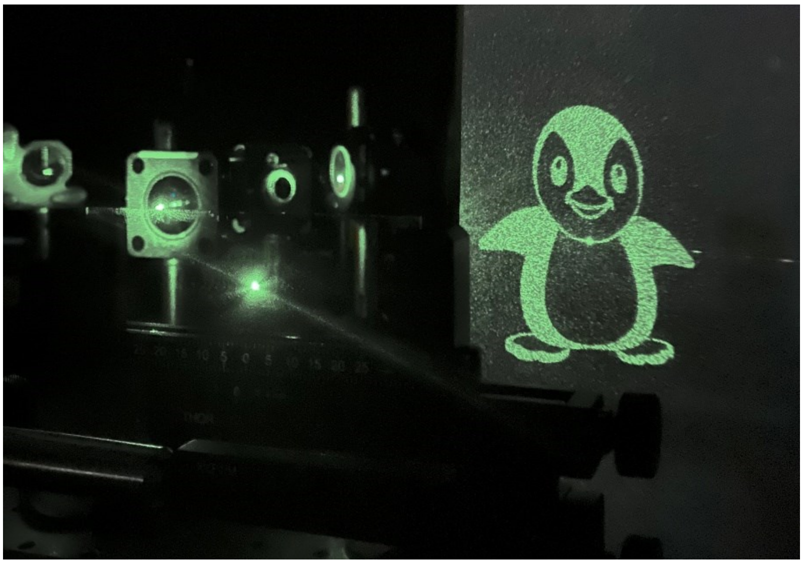

Fig. 5.10. Experimental results of the SU-8 FHMS sample for holographic imaging at λ= 532 nm [163].

To reveal the broadband operating ability of the proposed structure across the visible range, the same MS was illuminated with different wavelengths in the 488 nm to 632 nm range, and the corresponding holographic images were obtained, as shown in Fig. 5.11. As expected, and due to the diffraction effect, the image size and position change with the operation wavelength, as it is clearly illustrated in this figure.

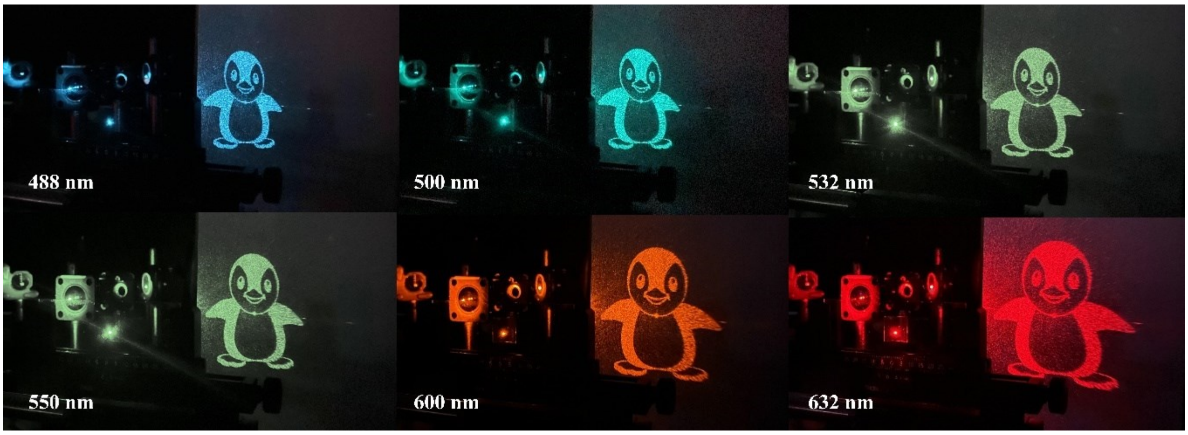

Fig. 5.11. Experimental measurement of the holographic imaging of the SU-8 FHMS membrane across the visible range [163].

To illustrate the capability of the experimented MS to operate effectively over a range of wavelengths, it is useful to study the created images with signal-to-noise (CNR) and contrast-to-noise (CNR) ratios. Figure 5.12 illustrates the SNR and CNR for images projected in different wavelengths. It should be mentioned that part of the projected images has been used to extract these values, hence the results should be considered in this context.

As expected, this approach exhibits versatility across a broad and diverse range of materials. For example, Fig. 5.13 illustrates the amplitude and phase characteristics of the transmitted light through a unit cell, considering PMMA and crystalline silicon with SU-8. In this instance, the lattice constant for the PMMA unit cell was maintained at 300 nm, as identical to the SU-8 case. However, a periodicity of 190 nm was considered for the silicon case.

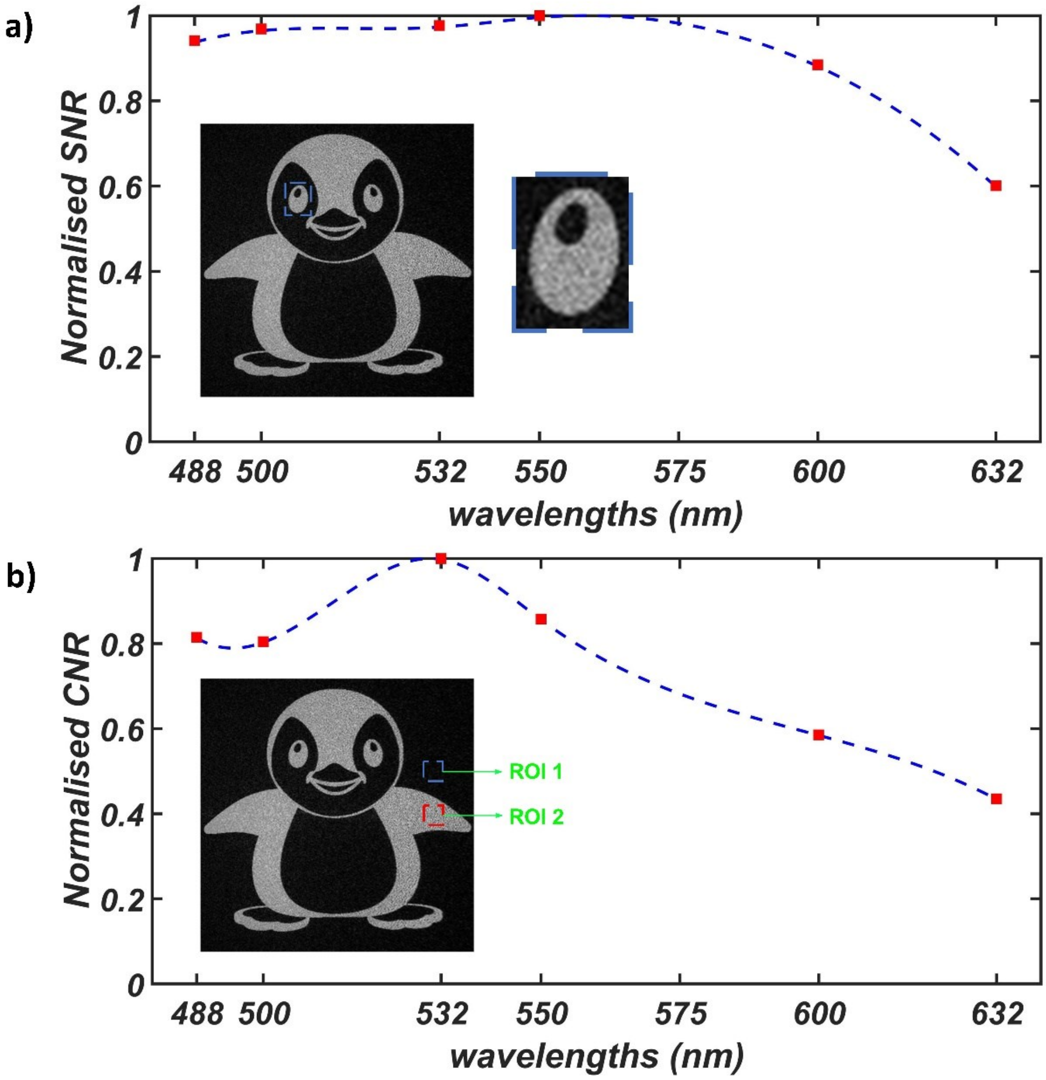

Fig. 5.12. Illustration of the (a) CNR and (b) SNR for created images in different wavelengths. The blue rectangular shape in (a) indicates the selected part of the image for calculations. ROI 1 and ROI 2 in (b) indicate the region of interest used in calculations for background and signal, respectively. Red squares are measured experimental points. The blue discontinued line is an interpolation between the red squares.

The determined minimum thicknesses ensuring complete 2π phase coverage were 1.170 μm for PMMA and 230 nm for silicon. The elevated refractive index of silicon induces a more severe phase modulation with the dimension of the air holes, resulting in a considerably reduced membrane thickness. This means the silicon MS membranes are more sensitive than SU-8/PMMA cases.

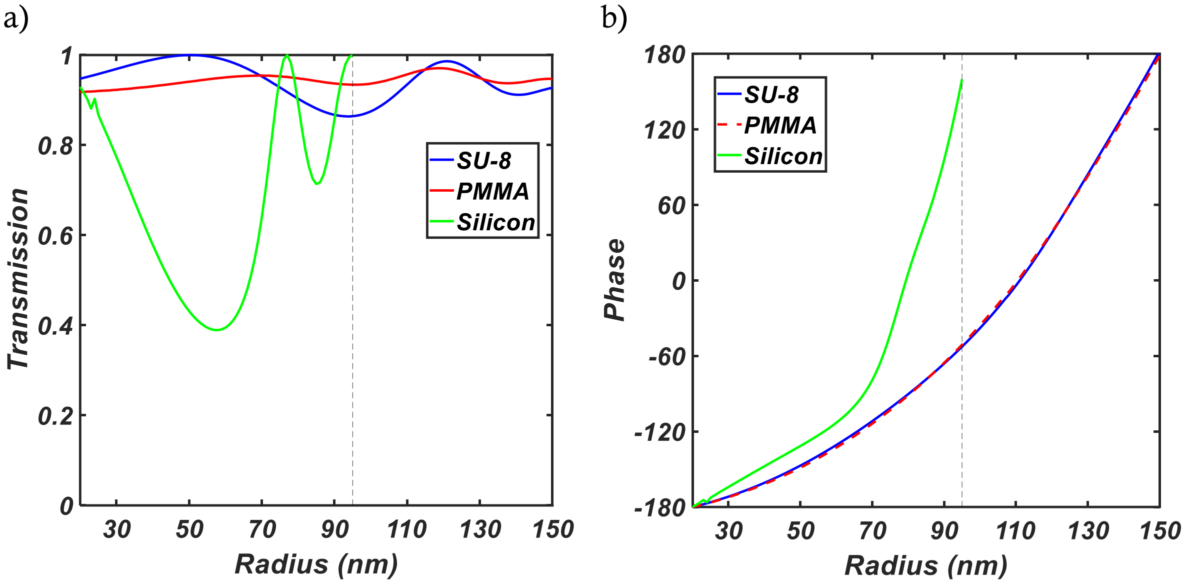

Fig. 5.13. Comparing the (a) transmission and (b) phase modulation of PMMA, and silicon with SU-8 membrane [163].

It is noteworthy that, even in the case of crystalline silicon, the flexibility and conformability of the nanomembranes can be effectively leveraged [153], as mentioned in Chapter 2. However, the heightened impedance mismatch with the surrounding environment and material absorption contribute to a less favourable transmission.

Exploiting PMMA is attractive due to its amenability to straightforward direct electron-beam exposure, albeit at a slightly increased thickness. Alternative polymeric materials, such as PDMS, hold promise for making stretchable and tuneable MSs, capitalising on their flexible and conformable nature. Moreover, the fabrication of this category of MSs can be upscaled using suitable polymers through hybrid nano-imprinting and etching techniques [165].

This class of MSs has the potential for additional refinement to exhibit sensitivity to a specific polarisation, should it prove advantageous for the intended application. Achieving this characteristic can be realised by defining non-symmetrical air holes.

It is important to highlight that holographic MSs composed of single materials generally exhibit a reduced range of versatility in controlling the scattering properties of the meta-atoms. Nevertheless, this limitation is compensated by the straightforwardness of both design and fabrication processes. Particularly, such simplicity is advantageous for applications in sensing [166-167] and augmented reality [168], wherein strong scattering efficiencies are not inherently crucial.

5.6 Conclusion

In summary, I introduced a flexible and polarisation-independent holographic MS membrane operating in transmission across the visible range. In contrast with most realisations of MSs, our devices can be constructed using a single transparent material, such as a low refractive index polymer. I conducted a comprehensive study on the impact of both geometric and material parameters of the meta-atoms, backed by experimental characterisation of the fabricated samples. The proposed flexible and highly transparent MS membranes offer a distinctive foundation for advancing scalable applications in augmented reality, sensing, and Biophotonics.

5.7 Contribution

I designed the holograms and ran all the simulations. I carried out all the fabrication steps for all samples related to this chapter from similar processes utilised in the Synthetic Optics research group. Also, I customised and developed the existing recipes for fabrication procedures to satisfy my needs. In particular, I worked with Nanofabrication tools, including Spin coater, EBL eLine Plus, Ebeam evaporator, RIE, Dek-talk profiler, and EVG system. In addition, I worked with a variety of photoresists and materials to develop a working recipe for the fabrication of SU-8 membranes. I made the required setup for the characterisation of holographic imaging and ran all the experiments. In general, I made approximately twelve SU-8 samples.

Chapter 6

Holographic metasurfaces for imaging and optical trapping applications in the visible range

This chapter details the realisation of lab-on-chip holographic MSs employed for optical trapping and imaging applications in the visible range, exploiting excellent optical and mechanical properties of ZrO_2.
Visible light holographic MSs offer advanced imaging capabilities within compact, planar systems. The precise control and structuring of light are crucial in lab-on-chip biophotonic applications, where manipulating light with high accuracy and flexibility is essential. Dielectric holographic MSs are limited to near-infrared and larger wavelengths of the visible range due to considerable absorption loss. Overcoming the challenge of extending operational wavelengths into smaller wavelengths, this study demonstrates the suitability of ZrO_2 MSs for this purpose. Here, I demonstrate the efficient operation of high numerical aperture ZrO_2 holographic MSs for imaging and optical trapping at wavelengths as low as 532 nm and 488 nm.

6.1 Introduction

In biophotonics experiments, working in the near-infrared (NIR) is advantageous as phototoxicity and light absorption in tissues can be minimised. However, visible-range imaging is predominant in most experiments, especially for leveraging fluorescence-based assays to enhance imaging resolution. Shorter wavelengths are commonly employed to excite fluorophores and dyes in this concept.

Various platforms can be employed to realise HMSs. Plasmonic meta-atoms exhibit outstanding performance in reflection [47, 56]. However, their implementation in the visible spectrum is challenging due to intrinsic losses and complicating biophotonics experiments with issues like localised absorption and heat. Silicon-based HMSs demonstrate good performance in the amorphous phase (a-si) and crystalline phase (c-si) [163, 169], but they are limited to the 532 nm region due to absorption losses. For instance, Metalenses with a numerical aperture up to 1.48 and efficiency exceeding 42% have been reported [79, 94, 164]. Titanium dioxide is another interesting material. TiO_2 HMSs emerge as promising candidates for visible range applications, with reported NA of 0.8 to 1.1 and having efficiencies from 78% to 50% [88-89, 170, 171], particularly in the crystalline form, which exhibits high refractive indices. Moving to smaller wavelengths, recent advancements include HfO_2 MSs operating in the UV range with a reported NA of 0.6 and an efficiency of 60% [154].

Here, I contend that ZrO_2 is a compelling and viable alternative to other platforms for HMSs within the visible range, particularly in applications for biophotonics and optical trapping (OT). Given its exceptional properties, in recent studies, the utilization of nanoimprinting techniques has facilitated the realisation of MSs using ZrO_2 nanoparticles, across the visible [172] and deep ultraviolet (UV) spectra [173]. Notably, these ZrO_2 nanoparticles exhibit a slightly lower refractive index and have a higher loss in deep UV spectra compared to bulk ZrO_2.

In this study, I show the ability of ZrO_2 MSs within microfluidic environments by demonstrating ZrO_2 HMSs tailored for optical trapping applications in the green and blue regions of the visible spectrum. OT, a non-invasive technique, enables precise manipulation of micron-sized particles [174] and smaller objects without direct contact. This manipulation is usually achieved by creating specific optical potentials, such as strongly focusing Gaussian beams to spot sizes comparable to that of the trapped object. The trap stiffness, indicative of the spring constant of the damped oscillator describing the trapping potential [175], is influenced by the power, wavelength, as well as optical and geometrical parameters of the trapped object [176]. OT is an invaluable method for measuring forces in the pN regime, by following the displacement of the trapped object on the nanometric scale. This capability has elevated OT to an outstanding tool for probing biophysical dynamics down to the single-molecule level [177]. Furthermore, OT has been employed to trap living cells directly [178], manipulate nanostructures within living organisms [179], facilitate in-situ assembly of microscopic structures [180], and manipulate extended objects [181].

Many of these experiments utilise bulky, high numerical aperture objectives, necessary for achieving a balance between the optical scattering and gradient forces acting on the trapped object. Hence, the adoption of MSs technology for OT applications holds significance. In the NIR range, metalenses (based on silicon platforms with NA up to 0.88) yield a trap stiffness of up to 0.02 pN/µm/W [182]. Also, by employing plasmonic-based platforms, trap stiffness up to 0.013 pN/µm/W (NA = 0.7) has been reported [183]. Recently, using reflective-type PB MSs, these performance metrics have been updated to values comparable to objectives with NA=1.2, and trap stiffness greater than 400 pN/µm/W [184].

Optical trapping in the visible range is rewarding but more challenging. OT in the visible spectrum, in comparison to the NIR, offers increased trapping forces (which scale advantageously with the inverse of the wavelength used). This is a crucial factor for manipulating and controlling small objects. Nevertheless, trapping at shorter wavelengths introduces additional challenges due to the comparable sizes between the periodicity of the MSs and the wavelength of the incident light. This makes achieving a high NA even more difficult in the visible region. A recent development in the visible range involves adaptive Fresnel metalenses that exploit a patterned polymer on the tip of an optical fibre with an NA of 0.88, working at the wavelength of 660 nm, and resulting in a trap stiffness of 100 pN/µm/W [185].

Here, I present broadband transmissive HMSs made of ZrO_2, having a numerical aperture as high as 1.2 within the visible range. These ZrO_2 HMSs are designed for on-chip optical trapping and imaging applications, specifically at wavelengths of 488 nm (blue HMSs) and 532 nm (green HMSs). The experimentally measured trapping stiffness for these devices indicates the trap stiffness of 212 pN/µm/W and 130 pN/µm/W, for blue and green HMSs, respectively.

6.2 Design

This part presents the considerations for the design of meta-atoms and holograms for efficiency measurements, holographic imaging and optical trapping. The design procedure of the meta-atoms for both applications was presented in Chapter 2. Here, I present the hologram design for efficiency measurements and image projection with the HMSs designed for holographic imaging. Then, I detail meta-atom designs, considering high NA requirements for optical trapping in the visible range. Following this, I present the hologram designs for efficiency measurements and optical trapping experiments.

6.2.1 Meta-atom design

The ellipsometer (J.A. Woollam) was used to measure the refractive index of the deposited amorphous ZrO_2 in the visible range and UV spectrum. Appendix B illustrates a comparison between the refractive index of the deposited ZrO_2 with that of reported works. Figure 6.1(a) illustrates the comparison of the refractive index of ZrO_2 with those of silicon and TiO_2. The data show that the deposited ZrO_2 possesses a high refractive index that spans from the visible range well into the deep UV region, with negligible absorption. In the interest of readability and clarity, Fig. 6.1(b) illustrates a perspective of the proposed ZrO_2 unit cells of the HMSs that are structured in a honeycomb lattice and fully described in Chapter 2.

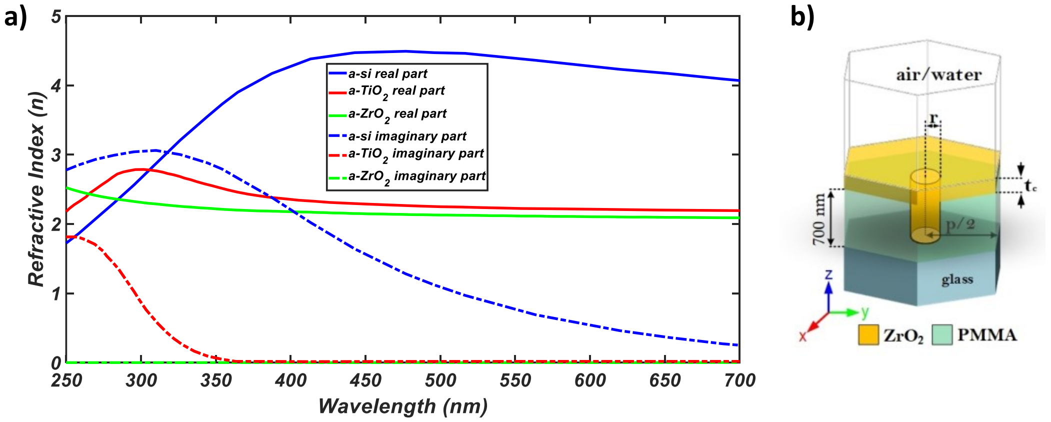

Fig. 6.1. (a) Comparison of amorphous ZrO_2 refractive index with that of si and TiO_2, and (b) perspective of the ZrO_2 unit cell design.

The corresponding transmission and phase modulation of the designed meta-atoms for both blue and green HMSs, working in air and water media, were described and fully explained in Chapter 2. The transmission of the meta-atoms for both green and blue HMSs was consistently greater than 80% in water. The meta-atoms working in the air were considered to enable efficiency measurements and show the HMS' capability for creating holographic images.

Though the transmission of the meta-atoms is affected by the surrounding medium, e.g. the transmission is higher in the water environment simply due to the elevated refractive index of water compared to air, the phase shift is unchanged. This means that the phase modulation of the meta-atoms is not dependent on the working environment, simply due to the ZrO_2 cap on top of the unit cell, which works as a separating wall between the unit cell core and the working medium. This planar ZrO_2 wall protects the supported modes of ZrO_2 meta-atoms against the environment.

6.2.2 Hologram designs for efficiency measurements at 488 nm and 532 nm for holographic image projection applications

Two different sets of MSs were designed for holographic imaging and optical trapping applications. The main difference between them was the periodicity of the MSs, as holographic imaging does not necessarily require high NA which limits the MS periodicity, whereas smaller periodicity is necessary for optical trapping to achieve high NA. This matter will be discussed in detail following this section.

To design a hologram to measure efficiency for holographic imaging applications, the parameters reported in Table 6.1 were used.

Table. 6.1. **Hologram parameters designed for efficiency measurements for holographic imaging applications.**

	Parameter	**Value**
488 nm	Hologram resolution	500×500
	Holographic image resolution	100×100
	Hologram pixel pitch	400 nm
	Holographic image pixel pitch	0.7 mm
	Source intensity	Plane-wave
	Wavelength	488 nm
	Distance in z	200 mm
	Holographic image offset in x-y-z	115.47,0,0 mm
532 nm	Hologram resolution	666×666
	Holographic image resolution	100×100
	Hologram pixel pitch	300 nm
	Holographic image pixel pitch	0.7 mm
	Source intensity	Plane-wave
	Wavelength	532 nm
	Distance in z	200 mm
	Holographic image offset in x-y-z	115.47,0,0 mm

Figure 6.2 reports on the target images, simulated holographic images, and the phase profiles obtained by the RS numerical method for these holograms.

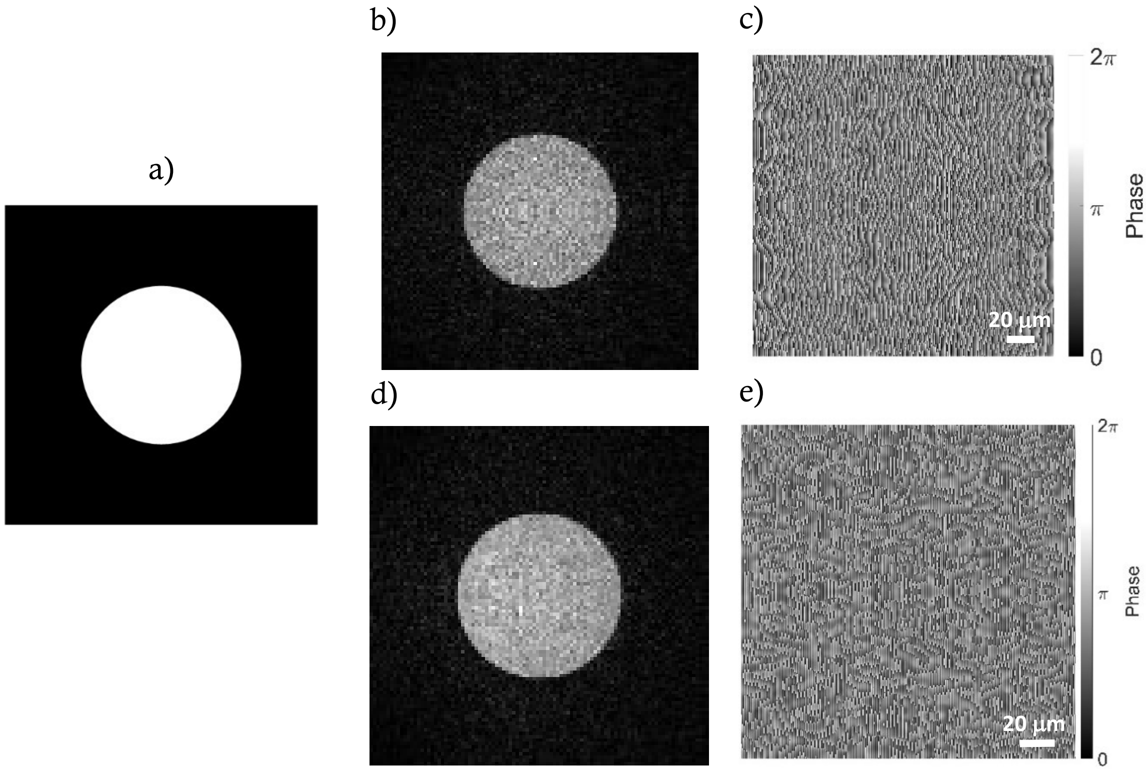

Fig. 6.2. (a) Target image to design a dot-shaped hologram. (b-c) Simulated holographic image and obtained phase profile at λ = 488 nm. (d-e) Simulated holographic image and obtained phase profile at λ = 532 nm.

6.2.3 Hologram design of a deer image for holographic image projection

To validate the performance of the proposed MSs, a deer image as a holographic image with the parameters reported in Table 6.2 was designed. Figure 6.3 reports on the target image, simulated holographic image, and the phase profile obtained by the RS numerical method for this hologram.

Table. 6.2. **Hologram parameters to design a deer hologram for ZrO_2 MS at 532 nm.**

Parameter	Value
Hologram resolution	660×660
Holographic image resolution	300×300
Hologram pixel pitch	300 nm
Holographic image pixel pitch	0.5 mm
Source intensity	Plane-wave
Wavelength	532 nm
Distance in z	150 mm
Holographic image offset in x-y-z	86.6,0,0 mm

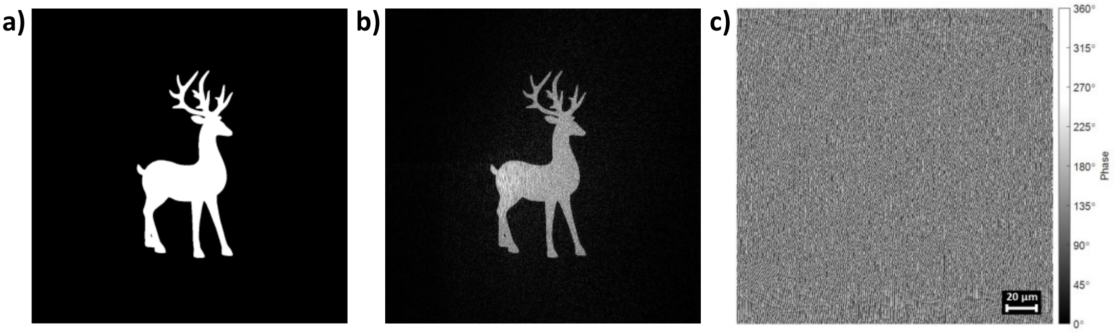

Fig. 6.3. (a) Target image to design a deer hologram. (b) Simulated holographic image at λ = 532 nm. (c) Phase profile.

6.2.4 High NA metasurface design

The NA of a focusing MS is limited by the periodicity of the meta-atoms, following the Nyquist–Shannon sampling theorem in the spatial domain [170]:

$$p \leq \lambda_d/2.NA \qquad (1)$$

Where p is the periodicity, λ_d is the designed wavelength. For instance, in my case, the MSs designed at λ_d = 488 nm and λ_d = 532 nm have p = 200 nm and 210 nm, respectively. This corresponds to a maximum achievable NA of 1.22 and 1.26, respectively. Figure 6.4 illustrates the plot of equation (1) for the case of λ_d = 532 nm.

This limitation can be considered in terms of the focal length (F) of the structure and its side length (L). Given a specific focal length, the maximum area of the MS and the periodicity of the meta-atoms impose limitations on the NA of the lens. To this end, and considering optical trapping using MSs, it can be noted that the maximum trapping distance to guarantee $NA = n_m \sin(\varphi)$, is derived by $\mathrm{F} = L \frac{n_m}{2\mathrm{NA}} \sqrt{1 - (\frac{\mathrm{NA}}{n_m})^2}$ [184], where φ is the half angle of the focal length, and n_m is the medium refractive index.

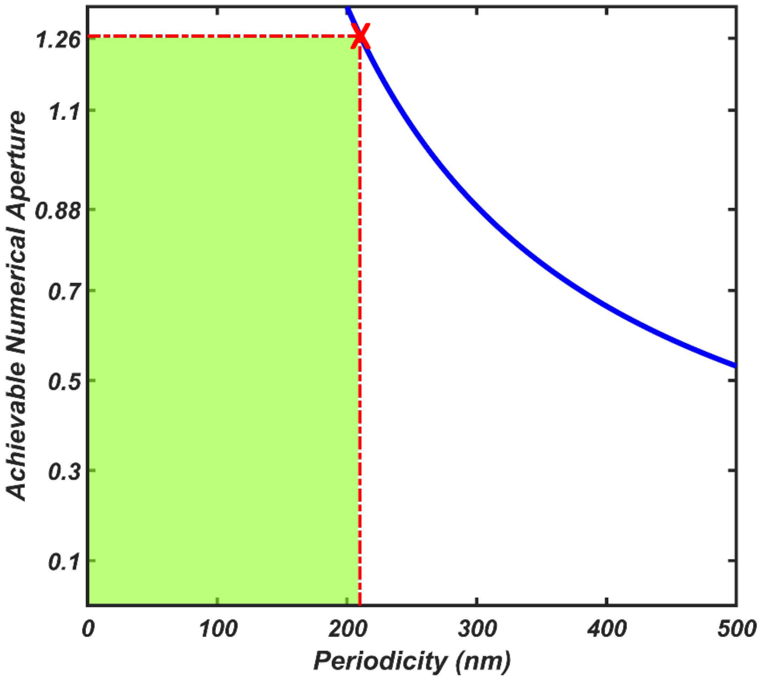

Fig. 6.4. Illustration of the achievable NA versus the MS periodicity. Considering λ_d = 532 nm, the blue curve shows the plot of equation 1. The green box depicts that with p = 210 nm, the maximum achievable NA is 1.26.

Figure 6.5 illustrates how the ratio ζ=F/L can be chosen to guarantee the selected periodicity meets the requirements of the designed NA.

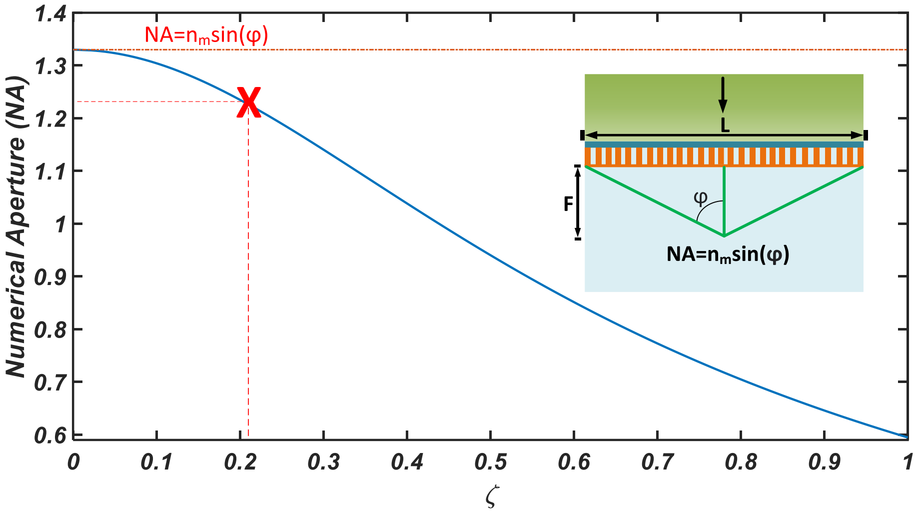

Fig. 6.5. The ratio of focal length over side length of an MS to guarantee the designed NA. Here, water was considered as the medium with n_m = 1.33. The red cross shows having ζ = 0.21 guarantees NA of 1.22.

6.2.5 Hologram designs for efficiency measurements at 488 nm and 532 nm for optical trapping applications

As explained before, due to the requirement of a high NA lens for optical trapping, the periodicity was chosen to be reduced to 200 nm and 210 nm for λ = 488 nm and λ = 532 nm, respectively. To design a hologram to measure the efficiency of these MSs, the parameters reported in Table 6.3 were used.

Table. 6.3. **Hologram parameters designed for efficiency measurements for optical trapping applications.**

	Parameter	**Value**
488 nm	Hologram resolution	1000×1000
	Holographic image resolution	100×100
	Hologram pixel pitch	200 nm
	Holographic image pixel pitch	0.7 mm
	Source intensity	Plane-wave
	Wavelength	488 nm
	Distance in z	150 mm
	Holographic image offset in x-y-z	86.6,0,0 mm
532 nm	Hologram resolution	952×952
	Holographic image resolution	100×100
	Hologram pixel pitch	210 nm
	Holographic image pixel pitch	0.7 mm
	Source intensity	Plane-wave
	Wavelength	532 nm
	Distance in z	150 mm
	Holographic image offset in x-y-z	86.6,0,0 mm

Figure 6.6 reports on the target image, simulated holographic images, and the obtained phase profiles by the RS numerical method for this hologram. It should be noted that the existence of the gradient shown in Figs. 6.6(b, d) arises due to early termination of the GSA. The effect of the gradient on efficiency measurements is negligible.

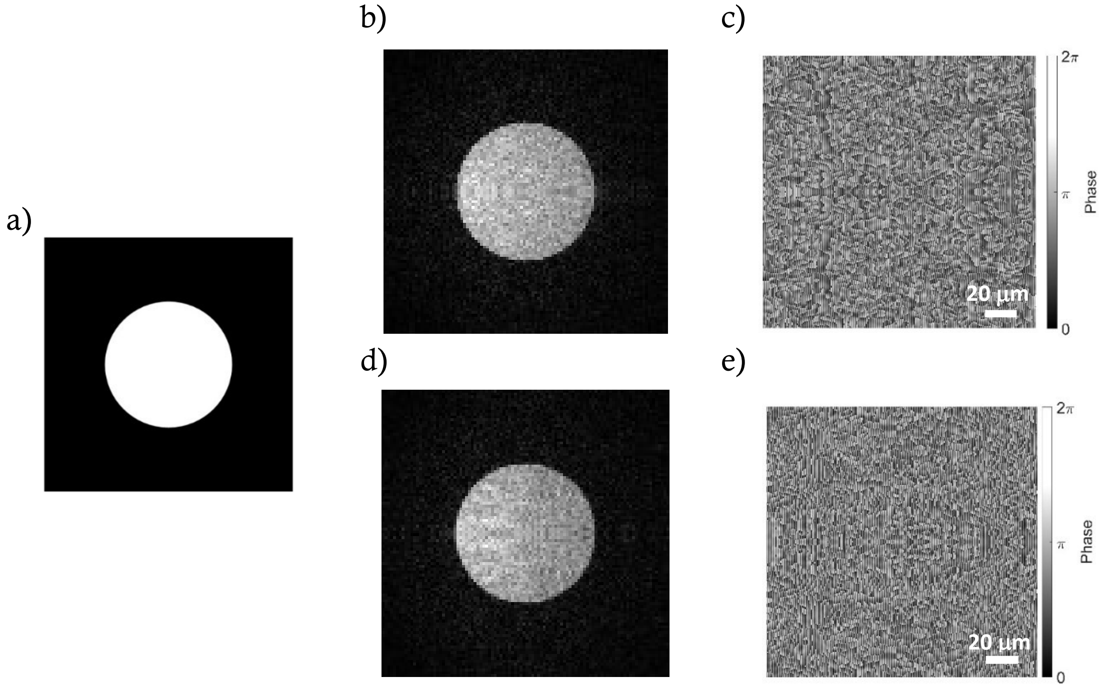

Fig. 6.6. (a) Target image to design a dot-shaped hologram. (b-c) Simulated holographic image and obtained phase profile at λ = 488 nm. (d-e) Simulated holographic image and obtained phase profile at λ = 532 nm.

6.2.6 Hologram designs for high NA metasurfaces at 488nm and 532 nm for optical trapping

Figure 6.7 illustrates the concept of optical trapping using an MS. In this figure, a collimated green light impinges the MS structure from the top and the structure focuses light to a point where the spherical bead is optically trapped.

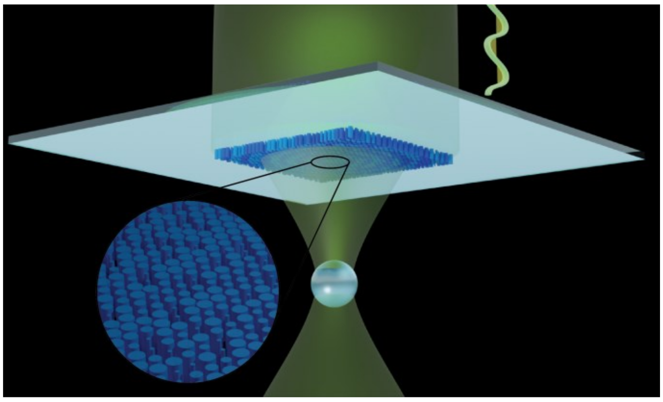

Fig. 6.7. The concept of optical trapping using an MS instead of a bulky objective.

Given the Nyquist–Shannon sampling theorem, the periodicity of 200 nm and 210 nm were chosen to meet the requirements of NA = 1.2 at λ = 488 nm and λ = 532 nm, respectively. Following the design procedure, considering 140 μm as the side length of both MSs, the focal length of 30 μm and 32 μm guarantees the designed NA = 1.2 at λ = 488 nm and λ = 532 nm, respectively. In addition, these MSs were designed to work in a water environment, meaning the refractive index of the propagation medium, n_m = 1.33, should be considered for the hologram designs. To this end, λ_m = 366.92 and λ_m = 400 nm were considered as the simulation wavelengths, respectively. Given the designed parameters, a dot-shaped image as the holographic image with the parameters reported in Table 6.4 was used to design these holograms.

Table. 6.4. **Hologram parameters designed for optical trapping applications.**

	Parameter	**Value**
488 nm	Hologram resolution	700×700
	Holographic image resolution	500×500
	Hologram pixel pitch	200 nm
	Holographic image pixel pitch	25 nm
	Source intensity	Plane-wave
	Wavelength	366.92 nm
	Closest separation z	30 µm
	Holographic image offset in x-y-z	0,0,0 mm
532 nm	Hologram resolution	666×666
	Holographic image resolution	500×500
	Hologram pixel pitch	210 nm
	Holographic image pixel pitch	50 nm
	Source intensity	Plane-wave
	Wavelength	400 nm
	Distance in z	32 µm
	Holographic image offset in x-y-z	0,0,0 mm

Figure 6.8 reports on the target image, simulated holographic images, and the phase profiles obtained by the RS numerical method for these holograms.

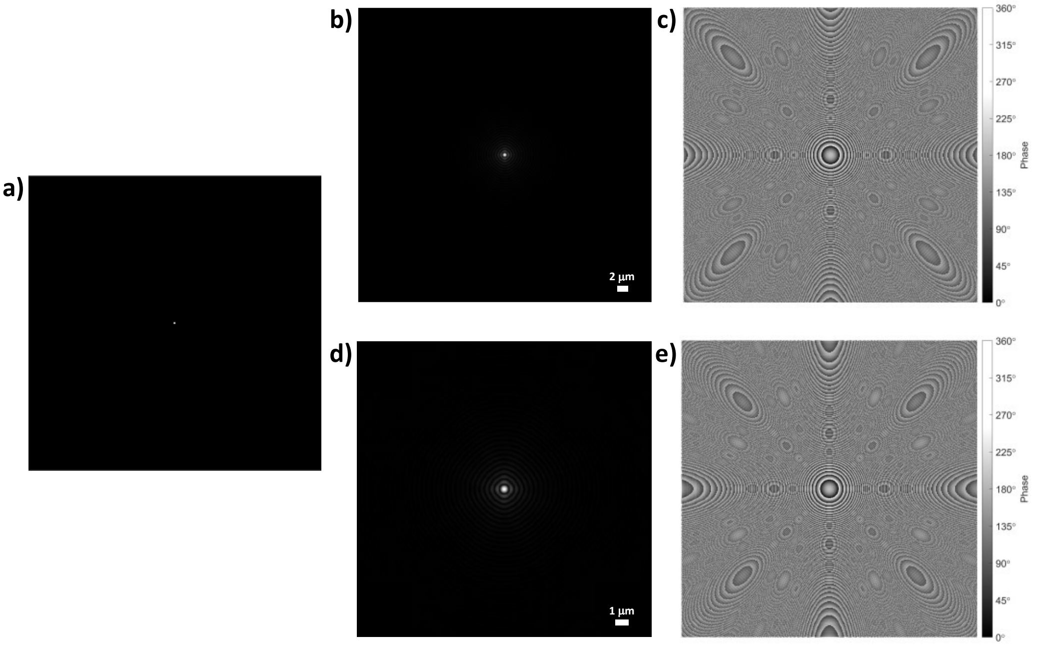

Fig. 6.8. (a) Target image to design a dot-shaped hologram. (b-c) Simulated holographic image and its hologram phase profile at λ = 488 nm. (d-e) Simulated holographic image and its hologram phase profile at λ = 532 nm.

6.3 Methods

Here, the approaches taken to do the experiments are presented. These approaches include the setups made for the experiments combined with the techniques used to make the optical trapping experiments for blue and green HMSs. The setup made to acquire holographic images is identical to the presented setup in Chapter 5.

6.3.1 Optical trapping experiments

The setup made for optical trapping experiments using two lasers with wavelengths λ = 488 nm (blue laser) and λ = 532 nm (green laser) was presented in Chapter 4. This setup provides access to the top and bottom of the objective lens for the green laser using a flip mirror. Also, the blue laser can reach the top of the objective lens. Figure 6.9(a,b) shows a simplified sketch of this setup for optical trapping using blue and green HMSs, respectively.

The HMSs were mounted on an adjustable stage on top of the objective for both experiments. Hence, the excitation of the HMSs happened through the collimated laser beams illuminating the MS samples from the top, as shown in Fig. 6. 9(a,b). To conduct the trapping experiments, the green laser light was directed to the back of the microscope and utilised for trapping SiO_2 beads. This was achieved using a 60X water immersion microscope (Nikon, PlanAPOVC60xA) objective with NA = 1.20. Then, the particle was positioned close to the focal point of HMSs before redirecting the green laser off and transferring the particle to the HMSs' optical trap.

Optical trapping by the HMSs from the top of the objective lens is completely independent of the objective itself. In optical trapping with HMSs, the objective lens was only used to record videos using a high-spec camera. The calibration of the CCD camera was co-ordinately calculated considering this objective, resulting in a pixel size of 80 nm.

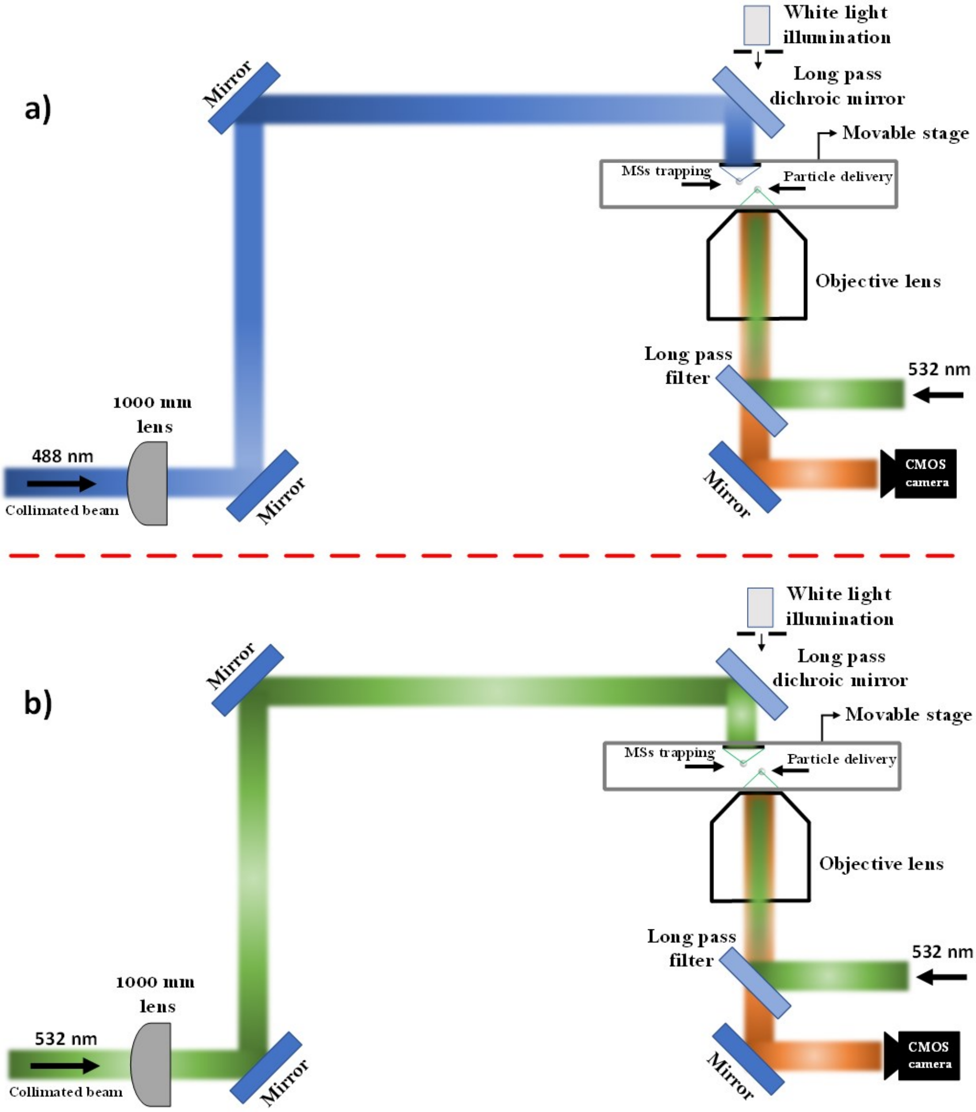

Fig. 6.9. The simplified sketch of the optical trapping experiments for (a) blue HMSs and (b) green HMSs. It is noteworthy to mention that the objective lens' position is fixed while the position of the MS mounted on the movable stage is adjustable for particle delivery.

The particle trajectories were derived from 10-second videos captured at 1000 frames per second (fps) under various laser powers. This was accomplished through a well-established method that relies on the shift properties of the Fourier transform [186].

6.4 Results

To illustrate the dependency of the performance of these MSs on the fabrication procedure, in particular the delivered EBL exposure dose, and specifically the dose factor reported in chapter three, I measured the efficiency of MSs designed at λ = 488 nm for holographic imaging but exposed at different doses during EBL exposure.

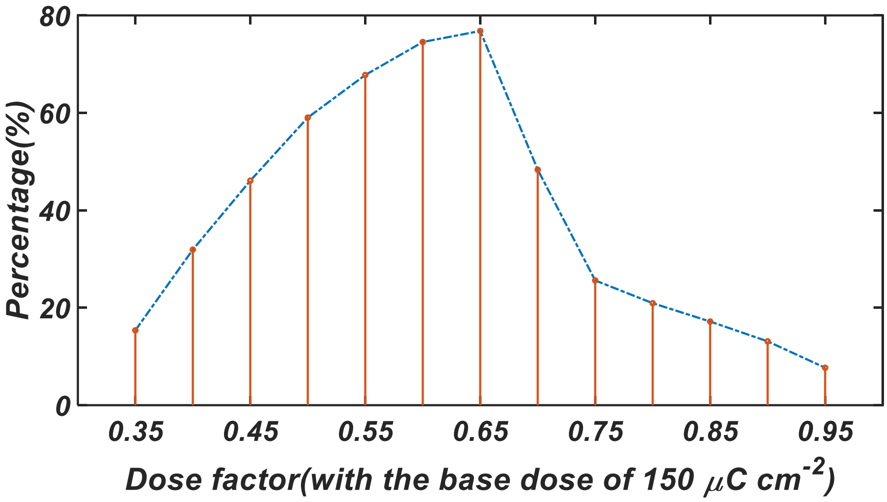

Fig. 6.10. The efficiency measurement of the ZrO_2 MS designed at 488 nm for different exposure doses.

For efficiency measurement, HMSs were configured to project a collimated beam at 30° relative to the MS normal, as detailed in Chapter 4. The diffraction efficiency of these fabricated samples reached 77% at its correct dose. However, the efficiency dropped at other doses due to underdevelopment or overdevelopment depending on the used doses. Figure 6.10 shows a sketch of diffraction efficiency as a function of the dose factor, in the range of 0.35-95, where the target dose factor was 0.65.

Figure 6.11 shows the experimental efficiency measurement of both MSs as a function of wavelength in the range of 488-700 nm. These MSs were designed for holographic imaging applications at λ = 488 nm and λ = 532 nm. Panel (a) shows the efficiency drops from 77% at 488 nm to 28% at 700 nm. Panel (b) depicts the efficiency peaks at 63% at the designed wavelength (λ = 532 nm) and is lower in other wavelengths. The phase shift of

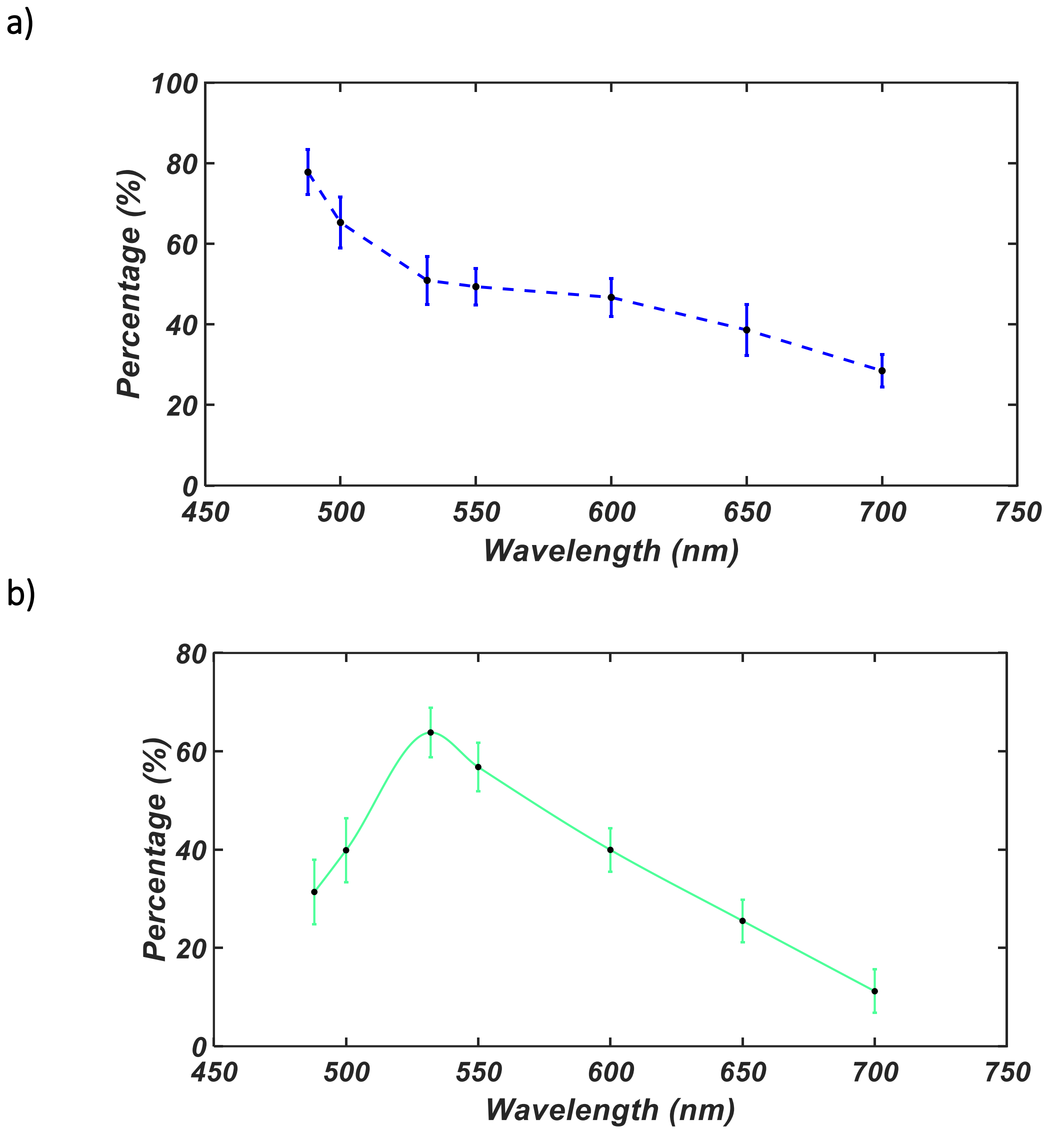

Fig. 6.11. Efficiency measurements of the ZrO_2 MSs designed for holographic imaging at (a) 488 nm and (b) 532 nm, as a function of wavelength in the visible range.

the meta-atoms in different wavelengths for both MSs can explain the reason behind the drop in efficiency in wavelengths other than the designed wavelength.

Notably, the error bars in Fig. 6.11 show the range of efficiencies measured for five separate but similar structures whose delivered EBL exposed dose are close to the nominal value.

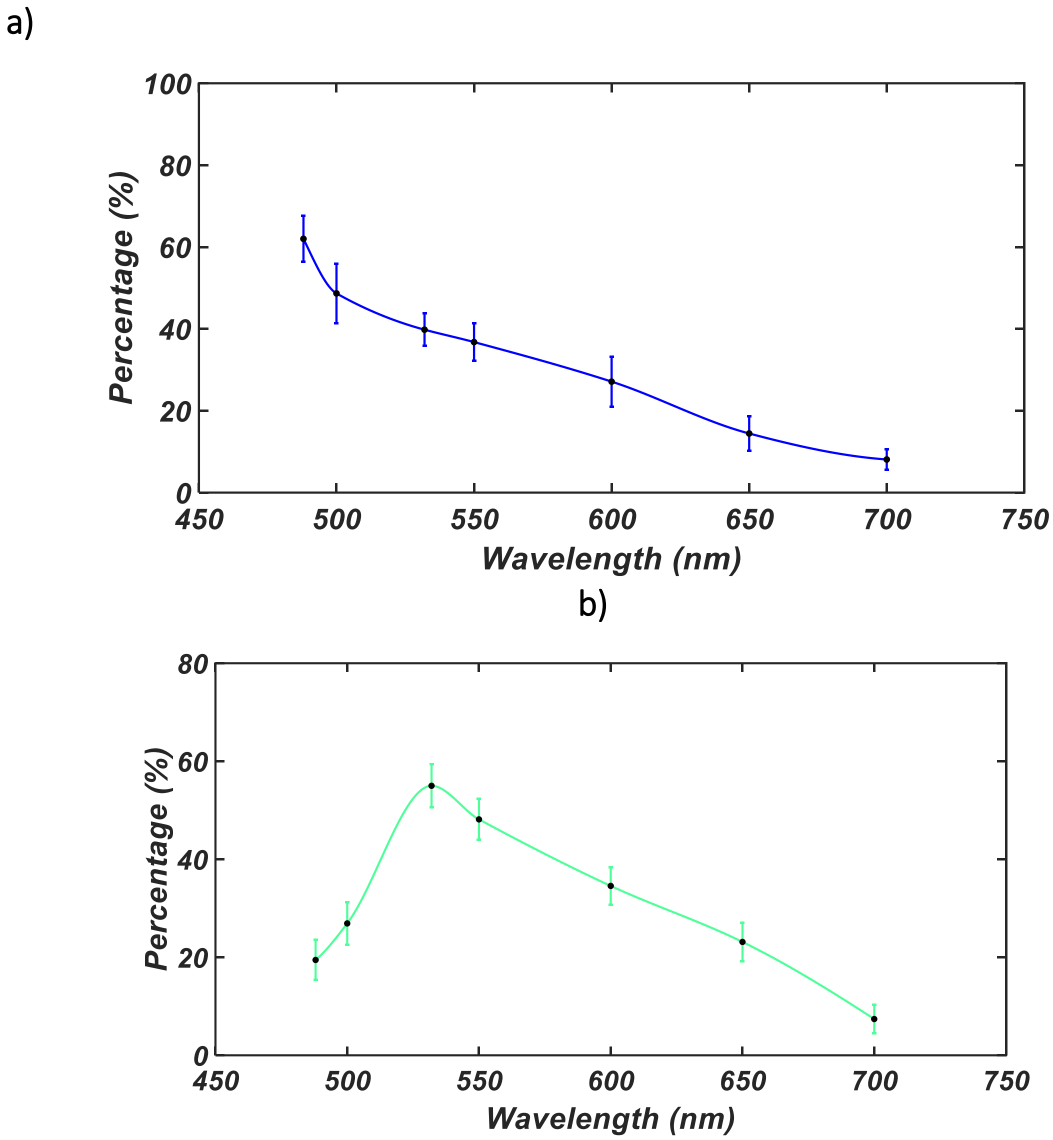

Fig. 6.12. Efficiency measurements of the ZrO_2 MSs designed for optical trapping at (a) 488 nm and (b) 532 nm, as a function of wavelength in the visible range.

Similarly, Fig. 6.12 illustrates the experimental efficiency measurements as a function of wavelength for MSs designed for optical trapping applications at $\lambda = 488$ nm and $\lambda = 532$ nm. Panel (a) displays the efficiency peaks at 62% at 488 nm and reaches 8% at 700 nm. Panel (b) illustrates the efficiency peaks at 55% at 532 nm and reaches 7% at 700 nm. These efficiencies reveal a similar behaviour but slightly lower than the MSs designed for holographic imaging. The reason behind this reduction in efficiency can be attributed to a slightly lower phase coverage of these MSs (due to having a smaller lattice constant) and fabrication quality. Similarly, the error bars show how the efficiency is dependent on the fabrication procedure.

To evaluate the performance of these HMSs in creating holographic images, a deer holographic image was designed as detailed in the design section. Figure 6.13 shows the capability of the HMS optimised for $\lambda = 532$ nm, depicting a deer-shaped holographic image at 30° off-axis with respect to the MS normal. Due to the diffraction effect, the holographic images were created bigger at larger wavelengths and their position slightly moved, as it is visible in Fig. 6.13.

Fig. 6.13. Experimental measurements of the ZrO_2 HMSs for holographic imaging applications across the visible range.

To perform optical trapping experiments, a microscope slide was used as the substrate that acts as the ceiling of a microfluidic chip. As detailed in Chapter 4, the sample was then prepared using a plastic strip and a thin coverslip to seal the sample, creating a reliable environment for the experiments. A collimated laser beam from above was used to excite the HMSs (see Fig. 6.9), creating focused spots within the microfluidic environment at distances of 30 μm and 32 μm for 488 nm and 532 nm, respectively. Imaging of the spots created by HMSs at their focal plane and recording videos of the trapped particles were conducted from below using a CCD camera (see Fig. 6.9). The blue and green HMSs were designed and fabricated with dimensions of $140\times140\ \mu m^2$, corresponding to nominal NA values of 1.22 and 1.21, respectively.

Figure 6.14 illustrates the simulated and measured beam profiles for both blue and green HMSs.

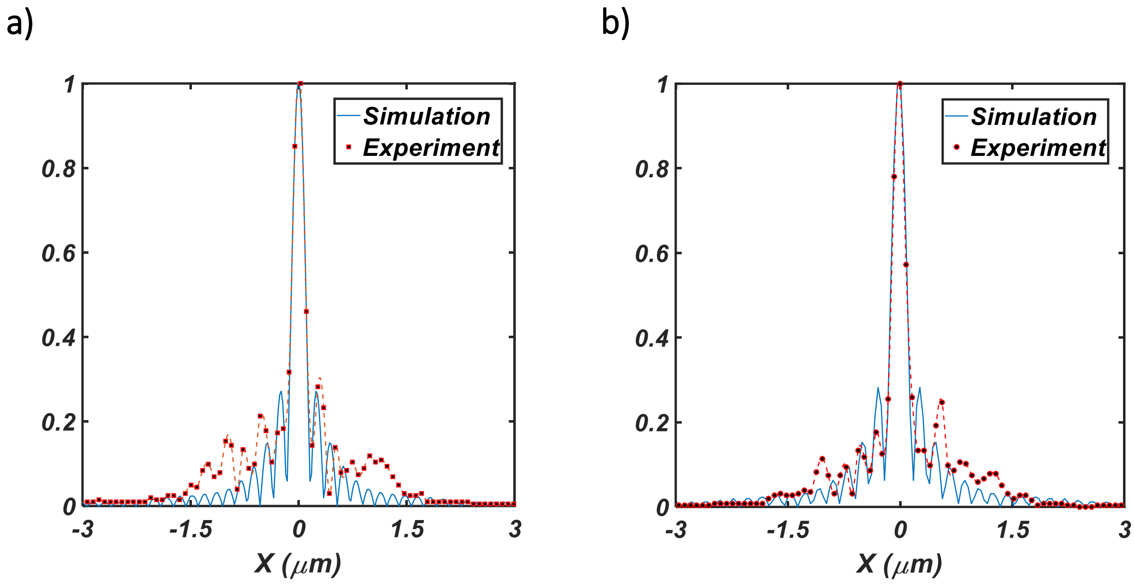

Fig. 6.14. Comparison of the simulated and experimentally measured beam profiles for blue and green HMSs.

The experimental beam profiles at the focal planes for the two HMSs are presented in Fig. 6.15(a-b). Extracting full width at half maximum (FWHM) of these profiles, both lenses exhibit NA=0.51λ/FWHM≈1.2.

In order to determine the trap stiffness of the optical trap created by the HMSs, the experimental videos of a particle that was trapped under different laser powers, were analysed. This was done using a SiO_2 particle with a diameter of 2 μm. Figure 6.15(c) illustrates the trap stiffness ($K_\perp$) which is averaged along the x (K_x) and y (K_y) directions. These indicate the values of 212 pN/μm/W and 130 pN/μm/W at 488 nm and 532 nm, respectively. It should be noted that the power values shown in Fig. 6.15(c) and the analysis are determined by measuring the power of the incident collimated light on the HMSs. Then, these values are scaled considering the geometrical overlap of these Gaussian incident beams with the HMSs and using the previously measured efficiency for

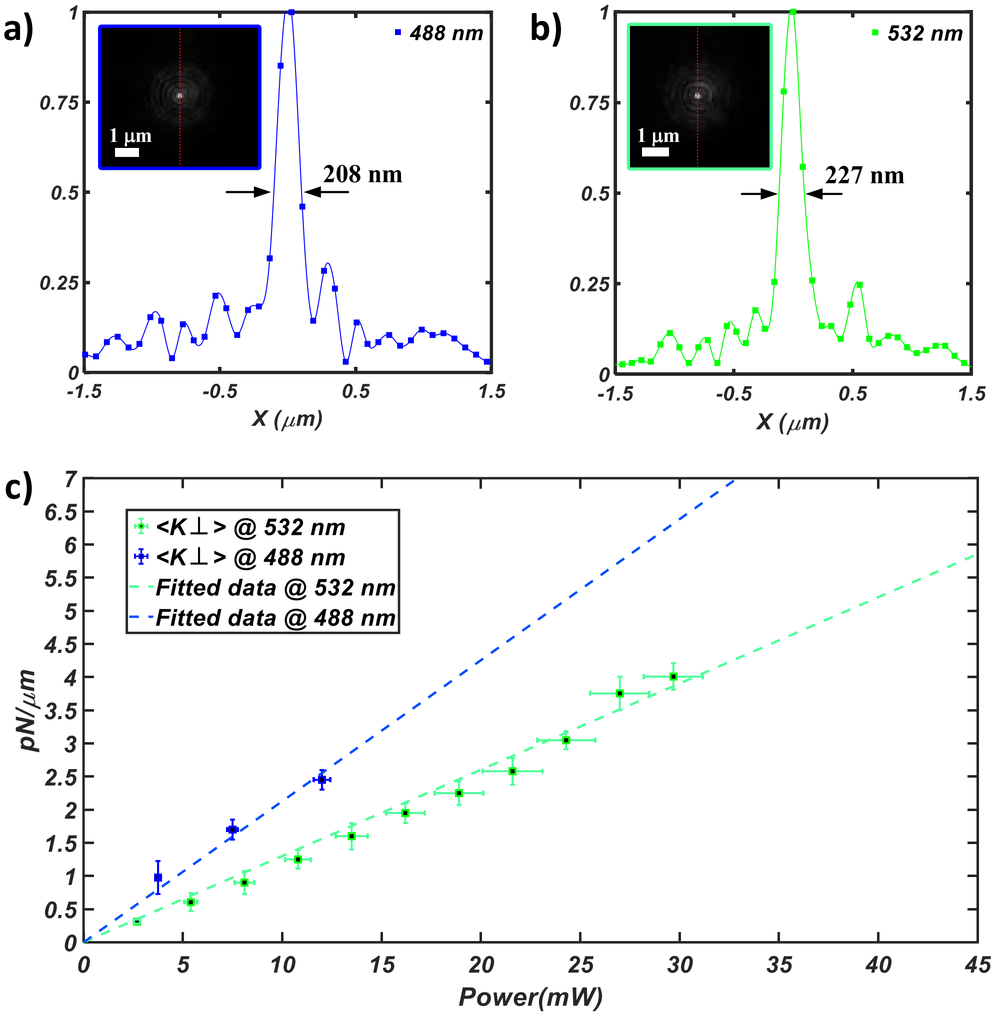

Fig. 6.15. Optical trapping measurements for blue and green HMSs. a) the experimental beam profile at 488 nm. The inserted image was taken at the HMS' focal plane, b) the experimental beam profile at 532 nm. The inserted image was taken at the HMS' focal plane, and c) the experimental trap stiffness measurements for blue and green HMSs.

both HMSs. Therefore, the absolute value for the trap stiffness should be contemplated in the context of this approximation. The error bars in Fig. 6.15 present the standard deviation of five repeated experiments.

During the experiments for both HMSs, particles remained trapped even after displacing the stage position by more than half an HMS side length. This indicates the light was coupled to the structure for these transmissive HMSs.

6.5 Discussion

To the best of my knowledge, Fig. 6.15(c) illustrates the first demonstration of on-chip optical trapping at λ = 488 nm. Explaining the intricacies of the trap stiffness in terms of the wavelength used for optical trapping and the geometry of the trapped object is a complex task, exceeding the scope of this study. Nevertheless, despite not specifically optimizing the particle geometry for this analysis, an elevated trap stiffness is observed at shorter wavelengths, aligning with general expectations [187].

These findings indicate that HMSs create a high-quality trapping spot, with the measured NA restricted by the microscope objective employed for image collection. It is noteworthy that surpassing this value is not expected, as the basic building blocks of the HMSs, the meta-atoms, do not cover the entire phase space. Furthermore, the directivity of the scattering profiles of the meta-atoms diminishes the effectiveness of HMSs at higher angles which constrains the maximum achievable NA [170]. The limited phase coverage also affects the overall diffraction efficiency of HMSs and the trap stiffness. This can be explained by considering the undiffracted light propagating into the chamber, leading to an increased scattering force on the particle. Enhancing the diffraction efficiency of HMSs is possible through further optimisation of the meta-atoms design, such as achieving a more favourable aspect ratio. However, achieving this improvement imposes more demanding fabrication requirements, in particular, an EBL system with the capability of defining high aspect ratio pillars. Also, this could be met through advanced nanolithographic approaches [188].

In this study, the meta-atoms are designed to generate a high-quality focused Gaussian beam. However, if necessary, it is possible to design HMSs with polarization-dependent meta-atoms, which can be easily achieved by optimising non-symmetrical nanofeatures. This adaptation could enable the generation of optical trapping beams with angular momentum, opening up possibilities for optical trapping and manipulation applications with increased degrees of freedom [189-190].

A notable characteristic of the suggested design is that the proposed structures create a flat and biocompatible layer at the microfluidic interface, encapsulating the meta-atoms. Consequently, the response of the meta-atoms remains unaffected by the medium in which the MS is employed, rendering it suitable for diverse biophotonics applications [191]. Furthermore, the deposition temperature for ZrO_2 is as low as 80°C, facilitating its integration with polymeric and biophotonic chips.

Ultimately, ZrO_2 exhibits distinct advantages over alternative material platforms, particularly in UV range performance [173]. These advantages can be leveraged for biological applications such as DNA analysis and medical applications [192, 193]. The combination of these features, coupled with the exceptional material hardness and device robustness, positions these proposed HMSs as ideal platforms for on-chip biophotonic integrated applications.

6.6 Conclusion

I have presented a novel material platform which performs well in the visible and UV spectrum. Introducing ZrO_2, I experimentally showed holographic imaging and optical trapping exploiting ZrO_2 HMSs operating in the visible range. I demonstrated ZrO_2 HMSs with a high numerical aperture (NA=1.2) at both 488 nm, and 532 nm, demonstrating trapping stiffness greater than 210 pN/μm/W (efficiency > 62%), and 130 pN/μm/W (efficiency > 55%), respectively. I anticipate the practical utility of these HMSs in diverse applications, including holography, optical trapping, and biomedical applications.

6.7 Contribution

I designed the holograms, meta-atoms, and ran all the simulations. I carried out all the fabrication steps for all samples related to this chapter from similar processes utilised in the Synthetic Optics research group. Also, I customised and developed the existing recipes for fabrication procedures to satisfy my needs. In particular, I worked with Nanofabrication tools, including Spin coater, EBL eLine Plus, Ebeam evaporator, RIE, Dek-talk profiler, and ALD system. I made the required setup for characterising holographic pattern generation and ran all the experiments. In addition, I customised the pre-existing optical trapping setup from scratch many times to satisfy my needs, performing the optical trapping experiments. The data analysis for the trapping data was done by another PhD student in the Synthetic Optics research group, Tomasz Plaskocinski. In general, I made approximately 90 ZrO_2 HMS samples.

Chapter 7

Incoherent holographic metasurfaces for the visible range

This chapter outlines the realisation of visible light incoherent holographic MSs employed for holographic imaging, exploiting excellent optical and mechanical properties of ZrO_2. Though visible light holographic MSs opened up advanced imaging opportunities which can be utilised for various purposes, they need a coherent light source, such as a collimated laser beam for excitation. As functioning with incoherent light may open up a wider range of applications, here, I present the design and fabrication of ZrO_2 incoherent holographic MSs to extend the applications of MSs to work with incoherent light sources such as light-emitting diodes.

7.1 Introduction

Coherent light sources emit light waves with a constant phase relationship between two points in space, and their frequency and wavelength are the same. This coherency leads to characteristics including monochromaticity, directionality, and the capability to interfere. Incoherent light sources emit light waves whose wavelengths are not in phase with each other, and they are not oscillating with the same frequency. The temporal coherency of a light source could change the speckles emitted by the source in time, whereas spatial coherency determines the correlation between the phases of light waves at different points in space. The spatial incoherency introduces characteristics including broadband spectrum, lack of directionality, and inability to interfere. Lower intensity is also one of the characteristics of incoherent light sources compared to coherent light sources, as they do not concentrate their energy into a single, powerful beam.

Coherent light sources have found applications in various fields. A collimated laser beam is the most common example of these kinds of sources. Incandescent bulbs, light-emitting diodes (LEDs), and sunlight are incoherent light sources. Thus, having an MS that works with an incoherent light source would benefit real-life applications.

To this end, there are reported works in which incoherent light sources have been placed for MS excitation, mostly for imaging applications [194-196]. For instance, a combination of specular and diffuse reflections from an MS has been used to design aluminium-based MSs to work with incoherent light for 3D full-colour image projection [195]. Also, the normal mapping technique concept is exploited to design MSs consisting of gold meta-atoms that work equally well with coherent and incoherent light sources[196]. These approaches work well for the selected meta-atoms. However, Creating an MS consisting of numerous sub-sections (tiles) and individually engineering each section is another approach.

Here, I present ZrO_2 incoherent holographic MSs at wavelength as short as $\lambda = 488$ nm for holographic imaging applications. These ZrO_2 HMSs offer a negligible absorption loss across the visible range and extend their performance to operate with incoherent light sources. The mechanical and optical properties of ZrO_2 combined with its operation with incoherent light sources open up opportunities for employing these HMSs for out-of-a-lab applications [144-146].

7.2 Design

Here, I discuss the methodology of designing incoherent illumination for HMSs. It details the concept of the unit cells as building blocks of a whole MS structure. Then, it presents the details of the implemented design.

7.2.1 Concept

This section provides a method to illuminate an MS with an incoherent light source. The coherence length of the light plays a pivotal role in the design methodology. The distance over which the light remains coherent meaning the phase relationship between different parts of the light is constant, defined as spatial coherence length, is different for coherent and incoherent light sources. Usually, this spatial coherence length of a coherent light source such as a laser beam is quite long, on the order of meters. Inversely, this spatial coherency becomes very short for incoherent light sources, such as a solid LED, usually in an order of a few microns. In other words, the coherence length of laser light is large enough to illuminate an MS structure, e.g. with a defined size of 200×200 μm^2. Typically, the size of the MSs is much larger than the spatial coherence length of an incoherent light source.

To this end, breaking down the MS structure into pixels(unit cells), where each pixel size is comparable to the spatial coherence length of the incoherent light source, can be a solution. Each pixel structure is unique and operates independently from one another. In this way, the whole MS structure, which is composed of many smaller unit cells, can work with an incoherent light source.

In Fig. 7.1, it is assumed that the target holographic image is a T-shaped object consisting of nine individual points. In panel (a) of this figure, the MS impinges with a coherent light source. Thus, the coherence length of the source is large enough to cover the entire MS size. As a result, the MS as a unit creates the T-shaped pattern. However, in panel (b), the MS interacts with an incoherent light source, where the spatial coherence length is in a range of a few microns, and subsequently, the pixel sizes named from one to nine are in this range. Notably, each pixel contributes to make a dot-shaped object as denoted in Fig. 7.1(b) and the MS as a unit makes the T-shaped holographic image.

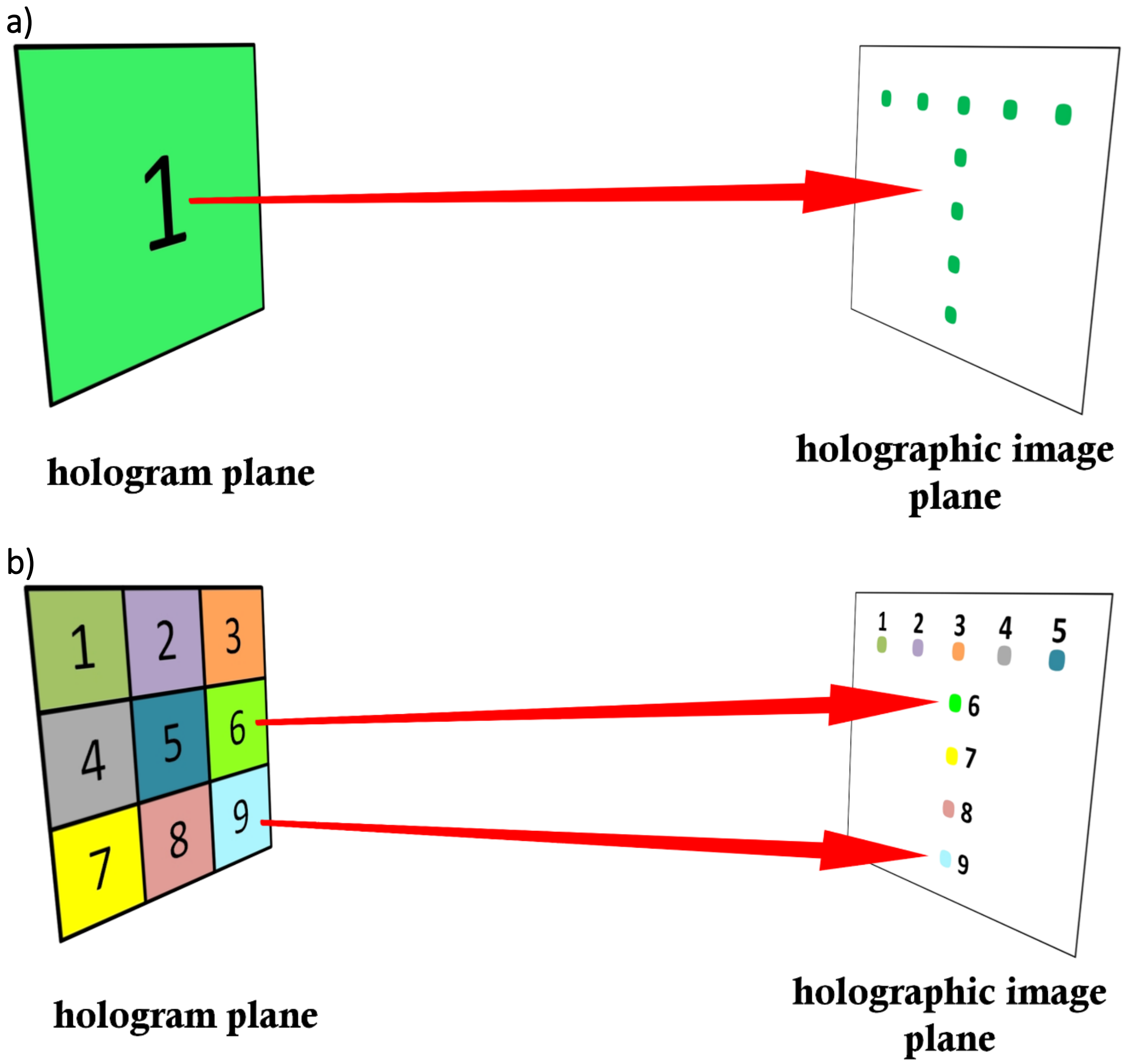

Fig. 7.1. The concept of (a) coherent light MSs, and (b) incoherent light MS design.

Clearly, the design of MSs that interact with incoherent light sources consists of numerous sub-designs for each pixel. Then, all designs can stick together and create the final structure. Considering the low intensity of an incoherent light source, it is wise to design the whole structure big enough to satisfy the required intensity for holographic imaging. The unit cell(pixel) size is an important parameter to be considered for the design depending on the spatial coherence length of the light source.

7.2.2 Unit cell design

Here, the design of the unit cells that create the whole MS geometry is discussed. These unit cells are optimised to work with an incoherent light source at the central wavelength of λ = 488 nm. It should be noted that the operational wavelength can be chosen within the visible range, as ZrO_2 meta-atoms can be designed at other visible wavelengths, which is fully addressed in Chapter 2. Each unit cell accommodates several meta-atoms, which can be determined given the periodicity of the meta-atoms and the size of the unit cell. Then, the whole size of the MS structure can be determined considering the number of unit cells.

As a proof of concept, I designed a boat-shaped hologram consisting of 25 points, as depicted in Fig. 7.2. Each point in the target image corresponds to a designed unit cell.

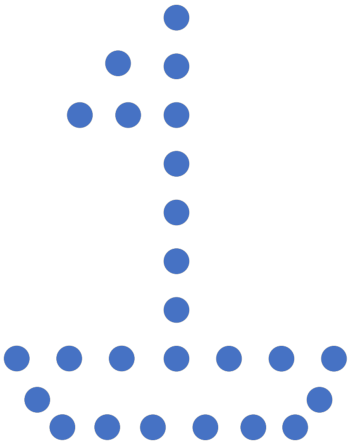

Fig. 7.2. The target image as a boat-shaped consists of 25 points.

Hence, twenty-five unit cells were designed. It is essential to mention that these unit cells can be designed using the meta-atoms presented in Chapter 2. Here, I chose to work with ZrO_2 meta-atoms with a periodicity of 400 nm. Table 7.1 reports the designed parameters for one of these unit cells.

The size of the unit cells was then calculated to be 5.2 × 5.2 μm^2. Figure 7.3 reports on the target image used to design, the simulated holographic image, and the phase profile obtained by the RS numerical method for this unit cell.

Table. 7.1. **Hologram parameters to design a boat-shaped hologram for ZrO_2 MS at 488 nm.**

Parameter	**Value**
Hologram resolution	13×13
Holographic image resolution	100×100
Hologram pixel pitch	400 nm
Holographic image pixel pitch	0.04 mm
Source intensity	Plane-wave
Wavelength	488 nm
Closest separation z	150 mm
Holographic image offset in x-y-z	30,0,0 mm

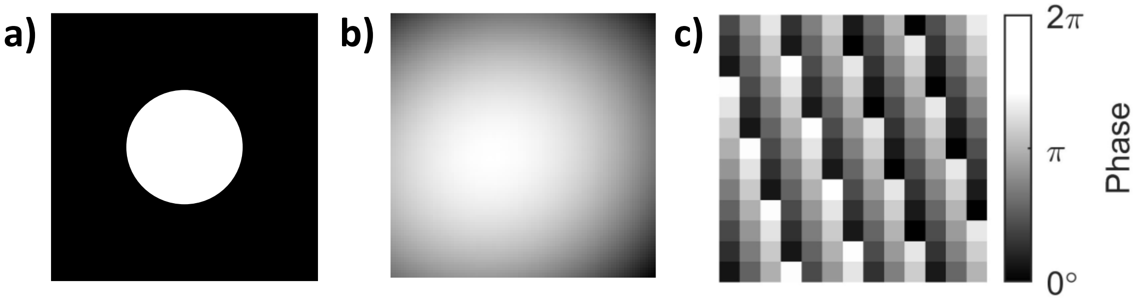

Fig. 7.3. (a) Target image to design a unit cell. (b) The simulated holographic image with a resolution of 100 × 100 pixels shows the focused light in a small designed area of 4 × 4 mm^2. (c) The phase profile consists of 13 × 13 elements determined by the design.

A customised MATLAB code written by myself was used to put the designed unit cells together combined with another MATLAB code, to create the whole MS structure to map the phase profiles to corresponding radii, using the details presented in Chapter 2.

7.3 Fabrication

The fabrication process for these ZrO_2 MSs is presented in Chapter 3. Here, I will present an image of the fabricated device. Figure 7.4 shows an image of a developed sample after the EBL procedure, consisting of twenty-five different unit cells.

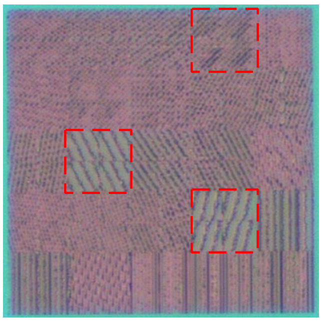

Fig. 7.4. Microscope image of a fabricated sample. The red squares highlight different unit cells.

7.4 Results

Fig. 7.5 illustrates the holographic images of the fabricated sample obtained with a coherent source. These images were obtained using the efficiency measurements setup described in Chapter 4, with a laser beam at λ = 488 nm illuminating the MS structure. Hence, it justifies the interference pattern for the boat shape in this figure. This preliminary result justifies the working principle of the aforementioned concept and design.

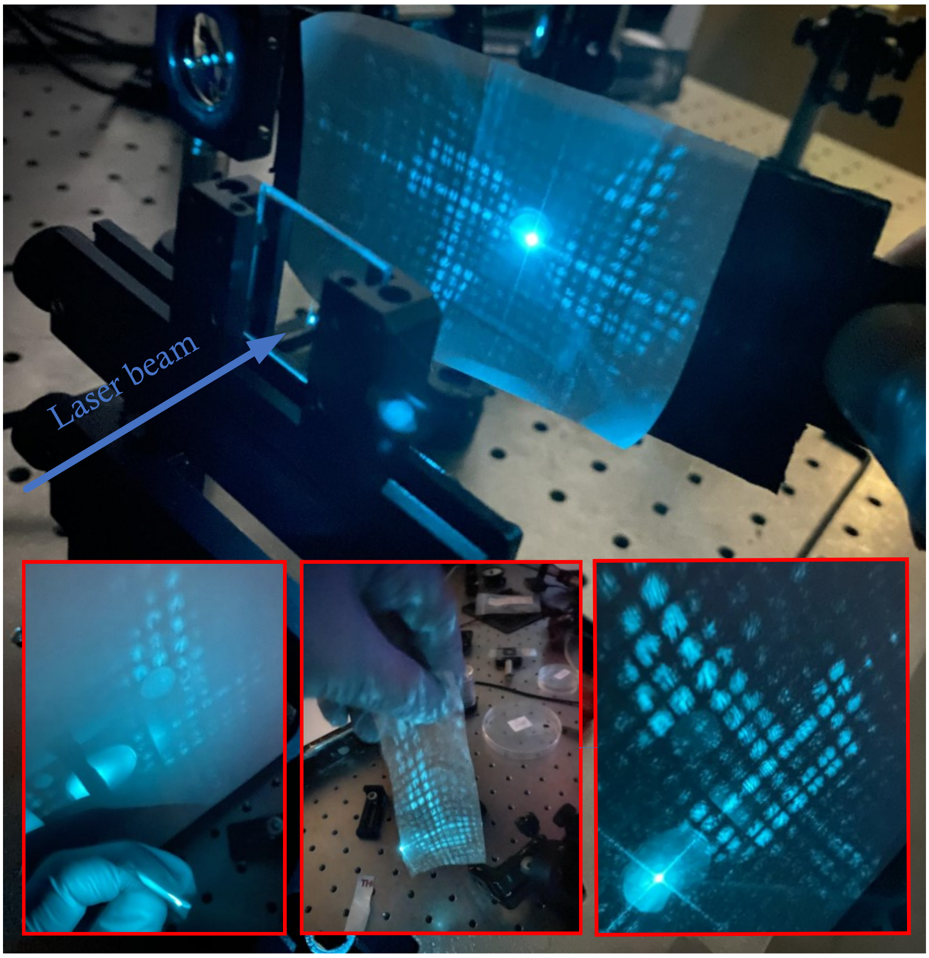

Fig. 7.5. The holographic images gained by ZrO_2 incoherent MS with a coherent laser light illumination at λ = 488 nm.

Figure 7.6 schematically illustrates a simplified experimental setup to obtain the holographic image projection with an incoherent light source. At the stage of writing this thesis, the results are yet to be obtained.

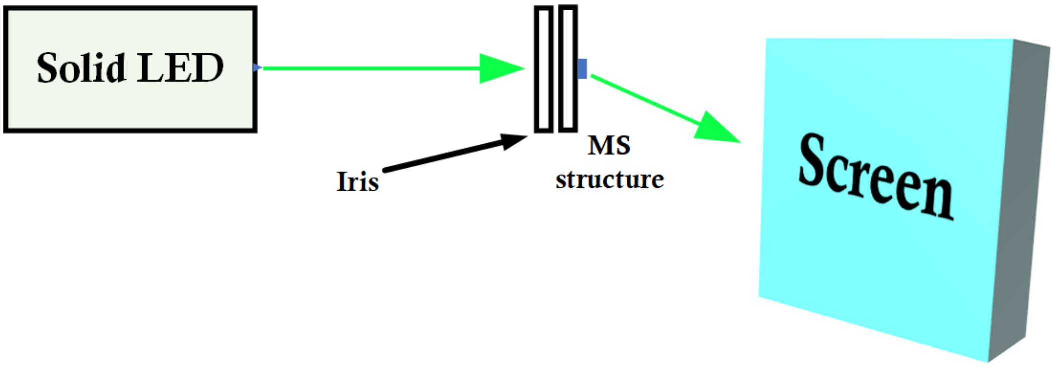

Fig. 7.6. Experimental setup to acquire the holographic image made by incoherent MSs.

7.5 Discussion

The performance of the proposed structure can be further improved by creating a mask at the back of the substrate, allowing the light to pass only through the MS aperture and block the rest of the substrate area. This decreases the intensity of the background light, which originates from the divergence of the incoherent source. This can be done by defining the aperture size in the EBL process followed by a gold evaporation.

The intensity of the holographic image can be improved by increasing the number of unit cells which send the light to a specific determined point. This will increase the size of the whole MS geometry and require a proper algorithm to design and accommodate the unit cells. Also, increasing the size of the unit cells is another approach to improve the intensity of the created holographic image. This can be explained considering the increase in the number of meta-atoms sending the light to a specific designed point. The unit cell size is related to the spatial coherence length of the source, and given the target application, this size can even be chosen to be more than 5 μm.

The broadband response of the meta-atoms across the visible range is interesting. Given the generality of the proposed design method, incoherent MSs can be made with any meta-atoms that can control the phase modulation of the scattered light. Hence, having a broadband meta-atom results in a broadband MS operation. Here, I used ZrO_2 meta-atoms optimised for the blue region, but they work at other regions of the visible range with some degradable features. This can be further improved by optimising the meta-atoms for a better optical response in other wavelengths.

Eventually, the optical characteristics of these structures, including efficiency, are yet to be measured. This can be done using another design and measurement procedure. I believe this type of MSs can facilitate the employment of MS technology for real-life applications.

7.6 Conclusion

I have presented the design of incoherent MSs across the visible range using ZrO_2 meta-atoms. Though not complete, I have validated the concept and operation of the proposed device through experimental results. I have shown the initial performance of an incoherent MS by creating boat-shaped holographic imaging. I believe the proposed approach holds promise in implementing the MSs for out-of-a-lab applications.

7.7 Contribution

I designed the meta-atoms, unit cells, and ran all the simulations. I carried out all the fabrication steps for all samples related to this chapter from similar processes utilised in the Synthetic Optics research group. Also, I customised and developed the existing recipes for fabrication procedures to satisfy my needs. In particular, I worked with Nanofabrication tools, including Spin coater, EBL eLine Plus, Dek-talk profiler, and ALD system. Though incomplete, I made the setup for obtaining holographic imaging and ran the experiments. In general, I made approximately 8 ZrO_2 incoherent MS samples.

Chapter 8

Conclusion and future works

This chapter details the summary of this thesis, describing the work done with a specific focus on the main achievements. Then, it outlines the future perspective of this research.

8.1 Thesis summary

This thesis has presented the realisation of rigid and flexible holographic MSs using unique materials with control over their performance in the target environment. It uses the GSA to design the hologram and RS equation to propagate light between the hologram and holographic image planes exploiting a numerical integral, which is fully described in Chapter 2. Following this, this chapter also delves into the modelling of these MSs using full-wave numerical simulations and presents three designed structures that can be realised using different materials. The optical response of the meta-atoms, depending on the design and the material used, is given. It should be noted that two of the designs are novel and obtained during the work of this PhD.

Chapter 3 details the fabrication of these MSs, the challenges faced, and their proper solutions. The experimental setups to run the experiments to measure the results are presented in Chapter 4, where a complex optical trapping setup working with two wavelengths is shown.

Visible light conformal holographic MSs using pure polymeric materials are discussed in Chapter 5, where I introduced a novel design which can be implemented using any material that can be processed for nanostructuring. It is essential to emphasise that due to the simplicity of the design and possible fabrication methods, the proposed structure holds promise for mass-scale production of these MSs, which can be employed in various applications.

Chapter 6 reports on holographic MSs exploiting a new material platform with properties that can open up great potential for real-life applications. The holographic image projection and efficient optical trapping across the visible range have been shown, while the proposed design introduces a unique opportunity for biophotonics experiments as the structure works independently from the operational environment.

Finally, chapter 7 presents incoherent holographic MSs, where I show how a MS can work with an incoherent light source by breaking the MS structure into smaller units, each creating part of the holographic image. The initial experimental results have been presented to validate the design and working principle.

In the following, I discuss the main novelties and achievements gained from this thesis.

8.1.1 Introduction of a novel material platform

To the best of my knowledge, this thesis has the first demonstration of bulk ZrO_2 to be utilised for MS technology. The material refractive index shows an interesting response in the visible and UV spectrum, having a weakly-dispersive behaviour while the absorption is negligible. The excellent ZrO_2 properties such as its biocompatibility make it promising for a variety of applications biophotonics, and biomedical fields. For instance, it can be used as a transparent thin-film coating to encapsulate the target structure. On the other hand, the hardness and unreactivity of ZrO_2 make this material suitable for real-life holographic applications. Hence, this thesis introduces ZrO_2 as a new material platform and demonstrates holographic imaging and optical trapping to validate this claim.

8.1.2 Introduction of a novel on-chip platform at λ < 500 nm

To the best of my knowledge, this thesis presents the first demonstration of an on-chip optical trapping in the blue region. This is provided with high NA metasurface designs at two biophotonics-friendly wavelengths of 488 nm and 532 nm. Separating TiO_2, the majority of high-index optical materials suffer from high absorption loss, especially in smaller wavelengths of the visible region. However, I have used and introduced ZrO_2 with favourable absorption loss across the visible area. In complex biophotonics experiments, the bulky objective lenses can be replaced with these MSs to offer integrated biophotonics chips. Also, the MSs can be designed to create a multi-trap optical landscape that can be interesting for some biophotonics experiments, e.g. to use an MS to trap four beads instead of a Spatial Light Modulator (SLM) for all-optical manipulation of photonics membranes.

8.2 Outlook

The primary goal of this thesis, to realise rigid and flexible visible-light MSs using advanced materials, has been achieved. It introduces novel material platforms and designs. The rest of this chapter explains the contribution of this thesis to the field followed by describing the most promising phenomena and applications for future works that can be performed based on this thesis.

8.2.1 Introduction of novel meta-atom designs for various applications

This thesis presents two new meta-atom designs that have not been previously explored. Hence, it offers new opportunities for the holographic applications of photonics MSs. In the following, I summarised the structural aspects and advantages that arise from their designs.

8.2.1.1 Pillar with top meta-atoms

The design provided in Chapter 2 is novel and reached during this PhD. The design is similar to most common cases of high-index meta-atoms where the meta-atoms are separated (not physically connected) and there is air between them. These designs usually need an etching step and removal of the photoresists at the end. However, I proposed a design in which the meta-atoms are physically connected, providing a flat layer on top of the meta-atoms. This approach eliminates the need for etching which makes the fabrication simpler. However, this simplicity comes with the cost of not a complete phase modulation offered by this design. I have experimentally shown that even not complete, the amount of phase modulation offered by this design is enough for many applications, as exemplified by demonstrating high-quality focused spots for optical trapping applications. The holographic images shown in Chapter 6 are another validation to confirm this claim.

The top cap encapsulates the meta-atoms, hence their phase response is independent of the medium they are employed. Given the biocompatibility of ZrO_2, this flat layer is interesting for biophotonics experiments. For instance, one can design a light sheet hologram and grow a cell on top of the designed MS to study the cell using light sheet microscopy.

8.2.1.2 Air-hole meta-atoms

In contrast with most meta-atom designs in which there is more than one material in their structure, this thesis offers a single material meta-atom design that can be applied to low refractive index materials such as polymers. Hence, this design enables the realisation of MSs with complete phase modulation using a single material. The realisation of all-polymeric visible light MSs presented in Chapter 5 validates the performance of the proposed design. Given the flexibility of polymers, this design can be used for different applications such as conformal holography, sensing, and augmented reality. Also, mass-scale manufacturing of these polymeric MSs can be done using state-of-the-art nanolithography techniques, detailed in the next section.

8.2.2 large-scale manufacturing of polymeric MSs for holographic image projection and augmented reality applications

In variance with most of the realised holographic MSs employed for various applications across the visible range, such as holographic imaging, sensing, augmented reality, encryption and data security, I have introduced a novel design with simplicity and demonstrated the implementation of a pure polymeric MSs across the visible range. The simplicity of this platform in terms of design and required fabrication scheme facilitates the large-scale production of these structures with methods fully described in Chapter 5. Depending on the required application, these conformable polymeric MSs can be designed for object coating, holographic image projection, augmented reality, or other useful phenomena. This can be implemented in a designed production line for mass-scale production and commercialisation.

Appendix A

A Simple Gerchberg-Saxton implementation in MATLAB

First, a simple MATLAB code representing the GSA algorithm is presented. Then, the amplitude and phase reconstructions of the target image are presented.

```
clear
close all
clc

it_no=100;    % Iteration number

% ------- defining target-----------%
target=rgb2gray(imread('smile.png'));
target=double(target);
[a, b] = size(target);
figure, imshow(target)
title('Target Image')
%----------------------------------%
%%
%------ Initializing the algorithm ------------%
ff=-pi + 2*pi*rand([a b]);     % far field with target intensity
f_to_n=zeros(a,b);             % far field with approximate target 
intensity
nf=zeros(a,b);                 % near field with source intensity
n_to_f=zeros(a,b);             % near field with approximate source 
intensity

source=ones(a,b);              % defining source intensity
k=sqrt(-1);                    % definig the imaginary numebr
ff=target.*exp(k*ff);          % initializing the far field information
%---------------------------------------------%

%------------- definig the iterative loop ------------%
for i=1:it_no

    n_to_f=ifft2(ff);
    nf=source.*exp(1j*angle(n_to_f));
    f_to_n= fft2(nf);
    ff=target.*(exp(1j*angle(f_to_n)));

end
%-----------------------------------------------------%
%%
%---------------- Plotting results -------------------%
figure, imshow(mat2gray(abs(f_to_n))),title('Amplitude reconstructed of the 
target image')
```

```
figure ,imshow(imag(f_to_n)),title('Phase reconstructed of the target
image')
c=colorbar;
c.Limits = [0 1];
c.Ticks = [0 0.5 1];
c.TickLabels = {'0','\pi','2\pi'};
c.Label.String = 'Phase';
c.FontSize=15;
%--------------------------------------------------------%
```

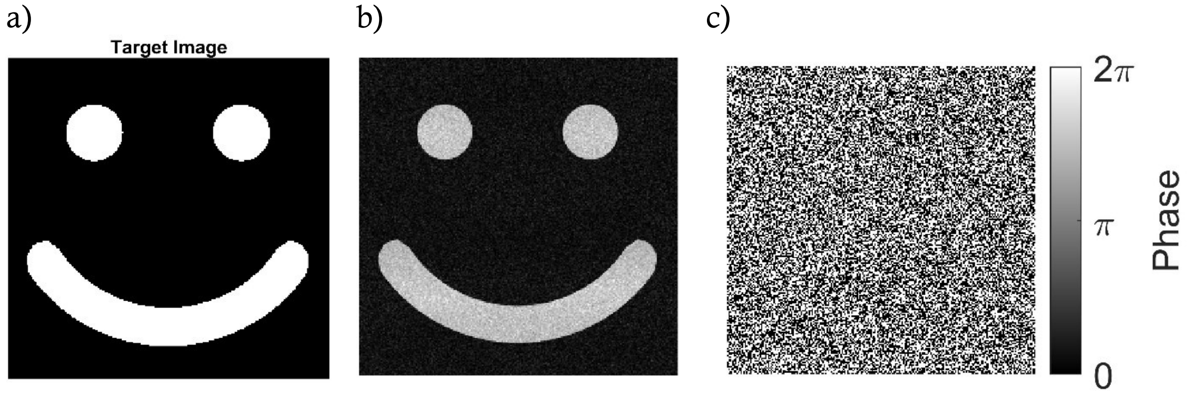

Figure. A.1. a) Target image, b) Amplitude reconstructed of the target image, c) Phase reconstructed of the target image.

Appendix B

Comparison of the refractive index of the deposited ZrO_2 with that of reported works

Figure A.2 illustrates the measured refractive index of the ALD-deposited ZrO_2 using the Ellipsometer (J.A. Woollam) and the previously reported ZrO_2 refractive index [197].

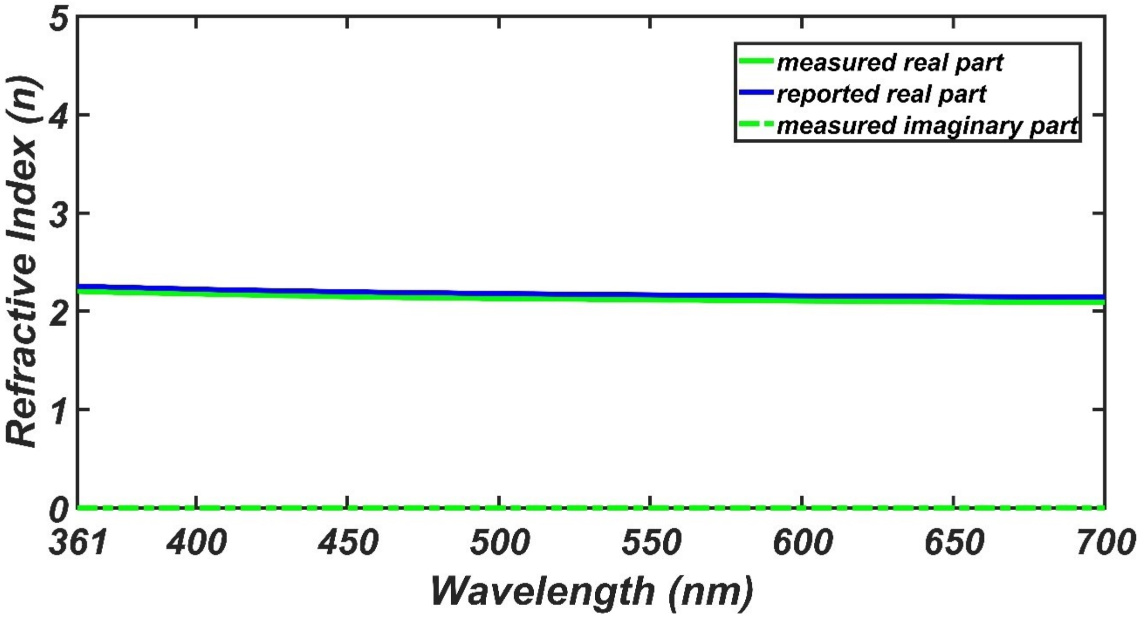

Fig. A.2. Comparison of the deposited ZrO_2 refractive index with that of the reported works. There is no imaginary part reported in ref [197].

Bibliography

[1] Burckel, D. Bruce, Michael Goldflam, Katherine M. Musick, Paul J. Resnick, Gaspar Armelles, and Michael B. Sinclair. "Coupling between plasmonic and photonic crystal modes in suspended three-dimensional meta-films." *Optics Express* 28, no. 8 (2020): 10836-10846.

[2] Burckel, David Bruce, Katherine M. Musick, Paul J. Resnick, Michael B. Sinclair, and Michael Goldflam. "Three-Dimensional Meta-films–A Discovery Platform for Structured Electromagnetic Materials." In *2020 Fourteenth International Congress on Artificial Materials for Novel Wave Phenomena (Metamaterials)*, pp. 376-378. IEEE, 2020.

[3] Hsiao, Hui-Hsin, Cheng Hung Chu, and Din Ping Tsai. "Fundamentals and applications of metasurfaces." Small Methods 1, no. 4 (2017): 1600064.

[4] Mühlenbernd, Holger, Philip Georgi, Nitipat Pholchai, Lingling Huang, Guixin Li, Shuang Zhang, and Thomas Zentgraf. "Amplitude-and phase-controlled surface plasmon polariton excitation with metasurfaces." ACS Photonics 3, no. 1 (2016): 124-129.

[5] Genet, Cyriaque, and Thomas W. Ebbesen. "Light in tiny holes." *Nature* 445, no. 7123 (2007): 39-46.

[6] Zhang, Yong, Lin Zhou, Jia-qi Li, Qian-jin Wang, and Cheng-ping Huang. "Ultra-broadband and strongly enhanced diffraction with metasurfaces." *Scientific reports* 5, no. 1 (2015): 10119.

[7] Li, Nanxi, Zhengji Xu, Yuan Dong, Ting Hu, Qize Zhong, Yuan Hsing Fu, Shiyang Zhu, and Navab Singh. "Large-area metasurface on CMOS-compatible fabrication platform: driving flat optics from lab to fab." *Nanophotonics* 9, no. 10 (2020): 3071-3087.

[8] Glybovski, Stanislav B., Sergei A. Tretyakov, Pavel A. Belov, Yuri S. Kivshar, and Constantin R. Simovski. "Metasurfaces: From microwaves to visible." Physics reports 634 (2016): 1-72.

[9] Bryant, F. "Snell's law of refraction." Physics Bulletin 9, no. 12 (1958): 317.

[10] Bloembergen, Nicolaas, and P. S. Pershan. "Light waves at the boundary of nonlinear media." Physical review 128, no. 2 (1962): 606.

[11] Xu, Ting, Changtao Wang, Chunlei Du, and Xiangang Luo. "Plasmonic beam deflector." Optics Express 16, no. 7 (2008): 4753-4759.

[12] Yu, Nanfang, Patrice Genevet, Francesco Aieta, Mikhail A. Kats, Romain Blanchard, Guillaume Aoust, Jean-Philippe Tetienne, Zeno Gaburro, and Federico Capasso. "Flat optics: controlling wavefronts with optical antenna metasurfaces." *IEEE Journal of Selected Topics in Quantum Electronics* 19, no. 3 (2013): 4700423-4700423.

[13] Yu, Nanfang, Patrice Genevet, Mikhail A. Kats, Francesco Aieta, Jean-Philippe Tetienne, Federico Capasso, and Zeno Gaburro. "Light propagation with phase discontinuities: generalized laws of reflection and refraction." science 334, no. 6054 (2011): 333-337.

[14] Skaar, Johannes. "Fresnel equations and the refractive index of active media." Physical Review E 73, no. 2 (2006): 026605.

[15] Li, Aobo, Shreya Singh, and Dan Sievenpiper. "Metasurfaces and their applications." Nanophotonics 7, no. 6 (2018): 989-1011.

[16] Ding, Fei, Anders Pors, and Sergey I. Bozhevolnyi. "Gradient metasurfaces: a review of fundamentals and applications." Reports on Progress in Physics 81, no. 2 (2017): 026401.

[17] Miyazaki, Hideki T., and Yoichi Kurokawa. "Controlled plasmon resonance in closed metal/insulator/metal nanocavities." Applied physics letters 89, no. 21 (2006): 211126.

[18] Fattal, David, Jingjing Li, Zhen Peng, Marco Fiorentino, and Raymond G. Beausoleil. "Flat dielectric grating reflectors with focusing abilities." Nature Photonics 4, no. 7 (2010): 466-470.

[19] Fan, Jonathan A., Chihhui Wu, Kui Bao, Jiming Bao, Rizia Bardhan, Naomi J. Halas, Vinothan N. Manoharan, Peter Nordlander, Gennady Shvets, and Federico Capasso. "Self-assembled plasmonic nanoparticle clusters." science 328, no. 5982 (2010): 1135-1138.

[20] Luk'yanchuk, Boris, Nikolay I. Zheludev, Stefan A. Maier, Naomi J. Halas, Peter Nordlander, Harald Giessen, and Chong Tow Chong. "The Fano resonance in plasmonic nanostructures and metamaterials." *Nature materials* 9, no. 9 (2010): 707-715.

[21] Grober, Robert D., Robert J. Schoelkopf, and Daniel E. Prober. "Optical antenna: Towards a unity efficiency near-field optical probe." *Applied Physics Letters* 70, no. 11 (1997): 1354-1356.

[22] Novotny, Lukas, and Niek Van Hulst. "Antennas for light." *Nature photonics* 5, no. 2 (2011): 83-90.

[23] Xu, Qiaobing, Jiming Bao, Robert M. Rioux, Raquel Perez-Castillejos, Federico Capasso, and George M. Whitesides. "Fabrication of large-area patterned nanostructures for optical applications by nanoskiving." *Nano letters* 7, no. 9 (2007): 2800-2805.

[24] Sukharev, Maxim, Jiha Sung, Kenneth G. Spears, and Tamar Seideman. "Optical properties of metal nanoparticles with no center of inversion symmetry: Observation of volume plasmons." *Physical Review B* 76, no. 18 (2007): 184302.

[25] Biagioni, Paolo, J. S. Huang, Lamberto Duo, Marco Finazzi, and B. Hecht. "Cross resonant optical antenna." *Physical review letters* 102, no. 25 (2009): 256801.

[26] Liu, S., Chin-Jung Chuang, C. W. See, G. Zoriniants, W. L. Barnes, and M. G. Somekh. "Double-grating-structured light microscopy using plasmonic nanoparticle arrays." *Optics letters* 34, no. 8 (2009): 1255-1257.

[27] Ginn, James, David Shelton, Peter Krenz, Brian Lail, and Glenn Boreman. "Polarized infrared emission using frequency selective surfaces." *Optics express* 18, no. 5 (2010): 4557-4563.

[28] Ganem, Joseph. "A behavioral demonstration of Fermat's principle." *The Physics Teacher* 36, no. 2 (1998): 76-78.

[29] Zhang, Junxi, Lide Zhang, and Wei Xu. "Surface plasmon polaritons: physics and applications." *Journal of Physics D: Applied Physics* 45, no. 11 (2012): 113001.

[30] Kim, G. M., M. A. F. Van Den Boogaart, and J. Brugger. "Fabrication and application of a full wafer size micro/nanostencil for multiple length-scale surface patterning." *Microelectronic engineering* 67 (2003): 609-614.

[31] Kelly, K. Lance, Eduardo Coronado, Lin Lin Zhao, and George C. Schatz. "The optical properties of metal nanoparticles: the influence of size, shape, and dielectric environment." (2003): 668-677.

[32] Sun, Shulin, Kuang-Yu Yang, Chih-Ming Wang, Ta-Ko Juan, Wei Ting Chen, Chun Yen Liao, Qiong He et al. "High-efficiency broadband anomalous reflection by gradient meta-surfaces." *Nano letters* 12, no. 12 (2012): 6223-6229.

[33] Sun, Shulin, Qiong He, Shiyi Xiao, Qin Xu, Xin Li, and Lei Zhou. "Gradient-index meta-surfaces as a bridge linking propagating waves and surface waves." *Nature materials* 11, no. 5 (2012): 426-431.

[34] Bin-Alam, M. Saad, Orad Reshef, Yaryna Mamchur, M. Zahirul Alam, Graham Carlow, Jeremy Upham, Brian T. Sullivan et al. "Ultra-high-Q resonances in plasmonic metasurfaces." *Nature communications* 12, no. 1 (2021): 974.

[35] Petoukhoff, Christopher E., and Deirdre M. O'Carroll. "Absorption-induced scattering and surface plasmon out-coupling from absorber-coated plasmonic metasurfaces." *Nature communications* 6, no. 1 (2015): 7899.

[36] Won, Rachel. "The rise of plasmonic metasurfaces." *Nature Photonics* 11, no. 8 (2017): 462-464.

[37] Liu, Bo, Kerui Song, and Jiangnan Xiao. "Two-dimensional optical metasurfaces: From plasmons to dielectrics." *Advances in Condensed Matter Physics* 2019 (2019).

[38] Yu, Nanfang, and Federico Capasso. "Flat optics with designer metasurfaces." *Nature materials* 13, no. 2 (2014): 139-150.

[39] Alu, Andrea, and Nader Engheta. "Input impedance, nanocircuit loading, and radiation tuning of optical nanoantennas." *Physical review letters* 101, no. 4 (2008): 043901.

[40] Luo, Weijie, Shulin Sun, He-Xiu Xu, Qiong He, and Lei Zhou. "Transmissive ultrathin Pancharatnam-Berry metasurfaces with nearly 100% efficiency." *Physical Review Applied* 7, no. 4 (2017): 044033.

[41] Ding, Xumin, Francesco Monticone, Kuang Zhang, Lei Zhang, Dongliang Gao, Shah Nawaz Burokur, Andre De Lustrac, Qun Wu, Cheng-Wei Qiu, and Andrea Alù. "Ultrathin Pancharatnam–Berry metasurface with maximal cross-polarization efficiency." *Advanced materials* 27, no. 7 (2015): 1195-1200.

[42] Xu, He-Xiu, Guang-Ming Wang, Tong Cai, Jun Xiao, and Ya-Qiang Zhuang. "Tunable Pancharatnam–Berry metasurface for dynamical and high-efficiency anomalous reflection." *Optics express* 24, no. 24 (2016): 27836-27848.

[43] Liu, Chuanbao, Yang Bai, Qian Zhao, Yihao Yang, Hongsheng Chen, Ji Zhou, and Lijie Qiao. "Fully controllable Pancharatnam-Berry metasurface array with high conversion efficiency and broad bandwidth." *Scientific reports* 6, no. 1 (2016): 34819.

[44] Luo, Lin, Min Ouyang, Haihua Fan, Qiaofeng Dai, Daquan Lu, Haiying Liu, and Sheng Lan. "Highly efficient spin-polarized beam splitter based on silicon Pancharatnam–Berry metasurface." *Journal of Optics* 24, no. 10 (2022): 105001.

[45] Tian, Ying, Xufeng Jing, Hao Yu, Haiyong Gan, Chenxia Li, and Zhi Hong. "Manipulation of the arbitrary scattering angle based on all-dielectric transmissive Pancharatnam Berry phase coding metasurfaces in the visible range." *Optics Express* 28, no. 21 (2020): 32107-32123.

[46] Huang, Lingling, Xianzhong Chen, Holger Mühlenbernd, Guixin Li, Benfeng Bai, Qiaofeng Tan, Guofan Jin, Thomas Zentgraf, and Shuang Zhang. "Dispersionless phase discontinuities for controlling light propagation." *Nano letters* 12, no. 11 (2012): 5750-5755.

[47] Burch, James, Dandan Wen, Xianzhong Chen, and Andrea Di Falco. "Conformable holographic metasurfaces." *Scientific Reports* 7, no. 1 (2017): 4520.

[48] Cong, Longqing, Ningning Xu, Weili Zhang, and Ranjan Singh. "Polarization control in terahertz metasurfaces with the lowest order rotational symmetry." *Advanced Optical Materials* 3, no. 9 (2015): 1176-1183.

[49] Chen, Xianzhong, Lingling Huang, Holger Mühlenbernd, Guixin Li, Benfeng Bai, Qiaofeng Tan, Guofan Jin, Cheng-Wei Qiu, Shuang Zhang, and Thomas Zentgraf. "Dual-polarity plasmonic metalens for visible light." *Nature communications* 3, no. 1 (2012): 1198.

[50] Ullah, Naqeeb, Ruizhe Zhao, and Lingling Huang. "Recent advancement in optical metasurface: fundament to application." *Micromachines* 13, no. 7 (2022): 1025.

[51] Kang, Ming, Tianhua Feng, Hui-Tian Wang, and Jensen Li. "Wave front engineering from an array of thin aperture antennas." *Optics express* 20, no. 14 (2012): 15882-15890.

[52] Wen, Dandan, Fuyong Yue, Santosh Kumar, Yong Ma, Ming Chen, Ximing Ren, Peter E. Kremer et al. "Metasurface for characterization of the polarization state of light." *Optics express* 23, no. 8 (2015): 10272-10281.

[53] Yang, Ling-Jun, Sheng Sun, and E. I. Wei. "Ultrawideband reflection-type metasurface for generating integer and fractional orbital angular momentum." *IEEE Transactions on Antennas and Propagation* 68, no. 3 (2019): 2166-2175.

[54] Wang, Shiyi, and Qiwen Zhan. "Reflection type metasurface designed for high efficiency vectorial field generation." *Scientific reports* 6, no. 1 (2016): 29626.

[55] Wen, Dandan, Fuyong Yue, Guixin Li, Guoxing Zheng, Kinlong Chan, Shumei Chen, Ming Chen et al. "Helicity multiplexed broadband metasurface holograms." *Nature communications* 6, no. 1 (2015): 8241.

[56] Zheng, Guoxing, Holger Mühlenbernd, Mitchell Kenney, Guixin Li, Thomas Zentgraf, and Shuang Zhang. "Metasurface holograms reaching 80% efficiency." *Nature nanotechnology* 10, no. 4 (2015): 308-312.

[57] Aoni, Rifat Ahmmed, Mohsen Rahmani, Lei Xu, Khosro Zangeneh Kamali, Andrei Komar, Jingshi Yan, Dragomir Neshev, and Andrey E. Miroshnichenko. "High-efficiency visible light manipulation using dielectric metasurfaces." *Scientific Reports* 9, no. 1 (2019): 6510.

[58] Devlin, Robert C., Mohammadreza Khorasaninejad, Wei-Ting Chen, Jaewon Oh, and Federico Capasso. "High efficiency dielectric metasurfaces at visible wavelengths." *arXiv preprint arXiv:1603.02735* (2016).

[59] Chen, Michael, Minseok Kim, Alex MH Wong, and George V. Eleftheriades. "Huygens' metasurfaces from microwaves to optics: a review." *Nanophotonics* 7, no. 6 (2018): 1207-1231.

[60] Wong, Joseph PS, Michael Selvanayagam, and George V. Eleftheriades. "Design of unit cells and demonstration of methods for synthesizing Huygens metasurfaces." *Photonics and Nanostructures-Fundamentals and Applications* 12, no. 4 (2014): 360-375.

[61] Ataloglou, Vasileios G., Michael Chen, Minseok Kim, and George V. Eleftheriades. "Microwave Huygens' metasurfaces: Fundamentals and applications." *IEEE Journal of Microwaves* 1, no. 1 (2021): 374-388.

[62] Wan, Xiang, Sheng Li Jia, Tie Jun Cui, and Yong Jiu Zhao. "Independent modulations of the transmission amplitudes and phases by using Huygens metasurfaces." *Scientific reports* 6, no. 1 (2016): 25639.

[63] Epstein, Ariel, and George V. Eleftheriades. "Huygens' metasurfaces via the equivalence principle: design and applications." *JOSA B* 33, no. 2 (2016): A31-A50.

[64] Baker, Bevan B., and Edward Thomas Copson. The mathematical theory of Huygens' principle. Vol. 329. American Mathematical Soc., 2003.

[65] Cheng, Jierong, Samad Jafar-Zanjani, and Hossein Mosallaei. "All-dielectric ultrathin conformal metasurfaces: lensing and cloaking applications at 532 nm wavelength." *Scientific reports* 6, no. 1 (2016): 38440.

[66] Mie, Gustav. "Beiträge zur Optik trüber Medien, speziell kolloidaler Metallösungen." *Annalen der physik* 330, no. 3 (1908): 377-445.

[67] Kruk, Sergey, Ben Hopkins, Ivan I. Kravchenko, Andrey Miroshnichenko, Dragomir N. Neshev, and Yuri S. Kivshar. "Invited Article: Broadband highly efficient dielectric metadevices for polarization control." *Apl Photonics* 1, no. 3 (2016): 030801.

[68] Decker, Manuel, Isabelle Staude, Matthias Falkner, Jason Dominguez, Dragomir N. Neshev, Igal Brener, Thomas Pertsch, and Yuri S. Kivshar. "High-efficiency dielectric Huygens' surfaces." *Advanced Optical Materials* 3, no. 6 (2015): 813-820.

[69] Zywietz, Urs, Andrey B. Evlyukhin, Carsten Reinhardt, and Boris N. Chichkov. "Laser printing of silicon nanoparticles with resonant optical electric and magnetic responses." *Nature communications* 5, no. 1 (2014): 1-7.

[70] Kuznetsov, Arseniy I., Andrey E. Miroshnichenko, Mark L. Brongersma, Yuri S. Kivshar, and Boris Luk'yanchuk. "Optically resonant dielectric nanostructures." *Science* 354, no. 6314 (2016).

[71] Jahani, Saman, and Zubin Jacob. "All-dielectric metamaterials." *Nature nanotechnology* 11, no. 1 (2016): 23-36.

[72] Fu, Yuan Hsing, Arseniy I. Kuznetsov, Andrey E. Miroshnichenko, Ye Feng Yu, and Boris Luk'yanchuk. "Directional visible light scattering by silicon nanoparticles." *Nature communications* 4, no. 1 (2013): 1-6.

[73] Aieta, Francesco, Mikhail A. Kats, Patrice Genevet, and Federico Capasso. "Multiwavelength achromatic metasurfaces by dispersive phase compensation." *Science* 347, no. 6228 (2015): 1342-1345.

[74] Lalanne, Philippe. "Waveguiding in blazed-binary diffractive elements." *JOSA A* 16, no. 10 (1999): 2517-2520.

[75] Kamali, Seyedeh Mahsa, Amir Arbabi, Ehsan Arbabi, Yu Horie, and Andrei Faraon. "Decoupling optical function and geometrical form using conformal flexible dielectric metasurfaces." *Nature communications* 7, no. 1 (2016): 1-7.

[76] Arbabi, Amir, Yu Horie, Mahmood Bagheri, and Andrei Faraon. "Dielectric metasurfaces for complete control of phase and polarization with subwavelength spatial resolution and high transmission." *Nature nanotechnology* 10, no. 11 (2015): 937-943.

[77] Arbabi, Amir, Yu Horie, Alexander J. Ball, Mahmood Bagheri, and Andrei Faraon. "Subwavelength-thick lenses with high numerical apertures and large efficiency based on high-contrast transmitarrays." *Nature communications* 6, no. 1 (2015): 1-6.

[78] Shalaev, Mikhail I., Jingbo Sun, Alexander Tsukernik, Apra Pandey, Kirill Nikolskiy, and Natalia M. Litchinitser. "High-efficiency all-dielectric metasurfaces for ultracompact beam manipulation in transmission mode." *Nano letters* 15, no. 9 (2015): 6261-6266.

[79] Zhou, Zhenpeng, Juntao Li, Rongbin Su, Beimeng Yao, Hanlin Fang, Kezheng Li, Lidan Zhou et al. "Efficient silicon metasurfaces for visible light." *Acs Photonics* 4, no. 3 (2017): 544-551.

[80] Li, Jing, Tiesheng Wu, Wenbin Xu, Yumin Liu, Chang Liu, Yu Wang, Zhongyuan Yu, Danfeng Zhu, Li Yu, and Han Ye. "Mechanisms of 2π phase control in dielectric metasurface and transmission enhancement effect." *Optics Express* 27, no. 16 (2019): 23186-23196.

[81] Yang, Liu, Dong Wu, Yumin Liu, Chang Liu, Zenghui Xu, Hui Li, Zhongyuan Yu, Li Yu, and Han Ye. "High-efficiency all-dielectric transmission metasurface for linearly polarized light in the visible region." *Photonics Research* 6, no. 6 (2018): 517-524.

[82] Kamali, Seyedeh Mahsa, Ehsan Arbabi, Amir Arbabi, Yu Horie, and Andrei Faraon. "Highly tunable elastic dielectric metasurface lenses." *Laser & Photonics Reviews* 10, no. 6 (2016): 1002-1008.

[83] Arbabi, Ehsan, Amir Arbabi, Seyedeh Mahsa Kamali, Yu Horie, MohammadSadegh Faraji-Dana, and Andrei Faraon. "MEMS-tunable dielectric metasurface lens." *Nature communications* 9, no. 1 (2018): 812.

[84] Arbabi, Amir, Ehsan Arbabi, Seyedeh Mahsa Kamali, Yu Horie, Seunghoon Han, and Andrei Faraon. "Miniature optical planar camera based on a wide-angle metasurface doublet corrected for monochromatic aberrations." *Nature communications* 7, no. 1 (2016): 13682.

[85] Kamali, Seyedeh Mahsa, Ehsan Arbabi, Amir Arbabi, and Andrei Faraon. "A review of dielectric optical metasurfaces for wavefront control." *Nanophotonics* 7, no. 6 (2018): 1041-1068.

[86] Arbabi, Amir, Ehsan Arbabi, Yu Horie, Seyedeh Mahsa Kamali, and Andrei Faraon. "Planar metasurface retroreflector." *Nature Photonics* 11, no. 7 (2017): 415-420.

[87] Aieta, Francesco, Patrice Genevet, Mikhail A. Kats, Nanfang Yu, Romain Blanchard, Zeno Gaburro, and Federico Capasso. "Aberration-free ultrathin flat lenses and axicons at telecom wavelengths based on plasmonic metasurfaces." *Nano letters* 12, no. 9 (2012): 4932-4936.

[88] Khorasaninejad, Mohammadreza, Wei Ting Chen, Robert C. Devlin, Jaewon Oh, Alexander Y. Zhu, and Federico Capasso. "Metalenses at visible wavelengths: Diffraction-limited focusing and subwavelength resolution imaging." *Science* 352, no. 6290 (2016): 1190-1194.

[89] Chen, Wei Ting, Alexander Y. Zhu, Vyshakh Sanjeev, Mohammadreza Khorasaninejad, Zhujun Shi, Eric Lee, and Federico Capasso. "A broadband achromatic metalens for focusing and imaging in the visible." *Nature nanotechnology* 13, no. 3 (2018): 220-226.

[90] Baek, Sangwon, Joohoon Kim, Yeseul Kim, Won Seok Cho, Trevon Badloe, Seong-Won Moon, Junsuk Rho, and Jong-Lam Lee. "High numerical aperture RGB achromatic metalens in the visible." *Photonics Research* 10, no. 12 (2022): B30-B39.

[91] Tseng, Ming Lun, Hui-Hsin Hsiao, Cheng Hung Chu, Mu Ku Chen, Greg Sun, Ai-Qun Liu, and Din Ping Tsai. "Metalenses: advances and applications." *Advanced Optical Materials* 6, no. 18 (2018): 1800554.

[92] Wang, Shuming, Pin Chieh Wu, Vin-Cent Su, Yi-Chieh Lai, Mu-Ku Chen, Hsin Yu Kuo, Bo Han Chen et al. "A broadband achromatic metalens in the visible." *Nature nanotechnology* 13, no. 3 (2018): 227-232.

[93] Hadibrata, Wisnu, Heming Wei, Sridhar Krishnaswamy, and Koray Aydin. "Inverse design and 3D printing of a metalens on an optical fiber tip for direct laser lithography." *Nano letters* 21, no. 6 (2021): 2422-2428.

[94] Zhang, Jianchao, Haowen Liang, Yong Long, Yongle Zhou, Qian Sun, Qinfei Wu, Xiao Fu et al. "Metalenses with Polarization-Insensitive Adaptive Nano-Antennas." *Laser & Photonics Reviews* 16, no. 9 (2022): 2200268.

[95] Wang, Yan, Miao Peng, Wei Cheng, Zheng Peng, Hao Cheng, Xiaodong Ren, Shengyin Zang et al. "Manipulation force analysis of nanoparticles with ultra-high numerical aperture metalens." *Optics Express* 30, no. 16 (2022): 28479-28491.

[96] Plidschun, Malte, Haoran Ren, Jisoo Kim, Ronny Förster, Stefan A. Maier, and Markus A. Schmidt. "Ultrahigh numerical aperture meta-fibre for flexible optical trapping." *Light: Science & Applications* 10, no. 1 (2021): 57.

[97] Hsu, T-W., Wenqi Zhu, Tobias Thiele, Mark O. Brown, Scott B. Papp, Amit Agrawal, and Cindy A. Regal. "Single-atom trapping in a metasurface-lens optical tweezer." *PRX Quantum* 3, no. 3 (2022): 030316.

[98] Arbabi, Amir, and Andrei Faraon. "Advances in optical metalenses." *Nature Photonics* 17, no. 1 (2023): 16-25.

[99] Gabor, Dennis. "A New Microscopi Prinnciple." *nature* 161 (1948): 777-778.

[100] Blanche, P-A., A. Bablumian, R. Voorakaranam, C. Christenson, W. Lin, T. Gu, D. Flores et al. "Holographic three-dimensional telepresence using large-area photorefractive polymer." *Nature* 468, no. 7320 (2010): 80-83.

[101] Lee, Byoungho. "Three'Dimensional." *Phys. Today* 66, no. 4 (2013): 36.

[102] Lee, Gun-Yeal, Gwanho Yoon, Seung-Yeol Lee, Hansik Yun, Jaebum Cho, Kyookeun Lee, Hwi Kim, Junsuk Rho, and Byoungho Lee. "Complete amplitude and phase control of light using broadband holographic metasurfaces." *Nanoscale* 10, no. 9 (2018): 4237-4245.

[103] Lee, Gun-Yeal, Gwanho Yoon, Seung-Yeol Lee, Hansik Yun, Jaebum Cho, Kyookeun Lee, Hwi Kim, Junsuk Rho, and Byoungho Lee. "Complete amplitude and phase control of light using broadband holographic metasurfaces." *Nanoscale* 10, no. 9 (2018): 4237-4245.

[104] Huang, Lingling, Shuang Zhang, and Thomas Zentgraf. "Metasurface holography: from fundamentals to applications." *Nanophotonics* 7, no. 6 (2018): 1169-1190.

[105] Burch, James, and Andrea Di Falco. "Surface topology specific metasurface holograms." *Acs Photonics* 5, no. 5 (2018): 1762-1766.

[106] Xiao, Jianling, Robert I. Hunter, Duncan A. Robertson, Graham M. Smith, Simon Horsley, Sebastian A. Schulz, and Andrea Di Falco. "Shape Dependent Conformable Holographic Metasurfaces." *Advanced Materials Technologies* 8, no. 10 (2023): 2202006.

[107] Wan, Weiwei, Jie Gao, and Xiaodong Yang. "Metasurface holograms for holographic imaging." *Advanced Optical Materials* 5, no. 21 (2017): 1700541.

[108] Hu, Yueqiang, Xuhao Luo, Yiqin Chen, Qing Liu, Xin Li, Yasi Wang, Na Liu, and Huigao Duan. "3D-Integrated metasurfaces for full-colour holography." *Light: Science & Applications* 8, no. 1 (2019): 86.

[109] Wan, Weiwei, Jie Gao, and Xiaodong Yang. "Full-color plasmonic metasurface holograms." *ACS nano* 10, no. 12 (2016): 10671-10680.

[110] Nobukawa, Teruyoshi, and Takanori Nomura. "Multilayer recording holographic data storage using a varifocal lens generated with a kinoform." *Optics letters* 40, no. 23 (2015): 5419-5422.

[111] Shimada, Ken-ichi, Tatsuro Ide, Takeshi Shimano, Ken Anderson, and Kevin Curtis. "New optical architecture for holographic data storage system compatible with Blu-ray Disc™ system." *Optical Engineering* 53, no. 2 (2014): 025102-025102.

[112] Gao, Yisheng, Yubin Fan, Yujie Wang, Wenhong Yang, Qinghai Song, and Shumin Xiao. "Nonlinear holographic all-dielectric metasurfaces." *Nano letters* 18, no. 12 (2018): 8054-8061.

[113] Genevet, Patrice, and Federico Capasso. "Holographic optical metasurfaces: a review of current progress." *Reports on Progress in Physics* 78, no. 2 (2015): 024401.

[114] Kooy, Nazrin, Khairudin Mohamed, Lee Tze Pin, and Ooi Su Guan. "A review of roll-to-roll nanoimprint lithography." *Nanoscale research letters* 9 (2014): 1-13.

[115] Zheng, Yi, Zhizhu He, Yunxia Gao, and Jing Liu. "Direct desktop printed-circuits-on-paper flexible electronics." *Scientific reports* 3, no. 1 (2013): 1786.

[116] Zhou, Jia, Tong Ge, Eileen Ng, and Joseph S. Chang. "Fully additive low-cost printed electronics with very low process variations." *IEEE Transactions on Electron Devices* 63, no. 2 (2015): 793-799.

[117] Gao, Li, Kazuki Shigeta, Abraham Vazquez-Guardado, Christopher J. Progler, Gregory R. Bogart, John A. Rogers, and Debashis Chanda. "Nanoimprinting techniques for large-area three-dimensional negative index metamaterials with operation in the visible and telecom bands." *ACS nano* 8, no. 6 (2014): 5535-5542.

[118] Ee, Ho-Seok, and Ritesh Agarwal. "Tunable metasurface and flat optical zoom lens on a stretchable substrate." *Nano letters* 16, no. 4 (2016): 2818-2823.

[119] Shaltout, Amr M., Alexander V. Kildishev, and Vladimir M. Shalaev. "Evolution of photonic metasurfaces: from static to dynamic." *JOSA B* 33, no. 3 (2016): 501-510.

[120] Schwaiger, Stephan, Andreas Rottler, and Stefan Mendach. "Rolled-up metamaterials." *Advances in OptoElectronics* 2012 (2012).

[121] Yang, Siming, Peng Liu, Mingda Yang, Qiugu Wang, Jiming Song, and Liang Dong. "From flexible and stretchable meta-atom to metamaterial: A wearable microwave meta-skin with tunable frequency selective and cloaking effects." *Scientific reports* 6, no. 1 (2016): 21921.

[122] Malek, Stephanie C., Ho-Seok Ee, and Ritesh Agarwal. "Strain multiplexed metasurface holograms on a stretchable substrate." *Nano Letters* 17, no. 6 (2017): 3641-3645.

[123] Kirkpatrick, Blair, Peter Reader-Harris, Yufang Shen, Jingzhi Wu, and Andrea Di Falco. "Advanced application of flexible metamaterials at visible frequencies." In *Photonic and Phononic Properties of Engineered Nanostructures V*, vol. 9371, pp. 54-58. SPIE, 2015.

[124] Reader-Harris, Peter, and Andrea Di Falco. "Functional metamaterials for lab-on-fiber." *Lab-on-Fiber Technology* (2015): 111-132.

[125] Omenetto, Fiorenzo G., and David L. Kaplan. "A new route for silk." *Nature Photonics* 2, no. 11 (2008): 641-643.

[126] Walia, Sumeet, Charan M. Shah, Philipp Gutruf, Hussein Nili, Dibakar Roy Chowdhury, Withawat Withayachumnankul, Madhu Bhaskaran, and Sharath Sriram. "Flexible metasurfaces and metamaterials: a review of materials and fabrication processes at micro-and nano-scales." *Applied Physics Reviews* 2, no. 1 (2015): 011303.

[127] Di Falco, Andrea, Martin Ploschner, and Thomas F. Krauss. "Flexible metamaterials at visible wavelengths." *New Journal of Physics* 12, no. 11 (2010): 113006.

[128] Wang, Yujie, Qinmiao Chen, Wenhong Yang, Ziheng Ji, Limin Jin, Xing Ma, Qinghai Song et al. "High-efficiency broadband achromatic metalens for near-IR biological imaging window." *Nature communications* 12, no. 1 (2021): 5560.

[129] Zhang, Shuyan, Chi Lok Wong, Shuwen Zeng, Renzhe Bi, Kolvyn Tai, Kishan Dholakia, and Malini Olivo. "Metasurfaces for biomedical applications: imaging and sensing from a nanophotonics perspective." *Nanophotonics* 1, no. ahead-of-print (2020).

[130] Zhang, Shuyan, Chi Lok Wong, Shuwen Zeng, Renzhe Bi, Kolvyn Tai, Kishan Dholakia, and Malini Olivo. "Metasurfaces for biomedical applications: imaging and sensing from a nanophotonics perspective." *Nanophotonics* 1, no. ahead-of-print (2020).

[131] Tittl, Andreas, Aurelian John-Herpin, Aleksandrs Leitis, Eduardo R. Arvelo, and Hatice Altug. "Metasurface-based molecular biosensing aided by artificial intelligence." Angewandte Chemie International Edition 58, no. 42 (2019): 14810-14822.

[132] Hariharan, Parameswaran. Basics of holography. Cambridge university press, 2002.

[133] Huang, Lingling, Shuang Zhang, and Thomas Zentgraf. "Metasurface holography: from fundamentals to applications." Nanophotonics 7, no. 6 (2018): 1169-1190.

[134] Bowman, David, Tiffany L. Harte, Valentin Chardonnet, Caroline De Groot, Samuel J. Denny, Guillaume Le Goc, Matthew Anderson, Philip Ireland, Donatella Cassettari, and Graham David Bruce. "High-fidelity phase and amplitude control of phase-only computer generated holograms using conjugate gradient minimisation." Optics express 25, no. 10 (2017): 11692-11700.

[135] Gerchberg, Ralph W. "A practical algorithm for the determination of plane from image and diffraction pictures." Optik 35, no. 2 (1972): 237-246.

[136] James Burch. "Flexible holographic metasurfaces." University of St Andrews, St Andrews (2019), http://hdl.handle.net/10023/18336.

[137] Constantine, A. Balanis. Antenna theory: analysis and design. Wiley-Interscience, 2005.

[138] Veerman, Jan AC, Jurgen J. Rusch, and H. Paul Urbach. "Calculation of the Rayleigh–Sommerfeld diffraction integral by exact integration of the fast oscillating factor." JOSA A 22, no. 4 (2005): 636-646.

[139] Schnars, Ulf, and Werner PO Jüptner. "Digital recording and numerical reconstruction of holograms." Measurement science and technology 13, no. 9 (2002): R85.

[140] Schars, Ulf, and Werner Jueptner. "Digital holography: digital hologram recording, numerical reconstruction, and related techniques." U. Sonars, W. Jueptner.-Berlin: Springer-Verlag (2005).

[141] Goodman, Joseph W. Introduction to Fourier optics. Roberts and Company publishers, 2005.

[142] Gupta, Saurabh, Sammy Noumbissi, and Marcel F. Kunrath. "Nano modified zirconia dental implants: Advances and the frontiers for rapid osseointegration." Medical Devices & Sensors 3, no. 3 (2020): e10076.

[143] Patil, Nikhil Avinash, and Balasubramanian Kandasubramanian. "Biological and mechanical enhancement of zirconium dioxide for medical applications." Ceramics International 46, no. 4 (2020): 4041-4057.

[144] Sagdoldina, Zhuldyz, Bauyrzhan Rakhadilov, Mazhyn Skakov, and Olga Stepanova. "Structural evolution of ceramic coatings by mechanical alloying." Materials testing 61, no. 4 (2019): 304-308.

[145] Pan, Yong. "Influence of oxygen vacancies on the electronic and optical properties of zirconium dioxide from first-principles calculations." Journal of Electronic Materials 48, no. 8 (2019): 5154-5160.

[146] Abd El-Ghany, Ossama Saleh, and Ashraf Husein Sherief. "Zirconia based ceramics, some clinical and biological aspects." Future Dental Journal 2, no. 2 (2016): 55-64.

[147] Manicone, Paolo Francesco, Pierfrancesco Rossi Iommetti, and Luca Raffaelli. "An overview of zirconia ceramics: basic properties and clinical applications." Journal of dentistry 35, no. 11 (2007): 819-826.

[148] Hisbergues, Michael, Sophie Vendeville, and Philippe Vendeville. "Zirconia: Established facts and perspectives for a biomaterial in dental implantology." Journal of Biomedical Materials Research Part B: Applied Biomaterials: An Official Journal of The Society for Biomaterials, The Japanese Society for Biomaterials, and The Australian Society for Biomaterials and the Korean Society for Biomaterials 88, no. 2 (2009): 519-529.

[149] Ahmed, Walaa M., Tom Troczynski, Anthony P. McCullagh, Chris CL Wyatt, and Ricardo M. Carvalho. "The influence of altering sintering protocols on the optical and mechanical properties of zirconia: a review." Journal of Esthetic and Restorative Dentistry 31, no. 5 (2019): 423-430.

[150] COMSOL Multiphysics® v. 6.1. www.comsol.com. COMSOL AB, Stockholm, Sweden.

[151] Arbabi, Amir, Yu Horie, Alexander J. Ball, Mahmood Bagheri, and Andrei Faraon. "Subwavelength-thick lenses with high numerical apertures and large efficiency based on high-contrast transmitarrays." *Nature communications* 6, no. 1 (2015): 7069.

[152] Khorasaninejad, Mohammadreza, Alexander Yutong Zhu, Charles Roques-Carmes, Wei Ting Chen, Jaewon Oh, Ishan Mishra, Robert C. Devlin, and Federico Capasso. "Polarization-insensitive metalenses at visible wavelengths." *Nano letters* 16, no. 11 (2016): 7229-7234.

[153] Zhang, Yihui, Zheng Yan, Kewang Nan, Dongqing Xiao, Yuhao Liu, Haiwen Luan, Haoran Fu et al. "A mechanically driven form of Kirigami as a route to 3D mesostructures in micro/nanomembranes." *Proceedings of the National Academy of Sciences* 112, no. 38 (2015): 11757-11764.

[154] Zhang, Cheng, Shawn Divitt, Qingbin Fan, Wenqi Zhu, Amit Agrawal, Yanqing Lu, Ting Xu, and Henri J. Lezec. "Low-loss metasurface optics down to the deep ultraviolet region." *Light: Science & Applications* 9, no. 1 (2020): 55.

[155] Meade, Robert D. VE, Steven G. Johnson, and Joshua N. Winn. "Photonic crystals: Molding the flow of light." (2008).

[156] Li, Kebin, Javier Alejandro Hernández-Castro, Keith Morton, and Teodor Veres. "Facile Fabrication of Flexible Polymeric Membranes with Micro and Nano Apertures over Large Areas." *Polymers* 14, no. 19 (2022): 4228.

[157] Wang, Yongjin, Wolfgang Mönch, Bernd Aatz, and Hans Zappe. "Tunable photonic crystals on a freestanding polymer membrane." *Journal of Micromechanics and Microengineering* 20, no. 1 (2009): 015003.

[158] Assaf, Salim, Mohamed Boutghatin, Yan Pennec, Vincent Thomy, Alexander Korovin, Anthony Treizebre, Michèle Carette, Abdellatif Akjouj, and Bahram Djafari-Rouhani. "Polymer photonic crystal membrane for thermo-regulating textile." *Scientific reports* 10, no. 1 (2020): 9855.

[159] Kim, Moohyuk, Nu-Ri Park, Aran Yu, Jin Tae Kim, Minseok Jeon, Seung-Woo Jeon, Sang-Wook Han, and Myung-Ki Kim. "Multilayer all-polymer metasurface stacked on optical fiber via sequential micro-punching process." *Nanophotonics* 0 (2023).

[160] Tan, You Sin, Hao Wang, Hongtao Wang, Chengfeng Pan, and Joel KW Yang. "High-throughput fabrication of large-scale metasurfaces using electron-beam lithography with SU-8 gratings for multilevel security printing." *Photonics Research* 11, no. 3 (2023): B103-B110.

[161] Winterstein, Thomas, Matthias Staab, Christian Nakic, Hans-Jürgen Feige, Jürgen Vogel, and Helmut F. Schlaak. "SU-8 electrothermal actuators: Optimization of fabrication and excitation for long-term use." *Micromachines* 5, no. 4 (2014): 1310-1322.

[162] https://refractiveindex.info/?shelf=other&book=Microchem_SU8_2000&page=specs.

[163] Biabanifard, Mohammad, Jianling Xiao, and Andrea Di Falco. "Thin-film polymeric metasurfaces for visible wavelengths." *Applied Physics Letters* 123, no. 23 (2023).

[164] Liang, Haowen, Qiaoling Lin, Xiangsheng Xie, Qian Sun, Yin Wang, Lidan Zhou, Lin Liu et al. "Ultrahigh numerical aperture metalens at visible wavelengths." *Nano letters* 18, no. 7 (2018): 4460-4466.

[165] Cadarso, Víctor J., Nachiappan Chidambaram, Loïc Jacot-Descombes, and Helmut Schift. "High-aspect-ratio nanoimprint process chains." *Microsystems & nanoengineering* 3, no. 1 (2017): 1-12.

[166] Yan, Libin, Jianling Xiao, Tomasz Plaskocinski, Mohammad Biabanifard, Saydulla Persheyev, Meisam Askari, and Andrea Di Falco. "Two-tier manipulation of holographic information." *Optics Express* 30, no. 11 (2022): 19145-19151.

[167] Kim, Inki, Won-Sik Kim, Kwan Kim, Muhammad Afnan Ansari, Muhammad Qasim Mehmood, Trevon Badloe, Yeseul Kim et al. "Holographic metasurface gas sensors for instantaneous visual alarms." *Science Advances* 7, no. 15 (2021): eabe9943.

[168] Xiong, Jianghao, En-Lin Hsiang, Ziqian He, Tao Zhan, and Shin-Tson Wu. "Augmented reality and virtual reality displays: emerging technologies and future perspectives." *Light: Science & Applications* 10, no. 1 (2021): 216.

[169] Gao, Song, Chul-Soon Park, Sang-Shin Lee, and Duk-Yong Choi. "A highly efficient bifunctional dielectric metasurface enabling polarization-tuned focusing and deflection for visible light." *Advanced Optical Materials* 7, no. 9 (2019): 1801337.

[170] Chen, Wei Ting, Alexander Y. Zhu, Mohammadreza Khorasaninejad, Zhujun Shi, Vyshakh Sanjeev, and Federico Capasso. "Immersion meta-lenses at visible wavelengths for nanoscale imaging." *Nano letters* 17, no. 5 (2017): 3188-3194.

[171] Devlin, Robert C., Mohammadreza Khorasaninejad, Wei Ting Chen, Jaewon Oh, and Federico Capasso. "Broadband high-efficiency dielectric metasurfaces for the visible spectrum." *Proceedings of the National Academy of Sciences* 113, no. 38 (2016): 10473-10478.

[172] Miyata, Masashi, Akihiro Kohno, Takeshi Komatsu, and Toshikazu Hashimoto. "Scalable direct printing of visible-light metasurfaces composed of an industrial ZrO 2-composite imprint material." *Optical Materials Express* 12, no. 10 (2022): 4169-4181.

[173] Kim, Joohoon, Wonjoong Kim, Dong Kyo Oh, Hyunjung Kang, Hongyoon Kim, Trevon Badloe, Seokwoo Kim et al. "One-step printable platform for high-efficiency metasurfaces down to the deep-ultraviolet region." *Light: Science & Applications* 12, no. 1 (2023): 68.

[174] Ashkin, Arthur. "Atomic-beam deflection by resonance-radiation pressure." *Physical Review Letters* 25, no. 19 (1970): 1321.

[175] Malagnino, Nunzia, Giuseppe Pesce, Antonio Sasso, and Ennio Arimondo. "Measurements of trapping efficiency and stiffness in optical tweezers." *Optics Communications* 214, no. 1-6 (2002): 15-24.

[176] Ashkin, Arthur. "Optical trapping and manipulation of neutral particles using lasers." *Proceedings of the National Academy of Sciences* 94, no. 10 (1997): 4853-4860.

[177] Perkins, Thomas T. "Ångström-precision optical traps and applications." *Annual review of biophysics* 43 (2014): 279-302.

[178] Ashkin, Arthur, James M. Dziedzic, and T. Yamane. "Optical trapping and manipulation of single cells using infrared laser beams." *Nature* 330, no. 6150 (1987): 769-771.

[179] Johansen, Patrick Lie, Federico Fenaroli, Lasse Evensen, Gareth Griffiths, and Gerbrand Koster. "Optical micromanipulation of nanoparticles and cells inside living zebrafish." *Nature communications* 7, no. 1 (2016): 10974.

[180] Melzer, Jeffrey E., and Euan McLeod. "Assembly of multicomponent structures from hundreds of micron-scale building blocks using optical tweezers." *Microsystems & Nanoengineering* 7, no. 1 (2021): 45.

[181] Askari, Meisam, Blair C. Kirkpatrick, Tomas Čižmár, and Andrea Di Falco. "All-optical manipulation of photonic membranes." *Optics Express* 29, no. 10 (2021): 14260-14268.

[182] Tkachenko, Georgiy, Daan Stellinga, Andrei Ruskuc, Mingzhou Chen, Kishan Dholakia, and Thomas F. Krauss. "Optical trapping with planar silicon metalenses." *Optics letters* 43, no. 14 (2018): 3224-3227.

[183] Markovich, Hen, Ivan I. Shishkin, Netta Hendler, and Pavel Ginzburg. "Optical manipulation along an optical axis with a polarization sensitive meta-lens." *Nano letters* 18, no. 8 (2018): 5024-5029.

[184] Xiao, Jianling, Tomasz Plaskocinski, Mohammad Biabanifard, Saydulla Persheyev, and Andrea Di Falco. "On-Chip Optical Trapping with High NA Metasurfaces." *ACS photonics* 10, no. 5 (2023): 1341-1348.

[185] Plidschun, Malte, Haoran Ren, Jisoo Kim, Ronny Förster, Stefan A. Maier, and Markus A. Schmidt. "Ultrahigh numerical aperture meta-fibre for flexible optical trapping." *Light: Science & Applications* 10, no. 1 (2021): 57.

[186] Leite, Ivo T., Sergey Turtaev, Xin Jiang, Martin Šiler, Alfred Cuschieri, Philip St J. Russell, and Tomáš Čižmár. "Three-dimensional holographic optical manipulation through a high-numerical-aperture soft-glass multimode fibre." *Nature Photonics* 12, no. 1 (2018): 33-39.

[187] P. H. Jones, O. M. Maragò and G. Volpe, *Optical tweezers: Principles and applications*, Cambridge University Press, Cambridge, 2015.

[188] Morton, Keith J., Gregory Nieberg, Shufeng Bai, and Stephen Y. Chou. "Wafer-scale patterning of sub-40 nm diameter and high aspect ratio (> 50: 1) silicon pillar arrays by nanoimprint and etching." *Nanotechnology* 19, no. 34 (2008): 345301.

[189] Plaskocinski, T., Y. Arita, G. D. Bruce, S. Persheyev, K. Dholakia, A. Di Falco, and H. Ohadi. "Laser writing of parabolic micromirrors with a high numerical aperture for optical trapping and rotation." *Applied Physics Letters* 123, no. 8 (2023).

[190] Cojoc, Dan, Valeria Garbin, Enrico Ferrari, Luca Businaro, Filippo Romanato, and Enzo Di Fabrizio. "Laser trapping and micro-manipulation using optical vortices." *Microelectronic Engineering* 78 (2005): 125-131.

[191] Geromel, René, Christian Weinberger, Katja Brormann, Michael Tiemann, and Thomas Zentgraf. "Porous SiO 2 coated dielectric metasurface with consistent performance independent of environmental conditions." *Optical Materials Express* 12, no. 1 (2022): 13-21.

[192] Tamariz, Jeannie, Kristina Voynarovska, Mechthild Prinz, and Theresa Caragine. "The application of ultraviolet irradiation to exogenous sources of DNA in plasticware and water for the amplification of low copy number DNA." *Journal of forensic sciences* 51, no. 4 (2006): 790-794.

[193] Gorog, Sander. *Ultraviolet-visible spectrophotometry in pharmaceutical analysis*. CRC press, 2018.

[194] Pestourie, Raphaël, Wenjie Yao, Boubacar Kanté, and Steven G. Johnson. "Efficient inverse design of large-area metasurfaces for incoherent light." *ACS Photonics* 10, no. 4 (2022): 854-860.

[195] Roth, Diane J., Mingke Jin, Alexander E. Minovich, Song Liu, Guixin Li, and Anatoly V. Zayats. "3D full-color image projection based on reflective metasurfaces under incoherent illumination." *Nano Letters* 20, no. 6 (2020): 4481-4486.

[196] Minovich, Alexander E., Manuel Peter, Felix Bleckmann, Manuel Becker, Stefan Linden, and Anatoly V. Zayats. "Reflective metasurfaces for incoherent light to bring computer graphics tricks to optical systems." *Nano Letters* 17, no. 7 (2017): 4189-4193.

[197] Wood, Darwin L., and K. Nassau. "Refractive index of cubic zirconia stabilized with yttria." *Applied Optics* 21, no. 16 (1982): 2978-2981.

List of Figures

List of Tables

Acronyms and Initialisms

3D three-dimensional. 1, 23, 24, 26, 27, 137

MS metasurface. 1, 2, 5, 6, 8, 10, 12, 13, 15, 16, 17, 18, 20, 21, 24, 26, 27, 28, 29, 30, 31, 32, 33, 34, 36, 37, 38, 42, 43, 52, 57, 58, 60, 61, 63, 66, 67, 71, 72, 77, 80, 81, 82, 84, 85, 87, 88, 89, 90, 91, 92, 93, 94, 96, 97, 101, 102, 103, 104, 105, 106, 107, 108, 109, 110, 112, 113, 114, 116, 118, 119, 120, 122, 124, 125, 126, 127, 128, 129, 133, 136, 137, 138, 139, 140, 141, 142, 143, 144, 146, 147, 148, 149, 150.

SPP surface plasmon polariton. 8, 9, 12, 13.

SEM scanning electron microscopy. 10, 11, 13, 22, 25, 26, 64, 65, 67, 72, 73, 74, 75, 76, 77, 78, 80, 102, 103, 104.

CP circularly polarised. 14, 15.

ED electric dipole, 16, 18.

MD magnetic dipole. 16, 18.

PDMS Polydimethylsiloxane. 19, 28, 29, 60, 109.

NA numerical aperture. 21, 50, 91, 94, 113, 114, 115, 116, 118, 119, 120, 122, 124, 129, 130, 132.

TiO_2 titanium dioxide. 21, 22, 64, 113, 115, 147.

LCP left-handed circularly polarised. 26, 27.

RCP right-handed circularly polarised. 26, 27.

2D two-dimensional. 27, 32, 70, 92, 94.

OPD optical path difference, 30.

ZrO_2 zirconium dioxide. 36, 42, 43, 44, 45, 46, 47, 48, 49, 50, 61, 64, 68, 71, 72, 76, 77, 78, 79, 80, 84, 85, 87, 90, 110, 112, 113, 114, 115, 116, 118, 126, 127, 128, 129, 133, 134, 136, 137, 140, 141, 142, 143, 144, 147, 148, 149, 154.

128, 130, 131, 134, 135, 136, 137, 138, 139, 142, 143, 144, 145.

GSA Gerchberg-Saxton algorithm. 36, 37, 40, 41, 42, 61, 146, 152.

FFT	Fast Fourier Transform. 37, 39, 41, 42.
RS	Rayleigh-Sommerfeld. 37, 40, 41, 42, 101, 102, 117, 118, 121, 123, 140, 146.
ALD	atomic layer deposition. 43, 67, 68,71, 72, 76, 77, 79, 134, 144, 154.
UV	ultraviolet. 43, 65, 66, 82, 113, 115, 133, 147.
ITO	Indium Tin Oxide. 44, 45, 47, 71, 78.
PMMA	polymethyl methacrylate. 42, 47, 49, 52, 57, 58, 61, 64, 65, 70, 71, 72, 73, 74, 76, 77, 78, 79, 80, 81, 82, 83, 103, 107, 108, 109.
EBL	electron beam lithography, 64, 65, 66, 71, 72, 73, 74, 75, 76, 77, 79, 81, 82, 85, 103, 110, 126, 132, 134, 141, 143, 144.
Ebeam	electron beam. 65, 68, 85, 110, 134.
RIE	Reactive Ion Etching. 65, 70, 81, 83, 85, 102, 110, 134.
DC	direct current. 70, 83.
RF	radio frequency. 70.
DI	deionised. 76, 79, 83.
IPA	isopropyl alcohol. 76, 78, 79, 83.
ETH	extra high tension. 79, 82.
FHMS	flexible holographic metasurfaces. 97, 102, 104, 105, 106, 107.
HMS	97, 113, 114, 115, 116, 121, 124, 125, 126, 129, 130, 131, 132, 133, 134, 137.
SNR	107, 108.
CNR	107, 108.
NIR	near-infrared. 112, 114.
HfO_2	hafnium dioxide. 64, 113.
OT	optical trapping. 113, 114.
LED	light-emitting diodes. 137, 138.
SLM	spatial light modulator. 148.